WATCHING THE HEALING BRAIN:

MULTIMODAL AND NON-INVASIVE IMAGING OF REGENERATIVE PROCESSES AFTER EXPERIMENTAL CEREBRAL ISCHEMIA

Inaugural-Dissertation

zur

Erlangung des Doktorgrades

der Mathematisch-Naturwissenschaftlichen Fakultät

vorgelegt von

Joanna Magdalena Adamczak

aus Skwierzyna

Universität zu Köln

Max Planck Institut
für neurologische Forschung

2013

Berichterstatter: PD. Dr. Heike Endepols

Prof. Dr. Wolfgang Walkowiak

Prof. Dr. Mathias Hoehn

Tag der mündlichen Püfung: 11.4.2013

Table of content

Abstract

Stroke is a severe disease of the brain, which leads to cell death and loss of function. Neuroprotective therapy to prevent neuronal loss has not been effective in human stroke patients. Therefore, new therapeutic strategies are needed. Spontaneous recovery can be observed in some patients. However, the basis of this phenomenon is not completely understood yet. Several endogenous regenerative processes have been observed following cerebral ischemia, which may be the reason for functional recovery and can be used as a basis for new therapeutic strategies. Shortly after the insult, endothelial cells start to proliferate and eventually lead to revascularization of ischemic brain tissue (angiogenesis). Furthermore, resident neural progenitor cells increase their proliferative activity, migrate towards the ischemic tissue and even differentiate into new neurons (neurogenesis). Detailed knowledge about the molecular mechanisms and interactions between angiogenesis and neurogenesis in response to stroke is needed in order to reveal new therapeutic targets. This PhD thesis established novel non-invasive imaging strategies to followed post-stroke angiogenesis and neurogenesis with particular regard to their dynamic temporal profiles. Bioluminescence imaging and magnetic resonance imaging were chosen for this purpose. The vascular endothelial growth factor receptor 2 was used as a molecular marker for angiogenesis, and for the first time the molecular basis of post-stroke vascular remodelling was observed non-invasively with bioluminescence imaging in an angiogenesis-specific reporter mouse. Structural changes of the vascular system were monitored with a magnetic resonance imaging strategy. Initial pronounced decrease of vessel density in ischemic tissue was followed by vessel density normalization. Non-invasive observation of endogenous neurogenesis is limited by the small number of neural progenitor cells within the adult brain. This work established the first bioluminescence protocol optimized for highly sensitive bioluminescence imaging of neurogenesis in a neurogenesis-specific reporter mouse. For the first time, increased proliferation of neural progenitor cells after stroke was observed with bioluminescence imaging. As post-stroke angiogenesis and neurogenesis may lead to regeneration of brain function, this PhD thesis established the first functional magnetic resonance imaging protocol for the specific application in mice. First investigations of brain function after stroke were performed and future studies will have the opportunity to follow functional recovery in transgenic mouse models. All methods used in this thesis bear the exceptional potential to be combined into a multimodal approach. Screening for new therapeutic targets within the brain endogenous regenerative capacity will be possible non-invasively. Furthermore, the effect of new therapies on angiogenesis, neurogenesis or functional recovery can be quickly tested.

Zusammenfassung

Der Schlaganfall ist eine schwere Erkrankung des Gehirns, welche zu Zelltod und Funktionsverlust führt. Da neuroprotektive Therapien bei Schlaganfallpatienten bisher unwirksam waren, werden neue therapeutische Ansätze benötigt. Einige Patienten zeigen nach dem Schlaganfall eine spontane Erholung, deren Grundlage noch nicht vollkommen entschlüsselt ist. Endogene, d.h. körpereigene Prozesse, können die Ursache der spontanen Erholung sein und können des weiteren als Grundlage für neue Therapien genutzt werden. Neue Blutgefäße entstehen in der Nähe das ischämische Hirngewebes (Angiogenese) und endogene neurale Vorläuferzellen wandern in das ischämische Gewebe, wo sie sich zu neuen Neuronen weiterentwickeln (Neurogenese). Detaillierte Kenntnisse über die endogenen Prozesse der Angiogenese und Neurogenese nach Schlaganfall werden nun benötigt, um auf ihrer Grundlage neue Therapien zu entwickeln. In dieser Arbeit werden erstmals nicht-invasive bildgebende Strategien verwendet um die endogenen Prozesse der Angiogenese und Neurogenese nach Schlaganfall zu beobachten und insbesondere ihren dynamischen Zeitverlauf zu dokumentieren. Für die Angiognese wurde der vaskuläre endotheliale Wachstumsfaktor Rezeptor 2 als molekularen Marker verwendet und erstmals mittels Biolumineszenzbildgebung die molekulare Regulation der Gefäßsystemveränderungen nach Schlaganfall nicht-invasive beobachtet. Strukturelle Veränderungen des Gefäßsystems wurden mittels einer kernspintomographischen Methode mit hoher räumlicher Auflösung observiert. Auf eine anfängliche Verringerung der Gefäßdichte in ischämischen Bereichen folgte einer Normalisierung. Die nicht-invasive Beobachtung der endogenen Neurogenese wird durch die geringe Anzahl von neuronalen Vorläuferzellen im adulten Gehirn erschwert. Diese Arbeit erstellte ein Protokoll für hochempfindliche Biolumineszenzbildgebung der Neurogenese in einer Neurogenese-spezifischen Reportermaus. Damit ließ sich erstmals die endogene Neurogenese nach Schlaganfall nicht-invasiv untersuchen. Da die untersuchten spontanen regenerativen Prozesse die Grundlage funktioneller Erholung sein können, wurde in dieser Arbeit erstmals ein nicht-invasives funktionelles Bildgebungsverfahren für die spezifische Anwendung an Mäusen etabliert. Erste Untersuchungen der Hirnaktivität nach Schlaganfall wurden in dieser Arbeit durchgeführt und künftige Studien haben die Möglichkeit transgene Mäuse für Untersuchungen der funktionelle Erholung nach Schlaganfall zu verwenden. Die in dieser Arbeit etablierten Verfahren stellen neue, nicht-invasiven Methoden zur Untersuchung von endogenen regenerativen Prozessen nach Schlaganfall dar. Insbesondere können sie nun zu innovativen multimodalen Ansätzen kombiniert werden. Neue Erkenntnisse über die Wechselwirkung von Angiogenese und Neurogenese können erzielt werden und Therapien schneller und einfacher auf ihre Wirksamkeit getestet werden.

Introduction

1. Stroke

Stroke remains the third-leading cause of death and the main cause of disability worldwide, leaving the majority of survivors dependent on institutional care (Donnan et al., 2008). Stroke describes the pathological situation when sudden oxygen and glucose deprivation results in severe brain damage. Depending on the cause, stroke can be either hemorrhagic or ischemic. Hemorrhagic stroke results from intra-cerebral bleeding caused by the rupture of a blood vessel in the brain parenchyma or in the subarachnoid space, which causes damage to the brain due to the elevation of intra-cranial pressure but also due to the lack of oxygen and glucose supply. Ischemic stroke can be further subdivided into thrombotic and embolic. Thrombotic stroke is the blockage of a cerebral artery by a gradual formation of a clot within this artery, while embolic stroke results from a traveling blood clot (embolus) formed somewhere else in the body. With 85-90% of all incidences, ischemic stroke represents the most common kind of stroke. Stroke symptoms are versatile, including sensory and motor dysfunction, paralysis, aphasia, nausea, and headache (Fatahzadeh and Glick, 2006) and are dependent on the size and area of the brain affected. Although stroke represents a severe and frequent disease, only few therapeutic interventions with limited applicability exist. Therefore, stroke continues to cause personal and familial tragedies. Furthermore, stroke and stroke-related rehabilitation places a heavy economical burden upon society (Meairs et al., 2006).

1.1. Pathophysiology

The blockage of a cerebral artery leads to oxygen and glucose deprivation within the area supplied by the artery. Very quickly the production of adenosine-tri-phosphate (ATP) by oxidative phosphorylation ceases and the high energy demand of the brain cannot be fulfilled (energy failure) (Dirnagl et al., 1999). This energy deficit is most severe in areas with the lowest residual blood flow (ischemic core), resulting in rapid anoxic depolarizations (Mitsios et al., 2006). Energy dependent ion pumps fail to restore ionic gradients, leading to increased intracellular ion concentration with water passively following the concentration gradient (cytotoxic edema) (Dirnagl et al., 1999). In the ischemic core, cells die quickly by necrosis. Areas with collateral blood supply experience less severe ischemia (ischemic penumbra) but incomplete restoration of ion gradients generates waves of depolarizations (peri-infarct depolarizations) leading to excessive neurotransmitter release (Dirnagl et al., 1999). Due to

impaired glial re-uptake of neurotransmitters, extracellular concentrations of glutamate become toxic through excessive activation of glutamate receptors (excitotoxicity) causing an accumulation of intracellular calcium (Iadecola and Anrather, 2011b). Excessive intracellular calcium triggers several deleterious events including activation of lytic enzymes, mitochondrial dysfunction and oxidative stress (Moskowitz et al., 2010). As a result, free radicals are produced in detrimental amounts, which are potent destroyers of cell membranes, DNA and any other cellular component. Damaged endothelium causes a break-down of the protective blood-brain barrier, which leads to an increased permeability to plasma proteins and consequently to increased fluid content within the extracellular space (vasogenic edema) (Durukan and Tatlisumak, 2007). Starting already a few hours after stroke, upregulation of pro-inflammatory cytokines calls peripheral immune cells to infiltrate the injured brain parenchyma, which form together with activated astrocytes and brain resident microglia a glial scar (Iadecola and Anrather, 2011a). The above described events after ischemia activate programmed cell death (apoptosis) which expands tissue damage in the ischemic penumbra (Mitsios et al., 2006, Ginsberg, 2003, Durukan and Tatlisumak, 2007). The temporal aspect of the events within the ischemic cascade is illustrated in Figure 1. Details of the underlying separate events are reviewed in (Chavez et al., 2009, Dirnagl et al., 1999, Durukan and Tatlisumak, 2007, Iadecola and Anrather, 2011b, Mitsios et al., 2006, Moskowitz et al., 2010)

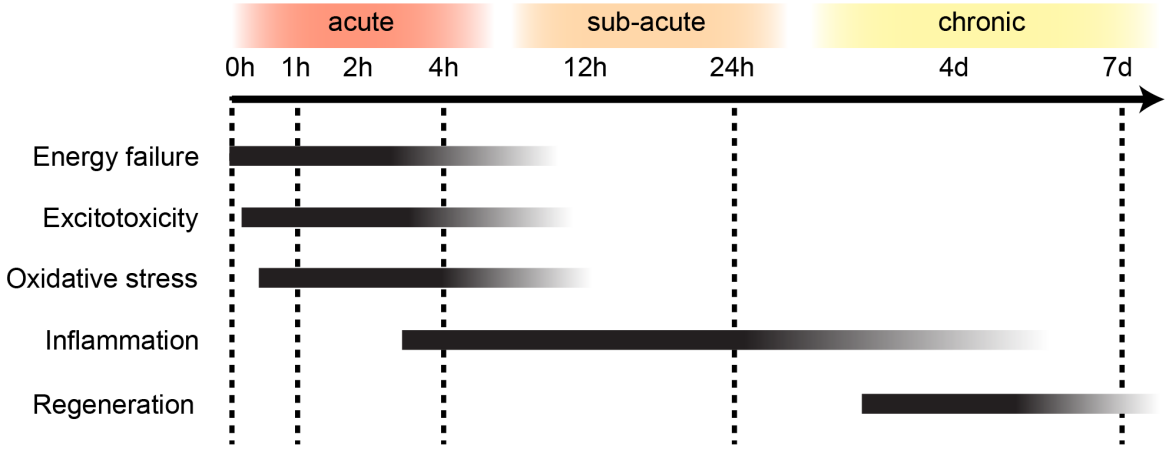

Figure 1: Time line of major events of the ischemic cascade
Detrimental effects of energy failure, excitotoxicity and oxidative stress predominantly occur during the acute phase. The inflammatory reaction starts during the first few hours after onset of ischemia, while regenerative processes are effective during the chronic phase.

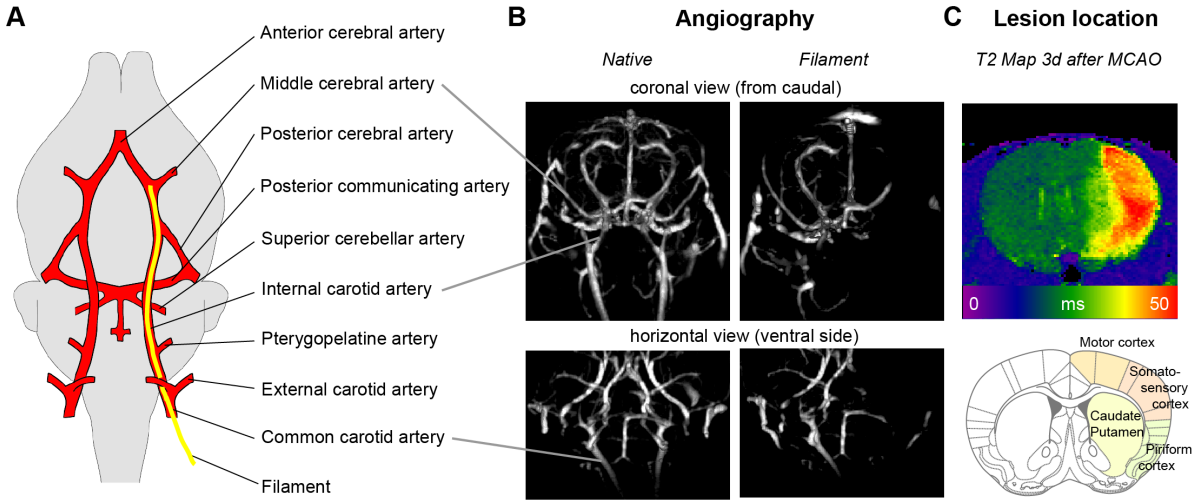

Figure 2: Middle cerebral artery occlusion in rodents
A Architecture of major cerebral arteries. A filament is inserted through the common carotid artery and blocks the blood flow to the middle cerebral artery. **B** Magnetic resonance angiography shows blood flow through the major cerebral arteries before (left panel) and after (right panel) insertion of the filament. **C** Top: MR T2 map at 3 days after MCAO in a mouse (30 min occlusion time). Bottom: Corresponding brain section taken from the mouse brain atlas (Paxinos and Franklin, 2001). Cerebral lesions after MCAO form in the caudate putamen, thalamus, and the cortex, including the somatosensory and piriform cortex.

1.2. Rodent model of transient focal cerebral ischemia

In order to study molecular mechanisms or to investigate the benefit of therapeutic interventions, ischemic stroke is modeled in experimental animals. The majority of experiments are carried out on small animals such as rats and mice, which have a similar cerebrovascular system as humans. Several animal models have been developed to study ischemic stroke. The most frequently used model in experimental stroke research uses the *intraluminal filament technique*, which was first developed in the rat model by Koizumi et al. (1986) (Koizumi et al., 1986). A filament is introduced into the lumen of an extra-cranial artery and advanced through the internal carotid artery until it blocks the blood flow to the middle cerebral artery (Figure 2A+B). Therefore, this technique is commonly referred to as middle cerebral artery occlusion (MCAO). With this model the duration of ischemia can be controlled. Leaving the filament in the artery results in a permanent occlusion model. Retraction of the filament models successful reperfusion (transient ischemia). Infarcts develop in the vascular territory of the middle cerebral artery (MCA), including the lateral striatum, the thalamus and the fronto-parietal cortex (Figure 2C). A very good reproducibility of infarct size was achieved by coating the filament with poly-L-lysine, which increases adhesion to the vascular wall (Belayev et al., 1999). Early studies used predominantly rats for intraluminal MCAO (Belayev et al., 1996, Koizumi et al., 1986, Longa et al., 1989). With the availability of a broad spectrum of transgenic mice, this technique was adjusted for this

species (Belayev et al., 1999, Hata et al., 2000), allowing investigation of molecular mechanisms of stroke. The advantage of this method is the relative low invasiveness with no need for craniectomy and the high reproducibility with control over the ischemic duration.

Intraluminal MCAO was used to model transient cerebral ischemia in this thesis. While rat MCAO was already established in our laboratory, modifications of the surgical procedure for mouse MCAO were evaluated during the course of this thesis and an optimal mouse MCAO protocol established for the use in our laboratory. Detailed description of the procedures can be found in the Materials and Methods section of the publications.

1.3. Established therapies and new approaches

Current treatments for stroke are very limited, focusing on removal of the clot in the acute phase for fast restoration of blood supply. Pharmacological lysis of the clot with intravenous administration of recombinant tissue plasminogen activator (rt-PA) within the first 4.5 h after the insult is an effective therapy, approved by the US Food and Drug Administration (Albers et al., 2002, Hacke et al., 2008, Hacke et al., 1998, Wahlgren et al., 2008). However, only around 15% of stroke patients arrive at the hospital within this time window and only 10% of the ischemic stroke patients receive this therapy (Minnerup et al., 2011) due to an increased risk of hemorrhage (Hacke et al., 2008). Mechanical endovascular recanalization with a wire system has proven similar effectiveness and can be applied within an extended therapeutic time window for up to 8h post infarction (Clark et al., 2009, Kulcsar et al., 2010, Smith et al., 2008, Smith et al., 2005).

Besides reperfusion therapy for the acute phase, several agents have been reported to rescue damaged brain tissue by modulating the biochemical events following cerebral ischemia. Summarized under the term of neuroprotection these agents target the detrimental effects of excitotoxicity, oxidative stress, inflammation and apoptosis within the ischemic cascade. Over 1000 neuroprotective agents have been tested preclinically (O'Collins et al., 2006) and around 200 have entered clinical trials – but none was able to reproduce effectiveness in the clinics so far (Minnerup et al., 2012). Currently under clinical investigation are growth factors (erythropoietin (Ehrenreich et al., 2002, Ehrenreich et al., 2009, Minnerup et al., 2009), granulocyte colony-stimulating factor (Schabitz et al., 2010)), free radical scavengers (Edaravone (Tohgi et al., 2003); Ebselene (Ogawa et al., 1999), NXY-059 (Lees et al., 2006, Macleod et al., 2008, Shuaib et al., 2007)), antibiotics (Minocycline (Fagan et al., 2010, Lampl et al., 2007)), *N*-Methyl-D-aspartate (NMDA) channel blocker (magnesium sulfate (Saver et al., 2004)) and other neuroprotective strategies like hypothermia, edema amelioration with albumin and anti-hypertensive drugs.

The therapeutic time window for neuroprotective therapy can be extended into the sub-acute phase, for example Edaravone was beneficial when treatment was started within 72 h after stroke onset (Tohgi et al., 2003, Naritomi et al., 2010).

Very few patients are eligible to receive thrombolytic therapy and hundreds of neuroprotective compounds were unsuccessful in clinical trials, therefore new therapeutic strategies begin to focus onto the chronic phase. The main objective of the new strategies is to restore lost function. Potential routes to achieve this goal are being identified, including stem cell transplantation and brain endogenous regenerative processes. Transplantation of various types of cells directly into the ischemic brain or intravenous infusion improved functional outcome in animal models of stroke and first transplantations were already performed on human stroke patients (Bang et al., 2005, Kondziolka et al., 2005, Nelson et al., 2002). Possible mechanisms of action include cell replacement (Oki et al., 2012), trophic support and modulation of the inflammatory processes after ischemia (Lee et al., 2008). It was recently recognized that even the adult brain has some capacity to react to cerebral injury. The endogenous regenerative processes initiated after ischemia include the formation of new blood vessels (angiogenesis) and the endogenous production of new neurons (neurogenesis). These processes may represent promising targets for the development of new therapies.

2. Endogenous regenerative processes after stroke

Early in the ischemic cascade hypoxia-induced up-regulation of growth factors and cytokines initiates the endogenous regenerative processes of angiogenesis and neurogenesis. Angiogenesis is the formation of new blood vessels from pre-existing ones. In the context of cerebral ischemia the angiogenic response describes the whole process of vascular remodeling which possibly translates into an increase of cerebral micro vessel density. Stroke patients with increased vessel density survived longer and showed a better neurological performance (Krupinski et al., 1994, Szpak et al., 1999). Angiogenesis is closely linked to endogenous neurogenesis (Sun et al., 2003). Endogenous neurogenesis describes the formation of new neurons from neural stem cells, which reside in the adult brain. The phenomenon of adult neurogenesis and its responsiveness to injury are well documented in animal models. However, endogenous neurogenesis does not seem potent enough to restore lost neuronal functions. As both processes share signal molecules, e.g. vascular endothelial growth factor (VEGF) (Carmeliet and Tessier-Lavigne, 2005), and manipulation with pro-angiogenic growth factors results in an enhanced neurogenic response to stroke (Wang et al., 2004, Xiong et al., 2010, Li et al., 2011), it is desirable to investigate both

processes in conjunction. The evaluation of their temporal profiles will allow determination of key events within each process, which may represent new therapeutic targets.

2.1. Angiogenesis

Angiogenesis is the formation of new blood vessels. In general, blood vessels can form via two distinct processes: vasculogenesis and angiogenesis. While vasculogenesis denotes de novo formation of vessels from proliferating and differentiating mesoderm-derived endothelial progenitor cells during embryonic development, angiogenesis represents new vessel formation from pre-existing blood vessels. Almost no changes of the cerebral vasculature appear under healthy conditions. However, ischemic injury will trigger molecular and structural changes.

2.1.1. Stroke-induced angiogenesis

The occlusion of a cerebral artery leads to a lack of oxygen (hypoxia) and glucose (hypoglycemia) in the affected brain region. Hypoxia inducible factor 1α (HIF1α) stabilizes under hypoxic conditions and forms a dimer with HIF1β [65] which functions as a transcription factor and binds to the hypoxia-response element (HRE) promoter. Thus, hypoxia triggers the elevation or de novo expression of several growth factors and cytokines, including vascular endothelial growth factor (VEGF), fibroblast growth factor (FGF), transforming growth factor (TGF), hepatocyte growth factor (HGF), platelet-derived growth factor (PDGF), insulin-like growth factor (IGF), epidermal growth factor (EGF) and angiopoietins (Ang1 and Ang2) (Hayashi et al., 2003, Lin et al., 2000).

VEGF is the major effector of angiogenesis (Adams and Alitalo, 2007, Ferrara, 2004). Under healthy conditions low levels function as endothelial survival factor (Ferrara, 1999, Lee et al., 2007). Following stroke, VEGF expression increases starting already 1 h after onset of ischemia (Hayashi et al., 2003). VEGF activates vascular endothelial growth factor receptor 2 (VEGFR2) on endothelial cells and results in endothelial cell proliferation, differentiation and migration. Therefore, an increased expression of VEGFR2 is characteristic for the process of active vascular remodeling after stroke.

Structural changes of the vascular system are initiated in the presence of above listed pro-angiogenic growth factors. Angiogenesis starts with vasodilation and an increase in vascular permeability. Secretion of matrix metalloproteinases (MMPs) results in degradation of the basement membrane and the local extracellular matrix. The inter-endothelial cell contact loosens and endothelial cells start to proliferate. Designated tip cells begin to sprout

into the surrounding space, following chemo-attractive signals of VEGF, that promote the polarized extension of tip cell filopodia. Circulating endothelial progenitor cells are recruited to the site of angiogenesis and integrate into the new sprout. Release of PDGF by the tip cells promotes the recruitment of pericytes to stabilize the new sprout. Eventually, the tip cells encounter another sprout to fuse and establish a continuous lumen. The lumen is most likely formed by intercellular fusion of large vacuoles. Reestablished blood flow improves oxygen delivery and thereby reduces the pro-angiogenic signals. Subsequently, Ang1 signaling leads to maturation and stabilization of the new capillary. A distinct process of so called intussuceptive angiogenesis can also lead to an increase in vessel density without the need of endothelial cell proliferation. The lumen of an existing vessel is divided into two tubes by the deposition of extracellular matrix.

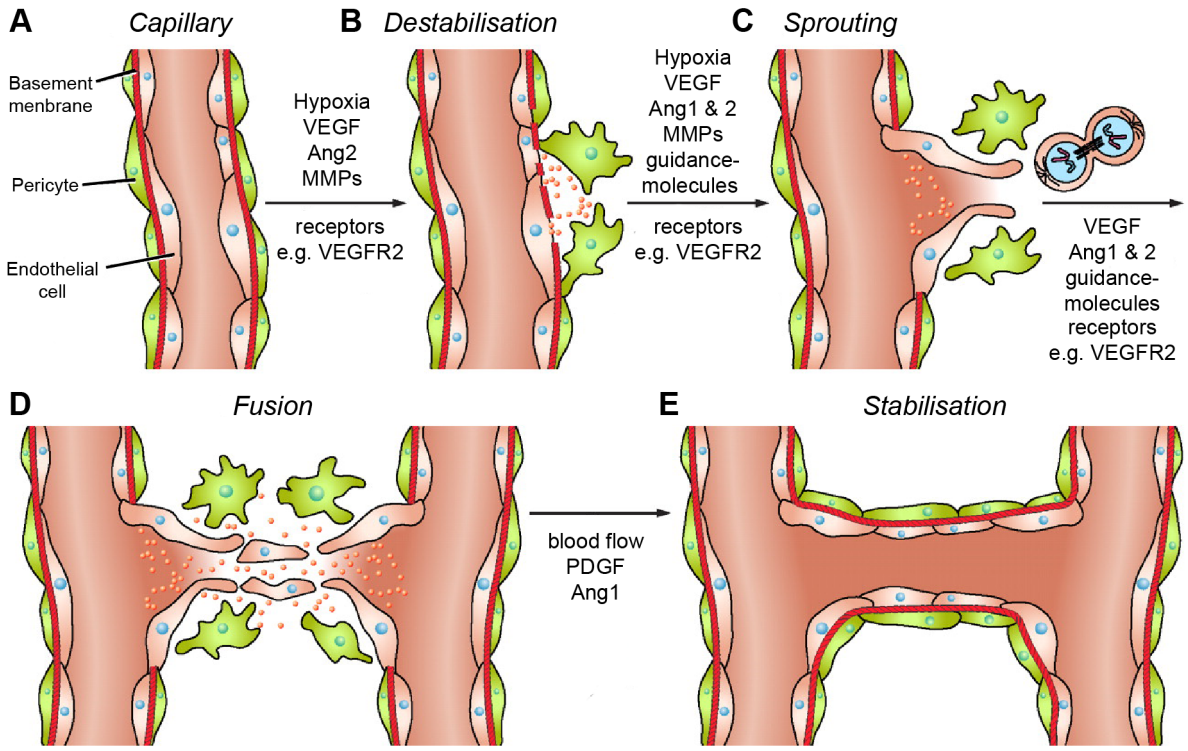

Figure 3: Major steps of post-stroke angiogenesis
A Brain capillaries are formed by endothelial cells, pericytes and basement membrane. **B** Hypoxia changes the expression of pro-angiogenic growth factors, like VEGF and Ang2, which induce destabilization of the endothelial wall. Matrixmetalloproteinases (MMPs) degrade the basement membrane. **C** Proliferating endothelial cells follow guidance molecules and invade the parenchyma to form an endothelial sprout. **D** Fusion of sprouts establish a new caplillary. **E** Re-established blood flow enhances anti-angiogenic signals, including PDGF and Ang1 expression, which results in pericyte recruitment and vessel stabilization. Modified from (Clapp et al., 2009).

2.1.2. Temporal and spatial profile of post-stroke angiogenesis

Initially, ischemic neuronal cell death is accompanied by pronounced vascular regression and endothelial apoptosis within the ischemic core (Bosomtwi et al., 2008, Lin et al., 2008a, Hayashi et al., 2003). Endothelial cell proliferation was detected as early as 3 days after stroke in rodent models of MCAO (Hayashi et al., 2003, Beck et al., 2000). A similar time profile was observed in human stroke patients (Krupinski et al., 1994). Increases in vascular density were discovered in peri-lesional areas starting 3-4 days after stroke (Hayashi et al., 2003, Beck and Plate, 2009). In particular, intensive vascular sprouting was found in the caudo-ventral area next to the subventricular zone in a mouse model of MCAO (Ohab et al., 2006, Thored et al., 2007) and in the pial network of the brain surface in rats with cortical stroke (Lin et al., 2002, Lin et al., 2008a). In some cases, the increase in vessel density was only transient (Thored et al., 2007). Although no increase in vascular density was detected in an embolic model of stroke, changes in cerebral blood flow and volume, as well as increased blood-brain barrier leakage indicate active vascular remodeling in peri-infarct regions (Lin et al., 2008a, Li et al., 2007). As literature gives only few and model-specific pieces of information about the location and the extent of vascular changes, much more knowledge is needed to fully elucidate its spatio-temporal profile.

2.2. Adult neurogenesis

Neurogenesis describes the formation of mature neurons from neuronal stem or progenitor cells. Long time it has been believed that neuronal proliferation in the central nervous system ceases after birth and that the adult mammalian brain does not have the ability to regenerate after injury. However, in 1962 Joseph Altman made the initial discovery that new neurons were continuously added to the adult rat brain. To date, the concept of adult neurogenesis is well established and signs of neurogenesis were confirmed in the adult human brain (Eriksson et al., 1998, Curtis et al., 2007). The adult brain has two established neurogenic regions, the subventricular zone (SVZ) and the subgranular zone (SGZ), where neural stem cells are present and proliferate throughout life (Alvarez-Buylla et al., 2002). The SVZ is located along the lateral ventricles and under physiological conditions gives rise to new interneurons in the olfactory bulb. The architecture of SVZ is subject of intensive research. Slowly dividing, primary neural stem cells located in the SVZ give rise to highly proliferative cells, therefore named transient amplifying cells. From these cells migratory neuroblasts arise, which follow the rostral migratory stream towards the olfactory bulb (Figure 3A). Neural precursor cells begin to express doublecortin (DCX), a microtubule-associated protein, while actively dividing. In particular, the migratory neuroblasts express DCX until they differentiate into mature neurons. The SGZ is located within the dentate gyrus of the

hippocampus. Newly formed neuroblasts migrate only over a short distance into the adjacent granule cell layer and differentiate into granule cells.

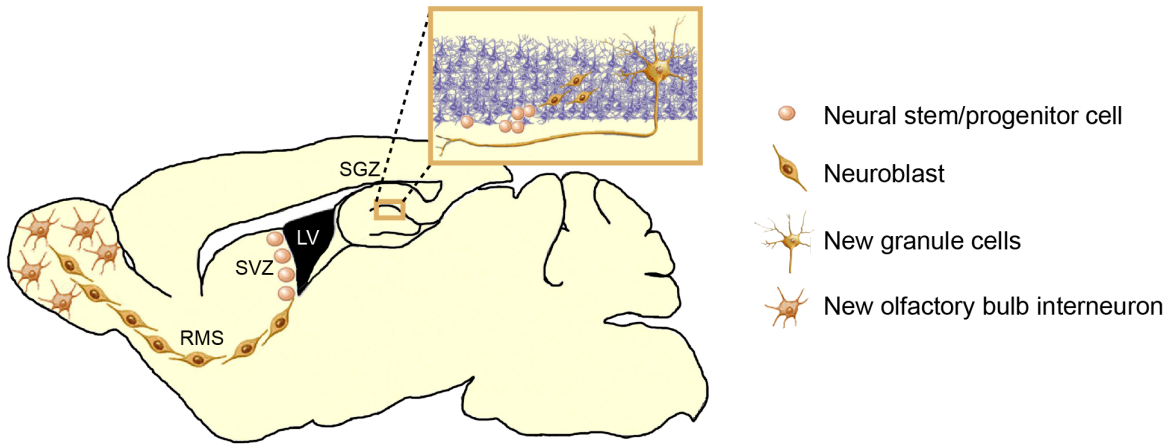

Figure 3: Adult neurogenic niches in the rodent brain
Neural stem/progenitor cells lie within the subventricular zone (SVZ) along the lateral ventricle (LV) and within the subgranular zone (SGZ) within the hippocampus. The former stem/progenitor cells give rise to neuroblasts, which migrate along the rostral migratory stream (RMS) to the olfactory bulb to form olfactory bulb specific interneurons. The stem/progenitor cells of the SGZ give rise to new granule cells of the granule cell layer (see insert). Adapted form (Ekdahl et al., 2009)

2.2.1. Stroke-induced neurogenesis

Cerebral ischemia induces changes in adult neurogenesis. Molecular cues involved in angiogenesis, including FGF, EGF, brain-derived neurotrophic factor, Ang and VEGF signaling, induce increased proliferation of neural stem cells within the SVZ and SGZ (Christie and Turnley, 2013). Neuroblasts of the ipsilateral SVZ, normally migrating to the olfactory bulb, change their direction and follow chemo-attractive signals of VEGF and stromal cell-derived factor 1α towards the site of injury (Zachary, 2005). During this journey they use newly built vessels as travelling scaffold (Ohab et al., 2006). A subset of the arriving neuroblasts differentiates into mature neurons of the appropriate neuronal type and even electrophysiological activity was observed in some studies.

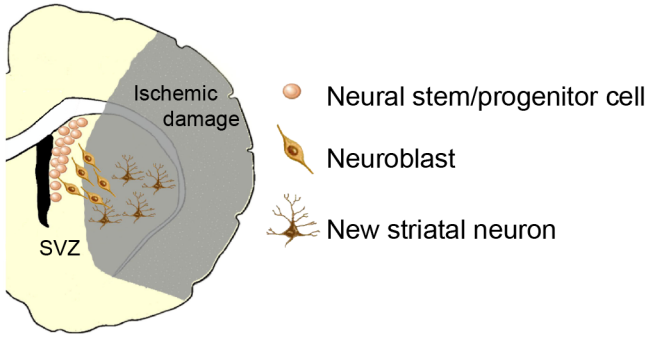

Figure 4: Neurogenic response to ischemia
Subventricular zone (SVZ) neural stem/ progenitor cells increase their proliferation. Neuroblasts migrate into the ischemic striatum and differentiate into the appropriate striatal neuron.

2.2.2. Temporal and spatial profile of post-stroke neurogenesis

Increased proliferation of SVZ neural progenitor cells was observed already 2 days after the onset of ischemia (Jin et al., 2001). In some studies it was found bilaterally but most studies report significantly higher proliferation in the ipsilateral SVZ. Proliferation peaked at 1-2 weeks and returned to normal levels by 3-4 weeks (Thored et al., 2007, Jin et al., 2001, Zhang et al., 2001), although continuous proliferation was observed several months after stroke (Thored et al., 2007). New neurons can be found in the ischemic striatum at 2 weeks after ischemia (Arvidsson et al., 2002, Parent et al., 2002). Some studies also report post-ischemic neurogenesis in the cerebral cortex (Gould et al., 1999, Palmer et al., 2000), but the origin of those cells is being debated. Proliferating cells from the SVZ were seen to migrate into the corpus callosum and the penumbral cortex (Jin et al., 2003) but almost no mature neurons differentiated from these cells were observed at later time points (Arvidsson et al., 2002, Parent et al., 2002).

3. Non-invasive imaging strategies

The angiogenic and neurogenic responses after cerebral ischemia are highly dynamic processes. Traditional experimental methods are invasive and require sacrificing high numbers of animals at many different time points during the experiment to resolve critical steps within those processes. Non-invasive imaging overcomes the limitation of one time point results by allowing the investigation of the whole dynamic process within the physiological or pathological context of the living organism. Thus, non-invasive imaging offers exclusive advantage for the field of regenerative stroke research. The non-invasive observation of biological processes holds the advantage of only mildly affecting the physiological homeostasis an organism. Various techniques exist for small animal imaging based either on optical probes (e.g Bioluminescence Imaging - BLI), magnetic properties (e.g. Magnetic Resonance Imaging - MRI), or radio nucleotides (e.g. Positron Emission Tomography - PET). These methods differ in spatial and temporal resolution, sensitivity, signal specificity and tissue penetration. BLI offers high sensitivity but is limited in spatial resolution. Radiotracer methods are also highly sensitive but offer only slightly higher spatial resolution. Finally, MRI is superior for spatial resolution but is limited in sensitivity. This thesis employs the methods of BLI and MRI for the investigation of regenerative processes after cerebral ischemia.

3.1. Bioluminescence imaging

Bioluminescence imaging (BLI) belongs to the group of optical imaging methods, which are based on the sensitive detection of light to visualize cellular and molecular processes. In the special case of BLI the source of light is a photon-producing enzymatic reaction between a specific enzyme (luciferase) and its specific substrate (luciferin). The phenomenon of bioluminescence has been observed in several species, including jellyfish (Aequorea), sea pansy (Renilla), corals (Tenilla), click beetle (Pyrophorus plagiophthalamus), and several bacterial species (Vibrio fischeri) (Hastings, 1996). The most commonly used bioluminescence reporter for research purposes is the luciferase from the North American firefly (Photinus pyralis) (Figure 5A).

BLI has quickly developed into a powerful tool for non-invasive imaging of cells or molecular processes within a living organism. Although spatial resolution is quite poor due to tissue induced light scattering, BLI offers very high sensitivity. Mammalian cells do not express the enzyme luciferase, so that light emission of the reporter can be unambiguously assigned to the process under investigation, generating images with high signal to noise ratio.

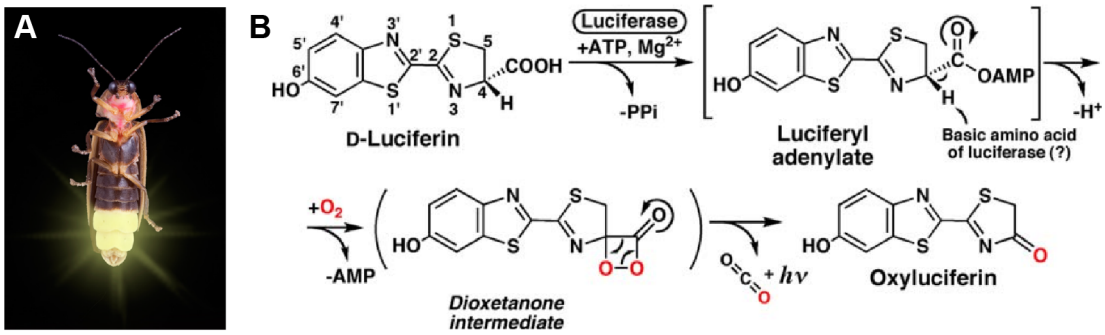

Figure 5: Principles of bioluminescence imaging
A Firefly (Phontinus pyralis) showing the endogenous production of light by a biochemical reaction (www.firefly.org). **B** Oxidation of luciferin by luciferase results in the emission of light (530-640 nm) (Inouye, 2010).

3.1.1. The principles of bioluminescence imaging

The light emitting reaction of luciferase-luciferin interaction varies between the luminous organisms. All reactions rely on an oxidative process with molecular oxygen and the conversion of chemical energy into light (Inouye, 2010). Firefly luciferase produces photons in a two-step reaction that requires ATP, magnesium, and a benzothiazoyl–thiazole luciferin (Wilson and Hastings, 1998). Initially, the firefly luciferase catalyzes the formation of a luciferase-bound luciferyl adenylate in the presence of magnesium and ATP, thereby

releasing an inorganic pyrophosphate (PPi) and adenylating the D-luciferin (Figure 5B). During the second step the adenylated D-luciferin is oxidized to produce an excited state of oxyluciferin. This reaction releases AMP and CO_2. When the excited oxyluciferin relaxes to its ground state, light of a broad spectrum (530–640 nm) is emitted (Figure 6A). This emission spectrum is pH and temperature dependent and further in vivo related factors change the photon emission, which has to be considered for in vivo application.

3.1.2. In-vivo bioluminescence imaging in pre-clinical research

The utilization of BLI for in vivo application includes stable over-expression of the luciferase enzyme as a molecular reporter in mammalian cells. The expression of luciferase allows subsequent sensitive imaging of molecular processes like promotor activity of a gene of interest (Figure 6B+C) or cell tracking of luciferase-expressing cells in the living organisms (Figure 6D) (Contag et al., 1997). Photon emission of the luciferase labeled cells is initiated upon injection of the substrate D-luciferin. Another benefit of BLI is that the light reaction of firefly luciferase is energy dependent, therefore only viable cells contribute to the BLI signal. Different injection routes (subcutaneous sc, intra-peritoneal ip, intra-venous iv) result in distinct light emission kinetics. BLI is simple to execute and allows monitoring of processes over a long period of time, with multiple measurements in the same animal, reducing the number of animals needed and minimizing the effects of biological variation.

Light emission from living tissue is detected by a specialized charged coupled device (CCD) camera, which converts the photon signal into an electrical signal. CCD cameras spatially encode the intensity of incident photons into electrical charge patterns to generate an image. Such cameras are installed in dark chambers and active cooling of the CCD camera reduces the noise of the system.

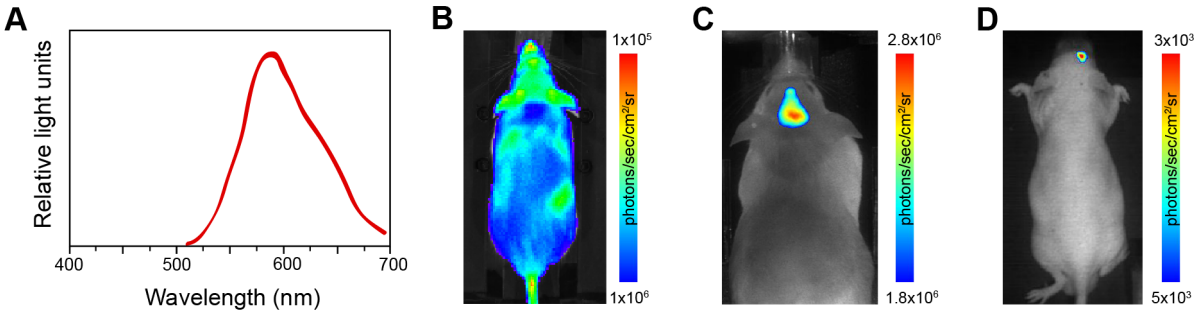

Figure 6: In-vivo application of bioluminescence imaging in this thesis
A Emission spectrum of firefly (Phontinus pyralis) luciferase under in-vivo condition (temperature 37°C, pH=7.4). **B** VEGFR2-luc knock-in mouse, expressing luciferase under the control of the vascular endothelial growth factor VEGFR2 promotor. **C** DCX-luc mouse, expressing luciferase under the control of the doublecortin (DCX) promotor. **D** Implantation of neural stem cells constitutively expressing luciferase enables to track their location.

The sensitivity of light detection is limited by wavelength-dependent absorption through pigments and chromophores in living tissues. Only light of 600 nm and above can penetrate through several centimeters of tissue, allowing the detection of light emitted from deeper structures inside an experimental animal (Sadikot and Blackwell, 2005). Nevertheless, images are surface weighted, meaning that light sources closer to the surface of the animal appear brighter compared to deeper sources, which has to be considered for quantitative analysis (Sutton et al., 2008). The interaction of light and tissue results in signal scattering, which decreases spatial resolution to mm scale.

Stable and reproducible imaging protocols are needed for achieving comparability between measurements at different time points and between different studies. For example, the luciferase reaction is temperature-dependent, indicating the need for close physiological monitoring of the animal's body temperature in order to gain comparable results. A variety of anesthesia and injection routes (sc, ip, iv) of the substrate D-luciferin have been used in literature so far, resulting in different photon emission intensities and kinetics, although the underlying luciferase expression is identical (Virostko et al., 2004, Keyaerts et al., 2008, Inoue et al., 2009, Keyaerts et al., 2011). Furthermore, in the specific case of BLI of the central nervous system substrate availability is aggravated by the presence of the blood-brain barrier (BBB), although luciferin is a small molecular weight molecule und freely diffusible through the BBB. In conclusion, BLI is a powerful tool for longitudinal non-invasive in vivo imaging of small animals, the potential of which can be exploited if an optimal protocol is evaluated for every new application with regard to its aim.

3.2. Magnetic resonance imaging

Magnetic resonance imaging (MRI) is one of the most powerful tools for non-invasive imaging approaches and is commonly used in clinical diagnosis. Compared to other imaging methods, MRI combines high resolution with excellent soft tissue contrast. The underlying physical principle is termed nuclear magnetic resonance (NMR) and was discovered by Purcell and Bloch in 1952. Further work by Lauterbur and Mansfield around 20 years later enabled the use of NMR for imaging (Lauterbur, 1989).

3.2.1. The principle of nuclear magnetic resonance

The basis of NMR lies in the magnetic properties of certain atomic nuclei, which posses a non-zero spin. The spin describes the charge-related rotation of the nucleus around its own axis, which induces magnetic properties to the nucleus similar to those of a bar magnet. The hydrogen nucleus fulfills this requirement and is commonly used for MRI in clinical and pre-

clinical research, because of its abundance in molecules and organisms. The orientation of the proton spins is random under normal conditions. When introduced into an external magnetic field (B_0), the spins will align paralelle or anti-parallel with the external field, resulting in a net sum magnetization along the magnetic field axis M_z (Figure 7A). The proton spins start to precess around the axis M_z with a special frequency, which is dependent on the external magnetic field strength and termed Larmor frequency. The actual MR signal is generated by applying a radiofrequency pulse with Larmor frequency. It induces a flip of the net magnetization into the transverse plane of B_0. The new transverse magnetization (M_T) continues to precess around the M_z axis and induces a current in a conductive coil, which represents the MR signal (Figure 7B). Once the radiofrequency pulse is removed, the M_T magnetization will gradually disappear, by a process called relaxation, until the proton spins reach their equilibrium in realigning with the external magnetic field M_z.

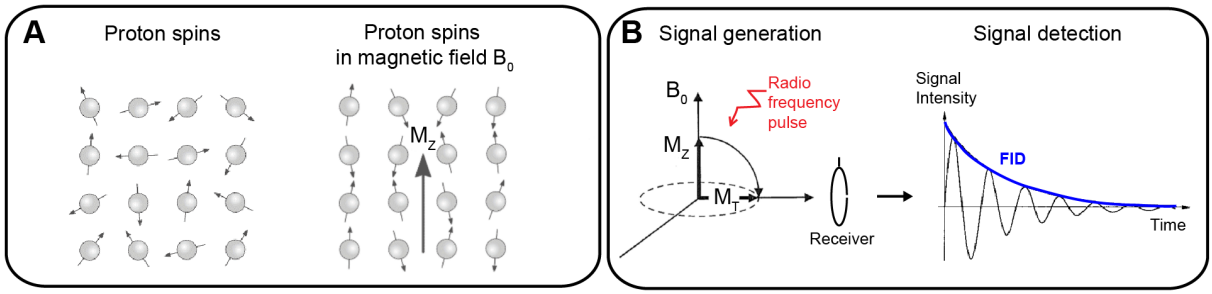

Figure 7: Principles of nuclear magnetic resonance
A Proton spins behave like small bar magnets and can orientate along an external magnetic field. Their magnetization sums up to a net magnetization M_z in the direction of the external field B_0. **B** Proton spins can be excited by a radio frequency wave, so that the net magnetization M_z flips into the xy-plane. Continuous precession of M_z around B_0 results in an electrical signal in a receiver. The signal decreases with tissue specific time curves, the so-called free induction decay (FID). Adapted from (http://wikidoc.org/index.php/Basic_MRI_Physics).

The relaxation can be divided in two distinct components: The transverse relaxation and the longitudinal relaxation. Transverse relaxation describes the decay of the transverse component of the magnetization, which is caused by an exchange of energy between the protons as well as by the impact of constant external inhomogeneities of the magnetic field. This decay is called free induction decay (FID) and follows a specific time constant termed T2* relaxation time (Figure 7B). Utilization of a second radiofrequency pulse, a so-called refocusing pulse, can reverse the impact of external magnetic field inhomogeneities on the signal by generating an echo for signal detection. The amplitude of the echos decays with a tissue specific time constant termed T2 relaxation. The longitudinal component of the net magnetization recovers with a tissue specific time constant T1 until the equilibrium of spin alignment with the external magnetic field is reached. The above described relaxation processes can be used for contrast generation between different types of tissue. Variation of the major parameters of repetition time (TR) and echo time (TE) can be utilized to create

images with enhancement of one relaxation process for contrast generation. Special contrast agents can be introduced into the system, to order to increase contrast for specific applications.

3.2.2. In vivo magnetic resonance imaging in pre-clinical research

Performing MR imaging in small animals requires the position of an anesthetized animal into the center of an external magnetic field created by superconductive coils within an MR system. Several different sequences can be acquired on the same animal during one same imaging session, which illustrates the exceptional potential of this method to assess different aspects of biological structures and processes.

For the application of small animal MRI, field strengths up to 16 tesla are available and highly specialized equipment enables imaging with resolutions down to 50 µm. This allows visualizing fine neuroanatomical structures in small animal brains. Besides imaging of cerebral anatomical structures, MRI can be employed to image cerebral blood flow (CBF), cerebral blood volume (CBV), and oxygenation status of the blood. The integration of these pieces of information can be used to gain knowledge even about brain activity. The use of additional contrast agents can further extend the application range to investigate the functional integrity of the blood-brain barrier and the microvascular architecture.

As in most in-vivo imaging approaches, tight control of the physiological state of the animal is necessary to avoid confounding influence on the measurement. For example, temperature and partial pressure of CO_2 in the blood have effects on the cerebral blood flow and can alter any measurement based on this parameter. Dedicated equipment is needed for physiological monitoring, which allows controlling temperature, respiration rate, heart rate, and oxygen saturation. In conclusion, MRI qualifies for pre-clinical small animal imaging, due to its non-invasive, longitudinal, and especially multimodal characteristics.

3.2.3. Imaging brain vasculature with magnetic resonance

MRI can be employed to image the architecture of large to medium size arteries in the brain (angiography). However, changes following stroke pathology appear predominantly in the microvasculature system. In order to gain information about changes of the microvasculature, measurements of CBF and CBV have been used as correlates (Lin et al., 2002, Jiang et al., 2005, Li et al., 2007, Ding et al., 2008, Hayward et al., 2011). But CBF and CBV based measurements provide relative low specificity for angiogenesis-related vascular changes, since CBF and CBV increases may also arise in response to autoregulatory vasodilation. Therefore, this thesis makes use of the new emerging methodology of steady

state contrast enhanced MRI, which provides direct information about the characteristics of the microvasculature, namely mean vessel density and mean vessel size.

Steady-state contrast-enhanced magnetic resonance imaging

In steady-state contrast-enhanced MRI (SSCE-MRI), transverse relaxation rates R2 and R2* (R2=1/T2, R2*=1/T2*) are measured before and after the administration of an intravascular contrast agent. The difference in relaxivity ΔR2 and ΔR2* within a given voxel can be used to quantify mean vessel density and mean vessel size of that voxel on the basis of mathematical modeling. Monte Carlo simulations showed that ΔR2 is predominantly sensitive to small vessels (<10µm), representing blood volume within the microvasculature, while ΔR2* is sensitive to vessels of all sizes, representing a measure of regional total cerebral blood volume.

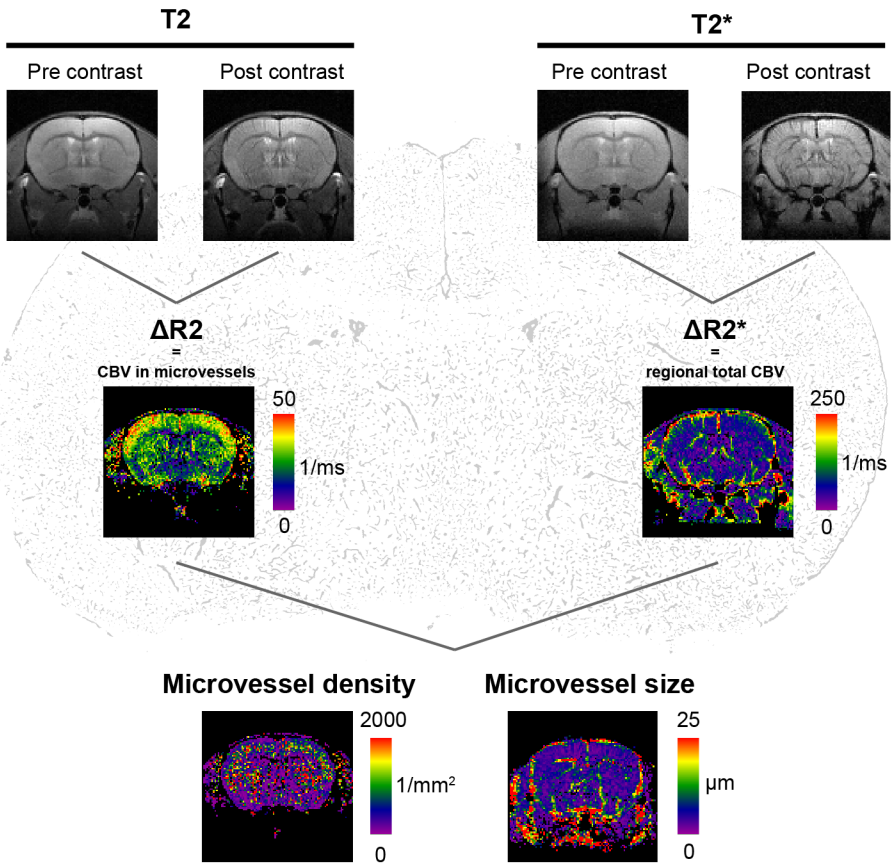

Figure 8: Steady state contrast enhanced MRI
Intravascular injection of superparamagnetic contrast agent results in changes in tissue relaxivity ΔR2 and ΔR2*. ΔR2 represents CBV in microvessels, while ΔR2* represents regional total CBV. Mathematical modeling allows determination of microvessel density and size on a voxel-wise basis.

3.2.4. Imaging brain function with magnetic resonance

Imaging brain function with MRI can employ CBV or CBF changes as a correlate for functional activity but is most commonly performed with blood oxygenation level-dependent (BOLD) contrast. Functional MRI (fMRI) approaches rely on neurovascular coupling, a phenomenon, which describes the vascular response to neuronal activity.

Neurovascular coupling

Neural activity is energy demanding, in particular, the re-uptake of neurotransmitters and the re-establishment of the ion gradients (Attwell and Laughlin, 2001). The exact mechanism by which the brain achieves the tight control of CBF to locally changing energy demands is not yet completely understood and several concepts exist. Local cerebral blood flow is controlled on the arteriole level. Arterioles are surrounded by smooth muscle cells, which can constrict or dilate vessel diameter. Blood flow in capillaries which do not possess smooth muscle cells can be regulated by pericytes serving as capillary sphincters. Originally, decreased oxygen and glucose concentration and increased carbon dioxide concentration were thought to trigger metabolic signals for increased blood flow. However, more recent concepts established that neurotransmitters and lactate, both released by active neurons, are metabolic regulators of blood flow (Attwell et al., 2010). Glutamate activates neuronal NMDA receptors, resulting in neuronal nitric oxide synthase activation and nitric oxide production, which dilates vessels. As part of the neurovascular unit, astrocytic end feet surrounding brain vessels are key players of neurovascular coupling. Upon neural activity, the extracellular presence of neurotransmitters, in particular glutamate, provokes astrocytic release of vasoactive substances, including adenosine, potassium, arachidonic acid and its derivates like prostaglandins, which lead to vasodilation and regionally increased CBF (Iadecola and Nedergaard, 2007, Koehler et al., 2009).

BOLD contrast

BOLD contrast was discovered in the early 90s (Ogawa et al., 1990) and uses the differential magnetic properties of hemoglobin. Hemoglobin consists of 4 subunits, each containing an iron complex. Binding of oxygen changes the molecular conformation and further results in pairing of previously single electrons of the iron atoms. Oxygenated hemoglobin (oxyHb) is diamagnetic and has no effect on the local magnetic field, thus not changing tissue related relaxivity. However, deoxygenated hemoglobin (deoxyHb) is paramagnetic and thereby changes the local magnetic field resulting in small field inhomogeneities which shorten the T2* relaxivity. A blood vessel containing excessive amounts of deoxygenated hemoglobin will induce enhanced signal drop in the tissue surrounding the vessel. Neural activity increases the cerebral metabolic rate of oxygen. This

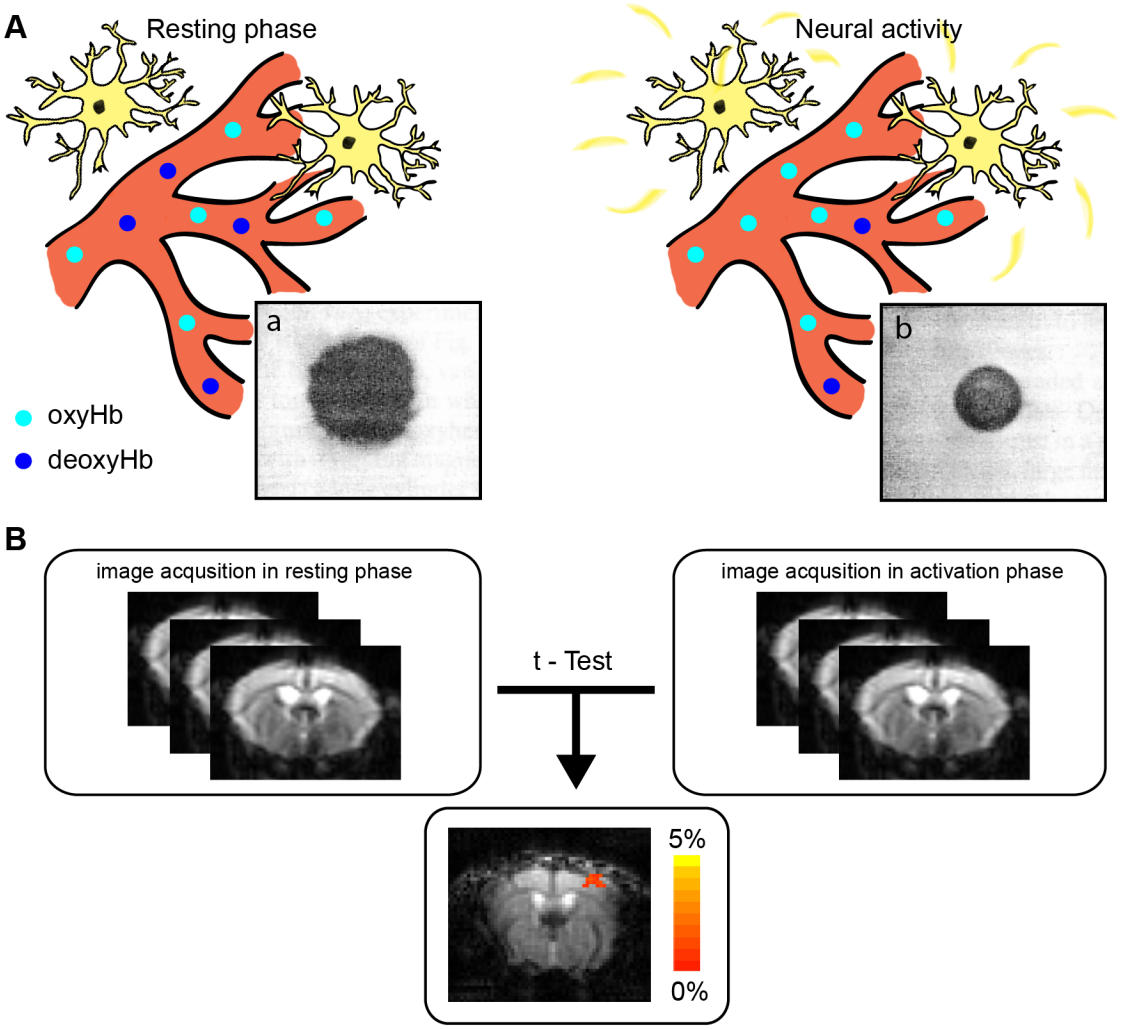

Figure 9: Principle of functional magnetic resonance imaging
A Neural activity increases the energy demand and thereby the supply of oxygenated hemoglobin. In the presence of deoxygenated hemoglobin (deoxyHb) the signal void is stronger than in the presence of oxygenated hemoglobin (oxyHb) (compare inserts of MR images of glass capillaries filled with deoxyHb (insert **a**) and oxyHb (insert **b**); inserts from Ogawa et al. 1990). **B** Repetitive fast imaging during the resting phase and the activation phase allows to statistically determine areas of activation.

increases the amount of deoxyHb and thus enhances signal loss in the area of activation (decreased BOLD signal). However, neural activity also triggers a hemodynamic response as described above, which results in increased CBV and CBF due to vasodilation. The increase in CBF lowers the amount of deoxyHb due to a washout and dilution with fresh, oxygen rich arterial blood. The CBF increase is the dominating process that eventually leads to a net increase in the level of oxyHb at the site of activation, resulting in the BOLD signal. Thus, the BOLD contrast represents an indirect measure of neural activity, with an inherent temporal delay. CBF increase can be detected approximately half a second after the onset of neuronal activity, while BOLD contrast starts shortly afterwards (approximately half a second later) and reaches its maximum only at 6 seconds after neural activity started (Silva et al., 2000). A

typical fMRI experiment acquires MR images during a resting phase and during an activation phase (Figure 9B). Neuronal activation is achieved by a stimulus, most commonly electrical forepaw stimulation. Subsequent statistical comparison of both phases reveals areas with BOLD changes, which are only in the order of a few percent and are visualized in parametric maps.

4. Aims

Stroke is a severe disease with extensive impact on personal life quality. The failure of adequate oxygen supply to the brain quickly leads to widespread cell death and loss of function. Stroke therapy has to prevent cell death or restore cellular circuits in order to retain and restore functional integrity. As neuroprotective therapies could not show beneficial effects for human stroke patients, new hope is laid on restoration therapies. Especially the discovery of the endogenous regenerative capacity of the brain led to several strategies, which aim to enhance the endogenous processes. One strategy is based on the spontaneous revascularization of ischemic tissue, starting early after the insult by the induction of endothelial cell proliferation. Another strategy considers endogenous neuronal stem cells of the established adult neurogenic niches, which respond to stroke by enhanced proliferation and directed migration towards the injured brain area. However, it is not clear if these endogenous mechanisms can be utilized to have an effect on functional recovery. Thorough knowledge about post-stroke angiogenesis and endogenous neurogenesis will reveal potential new therapeutic targets.

The aim of this PhD thesis was to monitor the endogenous regenerative processes of angiogenesis and neurogenesis following cerebral ischemia with new non-invasive imaging methods based on bioluminescence imaging and magnetic resonance imaging. Rat and mouse models of cerebral ischemia were employed and specific transgenic mice were used. Since regeneration is supposed to lead to functional recovery, this thesis also aimed to monitor functional changes of specific brain regions following stroke. As no such method existed for specific application in mice, this thesis established a mouse specific protocol.

Publications

I. **Monitoring angiogenesis after stroke using a VEGFR2-luc mouse model.**
Joanna M. Adamczak, Gabi Schneider, Melanie Nelles, Ivo Que, Ernst Suidgeest, Louise v.d. Weerd, Clemens Löwik, Mathias Hoehn
Angiogenesis (2012), (under review)

II. **Vascular changes after stroke in the rat – a longitudinal study using optimized magnetic resonance imaging.**
Philipp Boehm-Sturm*, Tracy D. Farr*, Joanna Adamczak, Jan Jikeli, Luam Mengler, Dirk Wiedermann, Therése Kallur, Valerij Kiselev, and Mathias Hoehn
Contrast Media and Molecular Imaging (2013) (accepted)
(*: authors contributed equally)

III. **Optimizing bioluminescence sensitivity for noninvasive imaging of neural stem cell grafts in the mouse brain.**
Markus Aswendt*, Joanna Adamczak*, Sebastian Couillard-Depres, Clemens Löwik, Mathias Hoehn
PLoS ONE (2013) 8(2): e55662
(*: authors contributed equally)

IV. **High field BOLD response to forepaw stimulation in the mouse.**
Joanna M. Adamczak, Tracy D. Farr, Jörg Seehafer, Daniel Kalthoff and Mathias Hoehn
NeuroImage (2010). 51(2): 704-712

I.

Monitoring angiogenesis after stroke using a VEGFR2-luc mouse model.

Joanna M. Adamczak, Gabi Schneider, Melanie Nelles, Ivo Que, Ernst Suidgeest, Louise v.d. Weerd, Clemens Löwik, Mathias Hoehn

Angiogenesis (2012), (under review)

Angiogenesis

In vivo bioluminescence imaging of vascular remodeling after stroke

--Manuscript Draft--

Manuscript Number:	
Full Title:	In vivo bioluminescence imaging of vascular remodeling after stroke
Article Type:	Original Article
Keywords:	VEGFR2; flk-1; Cerebral ischemia; Angiogenesis; Vessel density; in vivo bioluminescence imaging
Corresponding Author:	Mathias Hoehn Max Planck Institute for Neurological Research Cologne, GERMANY
Corresponding Author Secondary Information:	
Corresponding Author's Institution:	Max Planck Institute for Neurological Research
Corresponding Author's Secondary Institution:	
First Author:	Joanna Adamczak
First Author Secondary Information:	
Order of Authors:	Joanna Adamczak
	Gabriele Schneider
	Melanie Nelles
	Ivo Que
	Ernst Suidgeest
	Louise van der Weerd, Dr.
	Clemens Löwik
	Mathias Hoehn
Order of Authors Secondary Information:	
Abstract:	Thrombolysis remains the only beneficial therapy for ischemic stroke, but is restricted to a short therapeutic window during the acute phase following the infarct. Currently much research is focusing on spontaneous regeneration processes during the sub-acute and chronic phase. Angiogenesis was described in the border zones of the infarct, but further insight into the temporal profile and the molecular mechanisms is needed to fully apprehend its therapeutic potential. Angiogenesis is a multistep process, involving extracellular matrix degradation, increased blood brain-barrier permeability, endothelial cell proliferation/migration, and, finally, new vessel formation and maturation. Interaction between vascular endothelial growth factor (VEGF) and its receptor 2 (VEGFR2) plays a central role in angiogenic signaling cascades, and VEGFR2 transcription is upregulated following stroke. In the present study we investigated the VEGFR2 expression as a molecular marker for ongoing poststroke angiogenesis. We used a transgenic mouse model expressing firefly luciferase under the control of the VEGFR2 promotor to non-invasively elucidate the temporal profile of VEGFR2 expression after stroke. We found increased VEGFR2 expression up to 14d after the insult, which was paralleled by increased protein levels of VEGFR2 in Western blots of the ischemic cortex and striatum. Further, we observed increased vascular volume in the peri-infarct region and also in the striatal core on histological sections. This mouse model enables non-invasive global tracking of the vascular remodeling process after ischemic stroke, which lasts at least up to 2 weeks after the insult.

In vivo bioluminescence imaging of vascular remodeling after stroke

Joanna M. Adamczak[1], Gabriele Schneider[1], Melanie Nelles[1], Ivo Que[2], Ernst Suidgeest[3], Louise van der Weerd[3,4], Clemens Löwik[2,3], Mathias Hoehn[1]

[1]*In-vivo-NMR Laboratory, Max-Planck-Institute for Neurological Research, Cologne, Germany*
[2]*Department of Endocrinology, Leiden University Medical Center, Leiden, The Netherlands*
[3]*Department of Radiology, Leiden University Medical Center, Leiden, The Netherlands*
[4]*Department of Human Genetics, Leiden University Medical Center, Leiden, The Netherlands*

Running title: Non-invasive VEGFR2 imaging after stroke

Key words: VEGFR2, flk-1, Cerebral ischemia, Angiogenesis, Vessel density

Address correspondence to:
Prof. Dr. Mathias Hoehn
In-vivo-NMR Laboratory
Max Planck Institute for Neurological Research
Gleuelerstrasse 50
D-50931 Köln, Germany
Phone: +49-221-4726 315
Fax: +49-221-4726 337
Email: mathias@nf.mpg.de

Abstract

Thrombolysis remains the only beneficial therapy for ischemic stroke, but is restricted to a short therapeutic window during the acute phase following the infarct. Currently much research is focusing on spontaneous regeneration processes during the sub-acute and chronic phase. Angiogenesis was described in the border zones of the infarct, but further insight into the temporal profile and the molecular mechanisms is needed to fully apprehend its therapeutic potential. Angiogenesis is a multistep process, involving extracellular matrix degradation, increased blood brain-barrier permeability, endothelial cell proliferation/migration, and, finally, new vessel formation and maturation. Interaction between vascular endothelial growth factor (VEGF) and its receptor 2 (VEGFR2) plays a central role in angiogenic signaling cascades, and VEGFR2 transcription is upregulated following stroke. In the present study we investigated the VEGFR2 expression as a molecular marker for ongoing poststroke angiogenesis. We used a transgenic mouse model expressing firefly luciferase under the control of the VEGFR2 promotor to non-invasively elucidate the temporal profile of VEGFR2 expression after stroke. We found increased VEGFR2 expression up to 14d after the insult, which was paralleled by increased protein levels of VEGFR2 in Western blots of the ischemic cortex and striatum. Further, we observed increased vascular volume in the peri-infarct region and also in the striatal core on histological sections. This mouse model enables non-invasive global tracking of the vascular remodeling process after ischemic stroke, which lasts at least up to 2 weeks after the insult.

Introduction

Angiogenesis, the formation of new blood vessels from pre-existing ones, is recognized as a potential new therapeutic target in ischemic stroke [1-3]. Increased vascularization in areas surrounding the infarct has been observed in human [4,5] as well as in animal brain tissue [6-10] and is associated with improved functionality [11-13,4]. These results support the hypothesis, that angiogenesis after stroke is therapeutically advantageous.

The absence of adequate blood supply caused by the blockage of a cerebral artery leads to tissue hypoxia, which triggers the angiogenic response [8,14]. Hypoxia inducible factor 1α is stabilized under hypoxic conditions and dimerizes with HIF1β to form a transcription factor, which binds to the hypoxia responsible element in the promotor region of several hypoxia inducible cytokines and growth factors [15,16]. The most potent angiogenic factor is the vascular endothelial growth factor (VEGF), which exerts its effect through its main receptor, i.e. vascular endothelial growth factor receptor two (VEGFR2) [15,17]. Activation of the VEGFR2 results in endothelial cell proliferation, migration and differentiation and thus plays a key role in adult angiogenesis. VEGFR2 is upregulated as early as 1h poststroke in mouse models of middle cerebral artery occlusion (MCAO), continues to increase for up to one week and decreases thereafter [18,6,8]. This time profile of VEGFR2 expression after stroke is mainly based upon invasive methods like immunohistochemistry, Western blot and mRNA analysis. Non-invasive tracking of VEGFR2 expression as a correlate for angiogenesis after stroke was performed with PET in combination with a VEGFR tracer [18]. Increased VEGFR2 expression was observed in the ischemic hemisphere of rats until 16 days after stroke, and subsequently decreased to almost normal levels at 23 days post-stroke, correlating with immunohistological VEGFR2 quantification. However, a correlation to actual vessel density in the post-stroke tissue is missing in this study.

In the following study we aim to investigate the usefulness of VEGFR2 as a molecular marker for longitudinal observation of post-stroke vascular remodeling. We performed longitudinal and non-

invasive bioluminescence imaging of the VEGFR2 expression following middle cerebral artery occlusion in VEGFR2-luc mice, which express firefly luciferase under the control of the VEGFR2 promoter. After validation of elevated VEGFR2 levels in the ischemic hemisphere, we further investigated the changes in vessel density in immunohistological sections.

Methods

Animal model

All animal experiments were conducted according to the guidelines laid out in the German Animal Welfare Act, in accordance with the European Council Directive 2010/63/EU, and were approved by the Landesamt für Natur, Umwelt und Verbraucherschutz North Rhine-Westphalia, reference number 84-02.04.2011.A123, as well as by the bioethics committee from Leiden University Medical Center, Leiden, The Netherlands, reference number 10215. A transgenic knock-in mouse model [19] which expresses firefly luciferase under the control of the VEGFR2 promotor was used for all experiments. The animals were kept under ad libitum supply of food and water in a 12h/12h day and night cycle. All measurements and surgical interventions were performed under isoflurane anesthesia.

Experimental groups

In total 30 male VEGFR2-*luc* knock-in mice (7-13 weeks old) were randomly assigned into groups of different survival times and different post mortem tissue processing. Six healthy control animals were measured at three different days for the assessment of inter- and intra-animal stability of bioluminescence kinetics from the brain. Subsequently, these mice were sacrificed for Western blotting (n=3) and immunohistochemistry (n=3). Eighteen mice received a 30 min occlusion of the right middle cerebral artery. Of this group, 2 animals were excluded and prematurely sacrificed due to

lack of stroke (n=1) and strong weight loss (n=1). Of the remaining 16 animals, 4 were sacrificed at 7 days and brain tissue was collected for Western blotting (n=2) and immunohistochemistry (n=2). 12 animals were let to survive to 14 days post MCAO and brain tissue was collected for Western blotting (n=6) and immunohistochemistry (n=6). 6 animals received a sham surgery of which 1 had to be excluded due to spontaneous lesion formation detected as hyperintense brain areas on T2-weighted MR images. The remaining 5 sham animals were sacrificed at 14 days post sham surgery. Tissue was collected for Western blotting (n=3) and immunohistochemistry (n=2). MCAO and sham animals were imaged 3 to 7 days before surgery (baseline acquisition) and 3, 7 and 14 days post surgery. Each bioluminescence imaging session was directly followed by a MRI acquisition of T2 maps. Between day 3 and day 7 post surgery, sham and stroke animals received injections of 5-bromo-2'-deoxyuridine (BrdU, Sigma Aldrich, Taufkirchen, Germany) twice daily (50mg/kg). An overview of the study design is presented in Fig. 1a.

Middle cerebral artery occlusion

The ischemic lesion was induced by transient occlusion of the right middle cerebral artery (MCAO), using the intraluminal filament model adapted from rat. The specific surgical method used in this study equals previously described MCAO in mice [20]. Mice were anesthetized with 1-2% isoflurane in a 30/70 oxygen/air mixture and received a subcutaneous injection of 4 mg/kg buprenorphin (Temgesic, Merck, Darmstadt, Germany) for analgesia. A neck incision exposed the common carotid artery and a silicon rubber-coated filament with a tip diameter of 170 µm (7017PK5Re, Doccol Corporation, Sharon, MA USA) was introduced into its lumen. The filament was advanced through the internal carotid artery until it blocked the blood flow to the middle cerebral artery. Animals were allowed to recover under a red light lamp during the occlusion. After 30 min of occlusion, animals were re-anesthetized and reperfusion was initiated by filament removal. The common carotid artery (CCA) was permanently ligated. Sham surgery involved the partial introduction of a filament into the common carotid artery without blocking the blood flow to the MCAO. Animals were also recovered for 30 min and re-anesthetized for filament removal. The CCA was also ligated permanently.

Following MCAO surgery, all animals received s.c. injections of 1 ml NaCl twice daily until the body weight stabilized.

Bioluminescence Imaging

One day prior to the first bioluminescence imaging session, mice were anesthetized in 2% isoflurane and the fur on the head was shaved to allow better photon penetration. It was not necessary to shave the animals a second time during the study. Photon emission (PE) was captured using the IVIS 100 (Perkin-Elmer, Waltham, MA, USA) equipped with a mirror system consisting of two mirrors at a 45° angle to the basis (Fig. 1b). Mice were individually anesthetized in 2% isoflurane and subsequently injected i.p. with 150 mg/kg click beetle luciferin (Promega, Madison, WI, USA) (stock solution 20 mg/ml). The acquisition of photon emission was directly started after luciferin injection. 15 consecutive measurements of 1 min duration were performed in order to capture the inflow kinetics. Photon emission was analyzed for different regions of interest (ROIs; Fig. 1b). Inflow kinetics and photon emission of the 15th min (PE_{15}) after injection were extracted for each ROI. PE_{15} values from the 'ischemic hemisphere' ROI and the 'mirror ischemic' ROI were subsequently normalized to the 'intact hemisphere' / 'mirror intact' ROI and displayed as mean ± standard error of mean.

Magnetic Resonance Imaging

Experiments were performed on a 7 Tesla Bruker Pharmascan 70/16 (Bruker Biospin, Ettlingen, Germany) with a 16 cm horizontal bore magnet and a 9 cm (inner diameter) shielded gradient, a maximum gradient strength of 300 mT/m, and a 23-mm birdcage transmit-receive RF coil (Bruker Biospin, Ettlingen, Germany). A multi slice multi echo (MSME) sequence (TR/TE = 4000 ms /11 ms, 16 echoes, 8 slices, slice thickness 1 mm, FOV 1.5 x 1.5 cm, matrix 128 x 128, resolution 117 x 117 µm) was measured for T2 evaluation and visualization of lesion location. T2 maps were calculated with IDL software (Exelis Visual Information Soution, Boulder, CO, USA).

Western Blotting

Animals were deeply anesthetized and killed by cervical dislocation. Brains were removed quickly and placed in ice cold phosphate buffered saline (PBS). Left and right cortex, as well as left and right striatum were dissected and directly frozen on dried ice. Tissue was stored at -80 °C until further processing. Tissue was lysated in cell lysis buffer (#9803, Cell signaling Technology, Beverly, MA, USA) and treated with protease inhibitor complete Mini (CatNo 04693159001, Roche Applied Science, Indianapolis, Indiana, USA) supplemented with phenylmethylsulphonyl fluoride (PMSF, P6726, Sigma-Aldrich, Taufkirchen, Germany). Protein concentration was determined using the BCA Protein Assay Kit (Pierce, Rockford, IL, USA). For each sample equal amounts of protein were electrophoresed through 8-16% SDS–PAGE gel (Invitrogen, Life Technologies, Darmstadt, Germany) and subsequently electrotransferred to nitrocellulose membranes (ProTran, Whatman, Kent, UK). Membranes were probed with the primary antibodies for VEGFR2 (1:500; #2479, Cell Signaling Technology, Beverly, MA, USA), and β-actin (1:5000; MP Biomedical, Solon, Ohio, USA) overnight at 4°C. For detection, horseradish peroxidase-conjugated secondary antibodies were used (1:3,000 for β-actin, 1:800 for VEGFR2) followed by enhanced chemiluminescence development with Amersham ECL Western Blotting Detection Reagents (GE Healthcare, Buckinghamshire, UK). Results were analyzed using ImageJ software (NIH, rsbweb.nih.gov/ij/). Regions of interest with constant size were positioned over each protein band and the integrated density was quantified followed by background subtraction and normalization to the β-actin signal. Data from the ischemic/sham hemisphere was then normalized to the intact hemisphere and displayed as mean ± standard error of mean.

Immunohistochemistry

Animals were deeply anesthetized and transcardially perfused with ice cold PBS followed by 20 ml 4% paraformaldehyde. Subsequently, brains were removed and shock frozen in -40 °C methylbutane (Sigma-Aldrich, Taufkirchen, Germany). Brain tissue was stored at -80°C until further processing.

Brain sections of 10 µm thickness were cut on the cryostat (Leica Microsystems, Wetzlar, Germany) and stored at -20°C. Sections for BrdU staining were pretreated with 2N hydrochloric acid for 2 hours at room temperature. Prior to immunostaining, sections were pre-incubated at room temperature in 5% normal serum and 0.25% Triton X-100, in KPBS for 45 minutes. Primary antibodies were incubated overnight at 4°C. The following primary antibodies were used for double staining: Anti-laminin (1:100, ab11575, Abcam, Cambridge, UK), anti-GFAP (1:200, G3898, Abcam Cambridge, UK), biotinylated *solanum tuberosum* (potato) lectin (1:100, B-1165, Vector Laboratories, Burlingame, CA, USA), anti-BrdU (1:100, ab6326, Abcam, Cambridge, UK). Secondary antibodies were applied for 2h at room temperature. A biotin-conjugated secondary antibody (1:200, Vector Laboratories, Burlingame, USA) was used with Alexa 488-conjugated streptavidin (1:200, Molecular Probes, Invitrogen, Life Technologies, Darmstadt, Germany). Cy2 and Cy3 (1:200, Jackson Immuno Research, West Grove, PA, USA) were used as complementary secondary antibodies for double staining, and Hoechst 33342 (1:1,000 Invitrogen, Carlsbad, USA) was added during final incubation with secondary antibodies for nuclear staining. Slides were coverslipped with mounting medium (Entellan, Merck, Darmstadt, Germany). Z-stacks of BrdU/lectin positive cells were acquired with a confocal microscope (Leica TCS SP8, Leica Microsystems, Wetzlar, Germany). Laminin/GFAP double staining was used for vascular volume estimation. Microscopic images of whole brain sections were acquired at 4x magnification with a fluorescent microscope (BZ-9000 Keyence, Osaka, Japan). Areas of interest were defined inside the glial scar (‘cortex core’, ‘striatum core’) and outside the glial scar (‘cortex peri’, ‘striatum peri’). From each area of interest 3 images were taken at 20x magnification from the ischemic side and from corresponding areas within the intact hemisphere. Using the Keyence microscope processing software, the area of staining was quantified in these ROIs by thresholding. Clusters of small size (<100 pixels) were regarded as unspecific dirt and were eliminated from the selection. Subsequently, the ratio of the area covered by the staining was calculated for each image and a ratio was made to the corresponding image of the intact hemisphere. A mean was calculated for each region for each animal. Subsequently, a group mean was calculated for each region. Data is presented as group mean ± standard error of mean.

Statistics

Statistical analysis was performed on in vivo BLI data using a repeated measures ANOVA (SPSS version 20, IBM SPSS statistics, Ehningen, Germany) for the time points pre-stroke, 3d and 7d. Post hoc comparisons to the pre-stroke time points within each group were corrected for multiple comparisons using Bonferoni correction. A separate repeated measures ANOVA had to be employed for looking at sham and MCAO animals including the 14d time point. Post hoc comparisons included comparison to pre-stroke time points and comparison between sham and MCAO for each time point with Bonferoni correction. A p-value ≤ 0.05 was considered to be significant and highlighted by * for comparison to the pre-stroke time point, # for comparison to the sham group.

Results

Inter- and intra-animal stability and kinetics of the bioluminescence signal

We characterized the photon emission kinetics from the brain of 6 healthy transgenic mice expressing firefly luciferase under the control of the VEGFR2 promotor. All animals showed increasing photon emission from the brain between 1 to 10 min after luciferin injection. Photon emission (PE) reached a maximum between 10 and 13 min and remained on this level in a steady state until the end of the measurement at 15 min post injection (Fig. 2b). PE kinetics and intensity from the right hemisphere were equal to the left hemisphere for each individual animal (Fig. 2b). We continued to evaluate the photon emission during the 15^{th} minute after luciferin injection (PE_{15}), which represents photon emission during the steady state phase. Healthy animals were measured at three consecutive days for the assessment of inter- and intra-animal stability. Repetitive MRI on the healthy subjects reveals stable T2 values between time points and equality of both hemispheres (Fig. 2a). Corresponding BLI of this exemplary animal, presented as color-coded PE_{15}, confirm the equality of the hemispheres, as well as a stable PE_{15} between time points (Fig. 2a). Repeated measurement of the same animal resulted in absolute PE_{15} variation from 3 to 30% of the mean (Fig. 2c). Absolute signal intensity variation

between animals was 20 to 45% of the mean (Fig. 2, b + c). In order to investigate BLI changes over time, we corrected for inter- and intra-individual variation by normalizing the ischemic (right) to the intact (left) hemisphere.

Cerebral ischemia

Cerebral ischemia was induced by 30 min occlusion of the right MCA with a silicone rubber-coated filament. Lesion size, location and development were assessed by MRI using quantitative T2 maps. Lesions appear as areas of increased T2 values on T2 maps, and a representative lesion is displayed in Fig. 3a. Lesions were of similar size throughout all groups, including damage in the striatum and the parietal cortex, except for one animal of the 7d immunohistochemistry (IHC) group that showed only a small striatal infarct. However, three animals of the 14d Western Blot (WB) group showed larger lesions (including larger parts of the parietal cortex), thus slightly increasing the average lesion size of the WB group compared to the IHC group. The different lesion size of these three animals is probably due to their genetic background, since these three animals were siblings. At 14 days after MCAO, the ischemic hemisphere has shrunken in size, giving space to cerebrospinal fluid, which is visible as a rim of increased T2 value along the ischemic cortex (Fig. 3a).

Bioluminescence of VEGFR2 expression after stroke

Before MCAO, T2 maps displayed no signs of lesion and photon emission was comparable for the right and left hemisphere (Fig. 3a, first row). Three days after MCAO, vasogenic edema resulted in increased T2 values, and a clear lesion was visible in the right hemisphere on T2 maps (Fig. 3a, second row). At this point, photon emission of the ischemic hemisphere was already significantly increased (Fig. 3d) indicating an upregulation of VEGFR2 expression. Photon emission continued to increase from the ischemic hemisphere and was clearly visible on BL images on 7d and 14d after MCAO (Fig. 3a, 3rd and 4th row). The maximal PE increase of 58 ± 36 % in the ischemic hemisphere

was observed 7d post MCAO in the top view (Fig. 3d, left graph). The PE increase was even more pronounced (78 ± 26 %) when observed through the mirror system (Fig. 3d, right graph). At the last observation time point of 14d post MCAO, the photon emission was still strongly increased in the ischemic hemisphere in both, the top view (44 ± 34 %) and the mirror view (65 ± 26 %). The stroke-induced changes in photon emission were significant for all 3 post-stroke time points when compared to pre-stroke values (3d: $p=0.001$; 7d: $p<0.001$; 14d: $p<0.001$; repeated measures ANOVA $F(1.72, 34.438)=6.85$ $p=0.005$ with Bonferroni correction for multiple comparisons). The BLI kinetics, composed of an inflow phase and a steady state phase as observed in healthy control mice, are not changed in the pathological condition of ischemia. Although photon emission from the ischemic hemisphere rises faster during the inflow phase, a steady state phase is reached after 10 min with higher photon emission than from the steady state phase of the intact hemisphere (Fig. 3c).

Sham surgery (introduction of the filament into the ICA but without advancing it to occlude the MCA) did not result in lesion formation (cf. T2 maps in Fig. 3b), but, nevertheless, resulted in a transient change in PE on the ispilateral hemisphere (Fig.ure 3, B+D). Three days after surgery, the increase in emission was of similar magnitude as observed in the MCAO group (top view: 28 ± 17%; mirror view: 58 ± 31%) and was significantly different from pre-surgery values ($p=0.005$). Although emission from the sham hemisphere stayed elevated at 7d and 14d, the change to the pre-surgery values was no longer significant (Fig. 3d). The upregulation of VEGFR2 expression was significantly higher in MCAO animals when compared to sham animals at 7d ($p=0.022$) and at 14d ($p=0.044$) (repeated measures ANOVA $F(3.444, 34.438)=7.333$ $p<0.001$ with Bonferroni correction). Sham was significantly different from healthy animals only at 3d post surgery ($p=0.004$), but no longer thereafter. The BLI kinetics of sham animals show similar behavior of the intact and the sham hemisphere, with slightly higher PE from the sham hemisphere (Fig. 3c).

Western blot analysis

Western blot analysis of healthy control animals shows little change in VEGFR2 expression between left and right hemisphere (Fig. 4). MCAO results in changes in VEGFR2 protein content of the ischemic hemisphere. Western blot of VEGFR2 confirmed elevated levels of VEGFR2 protein in the ischemic cortex and striatum at 7d and 14d post MCAO (Fig. 4, a+b). Quantification revealed a 40 ± 21% increase in the ischemic cortex and a 32 ± 43% increase in the ischemic striatum at 14d after surgery (Fig. 4c). Sham surgery resulted in elevated levels of VEGFR2 protein in the cortex (21 ± 16%), but an apparent decrease in the striatum (-16 ± 14%) (Fig. 4c).

Immunochistochemistry

Histology was performed on the brains to determine changes in vascular volume after MCAO. 10-µm-thick brain sections were therefore stained with Laminin with the stained area interpreted as vascular volume approximation. GFAP staining was used for characterization of astrocyte activation in association with the ischemic lesion. Overview images were acquired for identification of the four areas of interest: the core lesion in the cortex (cortex core), the peri-infarct area the cortical lesion (cortex peri), the striatal core lesion (striatum core), and the peri-infarct area of the striatal lesion (striatum peri). Three close-ups of 20x magnification were taken from each area of interest and from corresponding sites of the intact hemisphere. Fig. 5a shows representative close-ups of each region. As a measure for vascular volume changes, the area positive for laminin was compared between the ischemic hemisphere and the corresponding regions on the contralateral hemisphere (% area, normalized to contralateral side). Vascular volume was strongly reduced in the cortical core region in the MCAO animals (16 ± 5 % reduction), and less so in the sham-operated animals. The striatal core, the striatal peri, and the cortical peri regions all showed an increased vascular volume of (21% ± 6 %), (26% ± 4%) and (14% ± 3%), respectively (Fig. 5b). Sham animals did not show significant differences between the hemispheres in any of these regions. We further investigated the presence of newly formed endothelial cells as possible source for the increased vascular volume using BrdU

staining. In each region that showed increased vascular volume, we found several endothelial cells with incorporated BrdU (Fig. 5c), proving that dividing endothelial cells may be the source of newly formed blood vessels between day 3 and 7 after stroke.

Stroke-induced angiogenesis is detectable with the VEGFR2-luc mouse model

MCAO resulted in increased PE from the ischemic hemisphere. In a cluster analysis presentation of the group averages, this increase was corroborated by increased VEGFR2 protein content in the ischemic striatum and cortex (Fig. 6a) and also by increased vascular volume in the peri-infarct areas of the cortex and striatum (Fig. 6b). Healthy control mice and sham animals showed only minor changes in BLI, minor changes in VEGFR2 expression and minor changes in vessel density from the left and right hemisphere, building a separate and distinct cluster around 1 (Fig. 6, a+b). The BLI signal recorded by the CCD camera is a two dimensional image from the three dimensional structure of the brain. Signals from deeper structures of the brain are subjected to stronger absorption by overlaying tissue than signals from structures closer to the brain surface. Additionally, the half-life of both proteins, VEGFR2 and luciferase, may be substantially different, resulting in a (partially) decoupled BLI signal. This could explain the lack of a tight correlation between the PE intensity and VEGFR2 protein content, or between PE intensity and vascular volume. A time delay between VEGFR2 expression and the occurrence of laminated microvessels will confound the correlation at the 14d time point. However, stroke-induced increased BLI was paralleled by increased VEGFR2 content and increased vascular volume. This is observed in a correlation between VEGFR2 protein content and vascular volume following stroke (striatum $r = 0.97$, cortex $r = 0.67$).

Discussion

J.M. Adamczak *et al*. Non-invasive VEGFR2 imaging after stroke

We have non-invasively observed the temporal profile of VEGFR2 expression after cerebral ischemia as a potential molecular reporter for poststroke angiogenesis, while we followed lesion development with the complementary method of MRI. VEGFR2 plays a key role in post-ischemic vascular remodeling and we found increased expression lasting up to 14d post MCAO, which was paralleled by an increased vascular volume in distinct peri-infarct areas.

Methodological considerations

Bioluminescence imaging is a very sensitive method and allows the detection of even small changes in cell numbers [21]. However, it has a poor spatial resolution. For the first time we report the additional observation of photon emission (PE) through two 45° angled mirrors for a better discrimination of left and right hemisphere through lateral views. Signal changes were consistently greater with intensity readouts from the mirror views, but variation of the signal was also increased, suggesting the introduction of additional noise. In vitro, a linear correlation exists between PE and number of luciferase expressing cells. In vivo this relation is affected by luciferin distribution and photon absorption and scattering by tissue [22-24]. Bioluminescence imaging of the brain has to deal with limited substrate diffusibility through the blood brain-barrier (BBB) [25]. Brain pathologies, which result in a breakdown of the BBB, impose even further methodological obstacles towards the interpretation of the photon emission. An open BBB may facilitate luciferin inflow on the ischemic hemisphere, thus resulting in higher photon emission due to higher substrate availability, instead of higher luciferase content. Photon emission will rise faster, when substrate availability is higher, which was illustrated in the comparison between i.v. and i.p. substrate application [21]. In order to gain insight into the possible effect of an open BBB, we recorded PE already during the luciferin inflow phase with a temporal resolution of 1 min. Subsequently, we compared the inflow behavior between the intact and the ischemic hemisphere. The ascent was faster in the ischemic hemisphere, indicating faster substrate availability through a disturbed BBB. Nevertheless, emission reached a steady state at maximal PE in the ischemic and in the intact side, suggesting that a constant level of substrate is

reached in the brain and is maintained. In this steady-state phase the difference in signal intensity will be due to the difference in luciferase content, rather than substrate concentration. We can therefore conclude that BBB breakdown in this model does not result in higher substrate availability in the ischemic side, and the increase in photon emission during steady-state can be solely attributed to increased VEGFR2 expression.

VEGFR2 upregulation during post-stroke angiogenesis

In order to non-invasively monitor VEGFR2 expression following stroke, we made use of a transgenic mouse expressing luciferase under the control of the VEGFR2 promotor [19]. We observed increasing bioluminescence intensity after cerebral ischemia in the ischemic hemisphere, which peaked at 7d post-stroke. In agreement to previous reports [18,6,8], our results show a continuous increase in VEGFR2 expression from 3d to 7d post-stroke. We observe still significantly elevated expression at 14d post-stroke, which was confirmed by increased VEGFR2 protein content in the ischemic hemisphere compared to the intact hemisphere. Semi-quantitative analysis of regional VEGFR2 content in the brain by Western blotting indicates strong vascular remodeling in the ischemic striatum, since the amount of VEGFR2 was increased by as much as 40%. Also sham surgery resulted in a lower transient increase in BLI signal from the sham hemisphere, indicating an upregulated VEGFR2 expression. Western blot results show a slightly increased VEGFR2 content at 14d post surgery in the right cortex, but not in the striatum of sham animals. Sham surgery involved the introduction of a filament only into the common carotid artery (CCA). Upon removal of the filament, the CCA was ligated permanently to control for blood flow changes induced by the permanent ligation of the CCA in the stroke group. CCA occlusion is used as a model for mild hypoxia and chronic cerebral hypoperfusion [26,27]. Following the occlusion of the internal carotid artery (ICA), Hecht et al. observed reduction by 80% in overall cerebral blood flow, while cortical perfusion was not notably changed. Unilateral CCA occlusion did not result in neuronal cell death within the territory of the MCAO [27], but at 21d after ICA occlusion, slightly increased vessel density was noted in the

ipsilateral cortex [26]. Although our study did not indicate a strong increase in cortical or striatal vascular volume, BLI was sensitive enough to detect the minor changes in VEGFR2 expression induced by mild hypoxia after CCA occlusion.

Vascular volume increase

We investigated the vascular volume in a core region and in a peri-infarct region of the cortex and the striatum. Our MCAO model resulted in strong reduction in vascular volume within the cortical core region. Similar observations were made by Bosomtwi et al. [28] in a distal MCAO rat model. Yet, in the region defined as striatum core, we detected an increase in vessel density. High upregulation of VEGFR2 in the striatum, as indicated by the Western blot results, may have possibly contributed to early enhanced endothelial survival due to its protective properties [29-32] which may then have been followed by new vessel recruitment. As reported by previous studies [6-8,12,9], we observed increased vascular volume in the peri-infarct striatum (26% ± 4) and peri-infarct cortex (16% ± 5%). The samples on which the striatal peri-infarct vascular volume is based include the most dorsal part of the striatum close to the subventricular zone (SVZ), which has been described as highly angiogenic [9,33]. Strong endothelial cell proliferation was observed in this area next to the SVZ between 1 and 2 weeks, and consequently increased vessel density persisted up to 16 weeks [9]. Previous studies reported endothelial cell proliferation started as early as 24h after MCAO in mice [6], and increased vessel density was detectable at 2-3d post-stroke [6,8]. The number of microvessels remained increased up to 21d [6]. In all three regions with increased vascular volume we detected several new endothelial cells, which were newly generated in the first week after stroke. However, new vessels can also form without endothelial cell proliferation through a process called intussusception [34]. Peripheral bone marrow-derived endothelial progenitor cells contributed to vessel formation or stabilization [35]; especially high numbers of endothelial progenitor cells were found beneficial for stroke patients [36]. We did not quantify the numbers of newly generated endothelial cells, since our

main objective was to investigate the impact of VEGFR2 signaling on new vessel formation, regardless of their origin.

Bioluminescence of angiogenesis

The bioluminescence signal change showed increased VEGFR2 expression within the ischemic hemisphere. Western blot analysis revealed increased VEGFR2 protein concentration in ischemic striatum as well as in the cortex. In both, peri-infarct cortex and striatum, as well as in the striatal core increased VEGFR2 expression translated into increased vascular volume. VEGFR2 is mainly expressed on endothelial cells and functions as transducer of survival, proliferation, migration and differentiation cues [15]. Following stroke, the number of VEGFR2 positive endothelial cells was strongly increased in the penumbra [7]. Although very early studies reported that VEGFR2 was expressed solely on endothelial cells, later studies found VEGFR2 expression as well in post-ischemic neurons [14,6]. Furthermore, inhibition of VEGFR2 resulted in decreased neurogenesis and decreased arrival of newly formed neuroblasts in the ischemic striatum [7]. Neuroprotection may therefore be another important function of VEGFR2 upregulation besides the promotion of angiogenesis.

VEGFRs have been also found to be upregulated on astrocytes following stroke [6]. Although VEGFR2 expression was found on reactive astrocytes [37] and microglia/macrophages [38] following stroke, other groups could not reproduce these results [39]. Further, a distinct pattern, where astrocytes express VEGFR1 and endothelial cells express VEGFR2 was suggested [40]. These conflicting results, however, imply caution for the interpretation of the BLI signal expressing solely ongoing angiogenesis.

Conclusion

We monitored the temporal profile of vascular changes following transient cerebral ischemia and established the usability of the VEGFR2-luc mouse model for non-invasive tracking of angiogenesis

in stroke pathology. The present study detected angiogenesis within the first two weeks after stroke and imaged lesion evolution in parallel. Future studies will benefit from this non-invasive tool for investigation of the angiogenic activity beyond this time window.

Acknowledgements:

This work was financially supported by grants from the Volkswagen Foundation (I/83 443) and the EU-FP7 program ENCITE (HEALTH-F5-2008-201842) and TargetBraIn (HEALTH-F2-2012-279017). Special thanks to Ulla Uhlenkücken for help with the preparation of Fig.ures.

References

1. Navaratna D, Guo S, Arai K, Lo EH (2009) Mechanisms and targets for angiogenic therapy after stroke. Cell adhesion & migration 3 (2):216-223

2. Shibuya M (2009) Brain angiogenesis in developmental and pathological processes: therapeutic aspects of vascular endothelial growth factor. The FEBS journal 276 (17):4636-4643. doi:10.1111/j.1742-4658.2009.07175.x

3. Slevin M, Kumar P, Gaffney J, Kumar S, Krupinski J (2006) Can angiogenesis be exploited to improve stroke outcome? Mechanisms and therapeutic potential. Clin Sci (Lond) 111 (3):171-183. doi:10.1042/CS20060049

4. Krupinski J, Kaluza J, Kumar P, Kumar S, Wang JM (1994) Role of angiogenesis in patients with cerebral ischemic stroke. Stroke; a journal of cerebral circulation 25 (9):1794-1798

5. Szpak GM, Lechowicz W, Lewandowska E, Bertrand E, Wierzba-Bobrowicz T, Dymecki J (1999) Border zone neovascularization in cerebral ischemic infarct. Folia neuropathologica / Association of Polish Neuropathologists and Medical Research Centre, Polish Academy of Sciences 37 (4):264-268

6. Hayashi T, Noshita N, Sugawara T, Chan PH (2003) Temporal profile of angiogenesis and expression of related genes in the brain after ischemia. Journal of cerebral blood flow and metabolism : official journal of the International Society of Cerebral Blood Flow and Metabolism 23 (2):166-180

7. Li WL, Fraser JL, Yu SP, Zhu J, Jiang YJ, Wei L (2011) The role of VEGF/VEGFR2 signaling in peripheral stimulation-induced cerebral neurovascular regeneration after ischemic stroke in mice. Experimental brain research Experimentelle Hirnforschung Experimentation cerebrale 214 (4):503-513. doi:10.1007/s00221-011-2849-y

8. Marti HJ, Bernaudin M, Bellail A, Schoch H, Euler M, Petit E, Risau W (2000) Hypoxia-induced vascular endothelial growth factor expression precedes neovascularization after cerebral ischemia. The American journal of pathology 156 (3):965-976. doi:10.1016/S0002-9440(10)64964-4

9. Thored P, Wood J, Arvidsson A, Cammenga J, Kokaia Z, Lindvall O (2007) Long-term neuroblast migration along blood vessels in an area with transient angiogenesis and increased vascularization after stroke. Stroke; a journal of cerebral circulation 38 (11):3032-3039. doi:10.1161/STROKEAHA.107.488445

10. Beck H, Acker T, Wiessner C, Allegrini PR, Plate KH (2000) Expression of angiopoietin-1, angiopoietin-2, and tie receptors after middle cerebral artery occlusion in the rat. The American journal of pathology 157 (5):1473-1483. doi:10.1016/S0002-9440(10)64786-4

11. Lee HJ, Kim KS, Park IH, Kim SU (2007) Human neural stem cells over-expressing VEGF provide neuroprotection, angiogenesis and functional recovery in mouse stroke model. PloS one 2 (1):e156. doi:10.1371/journal.pone.0000156

12. Reitmeir R, Kilic E, Reinboth BS, Guo Z, ElAli A, Zechariah A, Kilic U, Hermann DM (2012) Vascular endothelial growth factor induces contralesional corticobulbar plasticity and functional neurological recovery in the ischemic brain. Acta neuropathologica 123 (2):273-284. doi:10.1007/s00401-011-0914-z

13. Wang Y, Galvan V, Gorostiza O, Ataie M, Jin K, Greenberg DA (2006) Vascular endothelial growth factor improves recovery of sensorimotor and cognitive deficits after focal cerebral ischemia in the rat. Brain research 1115 (1):186-193. doi:10.1016/j.brainres.2006.07.060

14. Beck H, Plate KH (2009) Angiogenesis after cerebral ischemia. Acta neuropathologica 117 (5):481-496. doi:10.1007/s00401-009-0483-6

15. Ferrara N, Gerber HP, LeCouter J (2003) The biology of VEGF and its receptors. Nature medicine 9 (6):669-676. doi:10.1038/nm0603-669

16. Hayashi T, Deguchi K, Nagotani S, Zhang H, Sehara Y, Tsuchiya A, Abe K (2006) Cerebral ischemia and angiogenesis. Current neurovascular research 3 (2):119-129

17. Koch S, Tugues S, Li X, Gualandi L, Claesson-Welsh L (2011) Signal transduction by vascular endothelial growth factor receptors. The Biochemical journal 437 (2):169-183. doi:10.1042/BJ20110301

18. Cai W, Guzman R, Hsu AR, Wang H, Chen K, Sun G, Gera A, Choi R, Bliss T, He L, Li ZB, Maag AL, Hori N, Zhao H, Moseley M, Steinberg GK, Chen X (2009) Positron emission tomography imaging of poststroke angiogenesis. Stroke; a journal of cerebral circulation 40 (1):270-277. doi:10.1161/STROKEAHA.108.517474

19. Lyons SK, Clermont AO, Neben TY, Campbell K, Coffee R, Hunter J, Purchio TF, Jenkins DE (2005) Non-invasive in vivo bioluminescent imaging of tumor angiogenesis in mice. AACR Meeting Abstracts 2005 (1):903-b-

20. Bahmani P, Schellenberger E, Klohs J, Steinbrink J, Cordell R, Zille M, Muller J, Harhausen D, Hofstra L, Reutelingsperger C, Farr TD, Dirnagl U, Wunder A (2011) Visualization of cell death in mice with focal cerebral ischemia using fluorescent annexin A5, propidium iodide, and TUNEL staining. Journal of cerebral blood flow and metabolism : official journal of the International Society of Cerebral Blood Flow and Metabolism 31 (5):1311-1320. doi:10.1038/jcbfm.2010.233

21. Keyaerts M, Verschueren J, Bos TJ, Tchouate-Gainkam LO, Peleman C, Breckpot K, Vanhove C, Caveliers V, Bossuyt A, Lahoutte T (2008) Dynamic bioluminescence imaging for quantitative tumour burden assessment using IV or IP administration of D: -luciferin: effect on intensity, time kinetics and repeatability of photon emission. European journal of nuclear medicine and molecular imaging 35 (5):999-1007. doi:10.1007/s00259-007-0664-2

22. Inoue Y, Kiryu S, Izawa K, Watanabe M, Tojo A, Ohtomo K (2009) Comparison of subcutaneous and intraperitoneal injection of D-luciferin for in vivo bioluminescence imaging. European journal of nuclear medicine and molecular imaging 36 (5):771-779. doi:10.1007/s00259-008-1022-8

23. Keyaerts M, Heneweer C, Gainkam LO, Caveliers V, Beattie BJ, Martens GA, Vanhove C, Bossuyt A, Blasberg RG, Lahoutte T (2011) Plasma protein binding of luciferase substrates influences sensitivity and accuracy of bioluminescence imaging. Molecular imaging and biology : MIB : the official publication of the Academy of Molecular Imaging 13 (1):59-66. doi:10.1007/s11307-010-0325-x

24. Virostko J, Chen Z, Fowler M, Poffenberger G, Powers AC, Jansen ED (2004) Factors influencing quantification of in vivo bioluminescence imaging: application to assessment of pancreatic islet transplants. Molecular imaging 3 (4):333-342. doi:10.1162/1535350042973508

25. Berger F, Paulmurugan R, Bhaumik S, Gambhir SS (2008) Uptake kinetics and biodistribution of 14C-D-luciferin--a radiolabeled substrate for the firefly luciferase catalyzed bioluminescence reaction: impact on bioluminescence based reporter gene imaging. European journal of nuclear medicine and molecular imaging 35 (12):2275-2285. doi:10.1007/s00259-008-0870-6

26. Hecht N, He J, Kremenetskaia I, Nieminen M, Vajkoczy P, Woitzik J (2012) Cerebral Hemodynamic Reserve and Vascular Remodeling in C57/BL6 Mice Are Influenced by Age. Stroke; a journal of cerebral circulation. doi:10.1161/STROKEAHA.112.653204

27. Pimentel-Coelho PM, Michaud JP, Rivest S (2012) Effects of mild chronic cerebral hypoperfusion and early amyloid pathology on spatial learning and the cellular innate immune response in mice. Neurobiology of aging. doi:10.1016/j.neurobiolaging.2012.06.025

28. Bosomtwi A, Chopp M, Zhang L, Zhang ZG, Lu M, Jiang Q (2011) Mean microvessel segment length and radius after embolic stroke: Comparison of magnetic resonance imaging (MRI) and laser scanning confocal microscopy (LSCM). Brain research 1381:217-227. doi:10.1016/j.brainres.2011.01.009

29. Ferrara N (2004) Vascular endothelial growth factor: basic science and clinical progress. Endocrine reviews 25 (4):581-611. doi:10.1210/er.2003-0027

30. Hermann DM, Zechariah A (2009) Implications of vascular endothelial growth factor for postischemic neurovascular remodeling. Journal of cerebral blood flow and metabolism : official journal of the International Society of Cerebral Blood Flow and Metabolism 29 (10):1620-1643. doi:10.1038/jcbfm.2009.100

31. Lee S, Chen TT, Barber CL, Jordan MC, Murdock J, Desai S, Ferrara N, Nagy A, Roos KP, Iruela-Arispe ML (2007) Autocrine VEGF signaling is required for vascular homeostasis. Cell 130 (4):691-703. doi:10.1016/j.cell.2007.06.054

32. Shibuya M (2006) Differential roles of vascular endothelial growth factor receptor-1 and receptor-2 in angiogenesis. Journal of biochemistry and molecular biology 39 (5):469-478

33. Ohab JJ, Fleming S, Blesch A, Carmichael ST (2006) A neurovascular niche for neurogenesis after stroke. The Journal of neuroscience : the official journal of the Society for Neuroscience 26 (50):13007-13016. doi:10.1523/JNEUROSCI.4323-06.2006

34. Adams RH, Alitalo K (2007) Molecular regulation of angiogenesis and lymphangiogenesis. Nature reviews Molecular cell biology 8 (6):464-478. doi:10.1038/nrm2183

35. Zhang ZG, Zhang L, Jiang Q, Chopp M (2002) Bone marrow-derived endothelial progenitor cells participate in cerebral neovascularization after focal cerebral ischemia in the adult mouse. Circulation research 90 (3):284-288

36. Sobrino T, Hurtado O, Moro MA, Rodriguez-Yanez M, Castellanos M, Brea D, Moldes O, Blanco M, Arenillas JF, Leira R, Davalos A, Lizasoain I, Castillo J (2007) The increase of circulating endothelial progenitor cells after acute ischemic stroke is associated with good outcome. Stroke; a journal of cerebral circulation 38 (10):2759-2764. doi:10.1161/STROKEAHA.107.484386

37. Issa R, Krupinski J, Bujny T, Kumar S, Kaluza J, Kumar P (1999) Vascular endothelial growth factor and its receptor, KDR, in human brain tissue after ischemic stroke. Laboratory investigation; a journal of technical methods and pathology 79 (4):417-425

38. Lennmyr F, Ata KA, Funa K, Olsson Y, Terent A (1998) Expression of vascular endothelial growth factor (VEGF) and its receptors (Flt-1 and Flk-1) following permanent and transient occlusion of the middle cerebral artery in the rat. Journal of neuropathology and experimental neurology 57 (9):874-882

39. Krum JM, Mani N, Rosenstein JM (2002) Angiogenic and astroglial responses to vascular endothelial growth factor administration in adult rat brain. Neuroscience 110 (4):589-604

40. Krum JM, Mani N, Rosenstein JM (2008) Roles of the endogenous VEGF receptors flt-1 and flk-1 in astroglial and vascular remodeling after brain injury. Experimental neurology 212 (1):108-117. doi:10.1016/j.expneurol.2008.03.019

Figure legends

Fig. 1 Study design and imaging setup a) Healthy control animals were measured repetitively for the assessment of BLI brain kinetics and the inter- and intra-animal variability of the BLI signal. Sham and MCAO animals were measured before (pre), and 3, 7, 14 days (3d, 7d, 14d) after 30 min MCAO with MRI and BLI. At 7d and 14d post MCAO tissue was collected for WB and IHC. **b)** BL imaging setup: Animals were placed in a prone position on an elevated bar between two 45° mirrors. BLI was evaluated in four different regions of interest: intact lateral view in mirror, intact hemisphere and ischemic hemisphere in top view, ischemic lateral view in mirror. (MCAO: middle cerebral artery occlusion, MRI: magnetic resonance imaging, BL: bioluminescence, BLI: bioluminescence imaging, WB: Western blot, IHC: immunohistochemistry)

Fig. 2 Assessment of brain kinetics and stability of the BLI signal from healthy animals a) Exemplary MRI and BLI images of the three-fold repetition of one healthy animal shows an intact brain and a stable intensity of photon emission over time. **b)** The measurement directly after luciferin injection enabled to reveal the inflow kinetics specifically for the brain. An inflow phase between 1-10 min can be distinguished from a steady state phase of maximal photon emission between 12 and 15 min after injection. Emission from left and right hemisphere was consistently of same magnitude. Data is presented as mean ± standard deviation. **c)** Repeated measurement of each animal revealed intra-individual variability of 3 – 30%. Inter-animal variability of the absolute intensity during the steady state was around 20% to 45%. Data is presented as mean ± standard deviation. Note: Data is presented divergently to other graphs as group mean ± standard deviation for the purpose of descriptive statistics. (PE: photon emission, PE_{15}: photon emission during the 15^{th} minute after luciferin injection representing PE of the steady state phase)

J.M. Adamczak *et al*. Non-invasive VEGFR2 imaging after stroke

Fig. 3 Qualitative and quantitative evaluation of BLI changes after sham and MCAO surgery a) Representative longitudinal MRI and BLI data set from one animal that received MCAO surgery. After MCAO, a clear lesion is visible in the right hemisphere on T2 maps. BLI signal intensity starts to increase 3d post-stroke and PE is clearly increased over the ischemic hemisphere compared to the intact hemisphere at 7d and 14d post-stroke. Increased PE from the ischemic hemisphere is distinctively visualized in the mirrors. **b)** Representative longitudinal MRI and BLI data set from one animal that received sham surgery. Sham surgery did not result in lesion formation confirmed by unchanged T2 maps. However, sham surgery lead to a transient increase in photon emission from the ipsilateral side, which was best visible in the mirror system. **c)** BLI kinetics of the ischemic and the intact hemisphere at 14d post sham surgery (upper graph) and MCAO surgery (lower graph). After sham surgery, both hemispheres exhibit similar inflow behavior. PE from the sham hemisphere is slightly but not significantly increased compared to the intact side. After MCAO, PE increases faster in the ischemic side. The ischemic side as well as the intact side reach a steady state emission starting 12 min after luciferin injection. The absolute PE during the steady state is higher from the ischemic hemisphere. **d)** Quantification of BLI changes was achieved by normalization of PE from ischemic to intact hemisphere for the top view (left graph) and the mirror view (right graph). Pre-stroke PE was consistently equal in all investigated groups with a stronger variation in the mirror view. Increased PE was significantly different to pre-stroke values on day three for stroke, but also for sham animals in both views. At 7d and 14d, elevated PE in stroke animals was statistically significant compared to pre-stroke values (both $p<0.001$) and to the sham group ($p=0.021$, $p=0.044$). For visual comparison, the results of the repetitive measurement of healthy animals are incorporated in the graph, although these were measured at different days than indicated here. (* comparison to pre $p<0.05$; # comparison to sham $p<0.05$)

Fig. 4 Qualitative and quantitative evaluation of tissue VEGFR2 protein content a) Representative Western blots from cortical tissue samples for each group showing increased VEGFR2 (210 and 230 kDa) content in the ischemic cortex of animals that underwent MCAO. Note the strong increase in the 7d group. Sham animals and healthy control display similar levels between left and right hemisphere. **b)** Representative Western blots from striatal

tissue samples. Strongest elevation is visible in the 14d MCAO group. **c)** Semi-quantification (including normalization to actin) and subsequent normalization to the intact hemisphere reveals slightly increased VEGFR2 expression in the cortex of sham animals, while the increase is very pronounced in cortex and striatum in the MCAO group.

Fig. 5 Immunohistochemical analysis of vascular changes a) Immunohistochemistry of laminin for vascular volume estimation. Representative close-ups of 20x magnification for each region of interest already display apparent changes in vessel density. **b)** Quantification and subsequent normalization to the intact hemisphere confirms decreased vascular volume in the core region of the cortex but not in the core region of the striatum. Sham animals showed little changes in corresponding areas of the brain. However, healthy animals displayed strong variability in corresponding regions in the cortex, probably inherent to the methodological approach chosen here. Vascular volume in the peri-infarct zone of the striatum was elevated, but not in the peri-infarct zone of the cortex. Sham animals showed little changes in corresponding areas of the brain. **D)** Z-stacks of three representative BrdU+/lectin+ newly formed endothelial cells from the striatum and the peri-infarct cortex. Scale bar shows 20 μm

Fig. 6 Correlation a) Scatter plot of group-pooled BLI signal change (change of ischemic hemisphere compared to intact hemisphere) against VEGFR2 protein content (WB – Western blot) shows two distinct clusters: Healthy and sham animals show little change and cluster around the 1 intersection, while MCAO animals have increased PE and increased VEGFR2 content in the ischemic hemisphere and cluster in upper right quadrant. **b)** Scatter plot of group-pooled BLI signal change against vessel density change (IHC – immunohistochemistry) shows two distinct clusters: Healthy and sham animals show little change and cluster around the 1 intersection, while MCAO animals have increased PE and increased vessel density in the ischemic hemisphere and cluster in upper right quadrant.

Figure 1

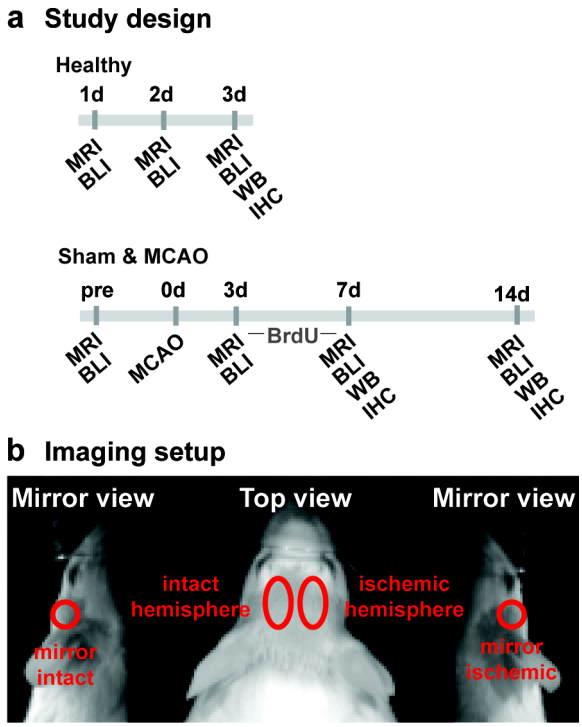

Figure 2

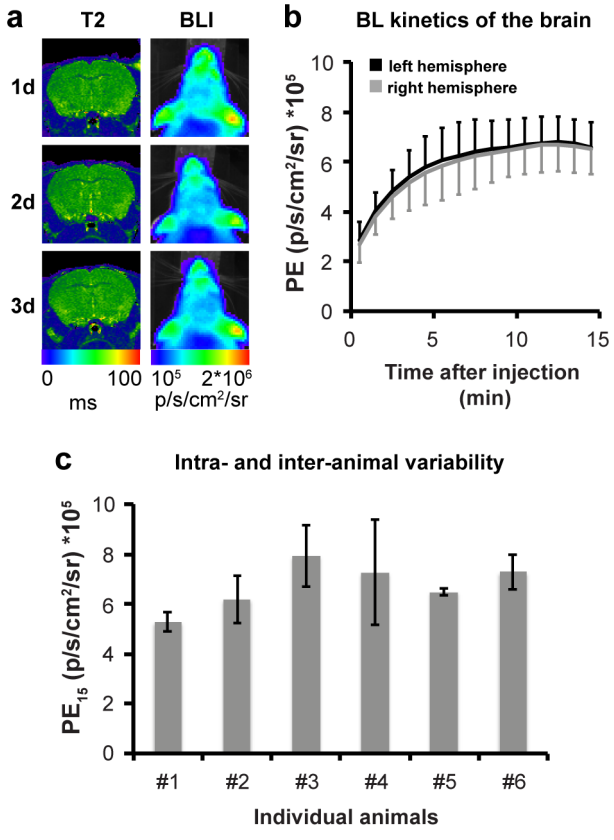

Figure 3

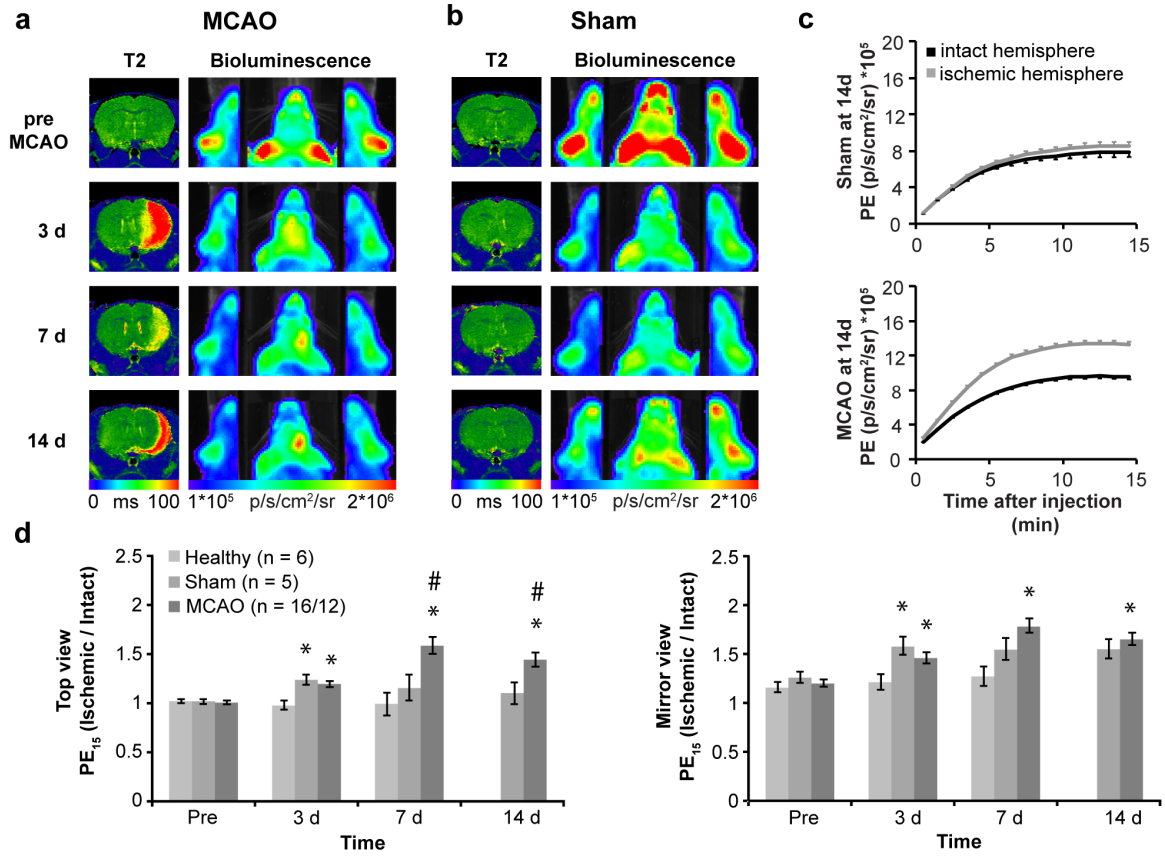

Figure 4

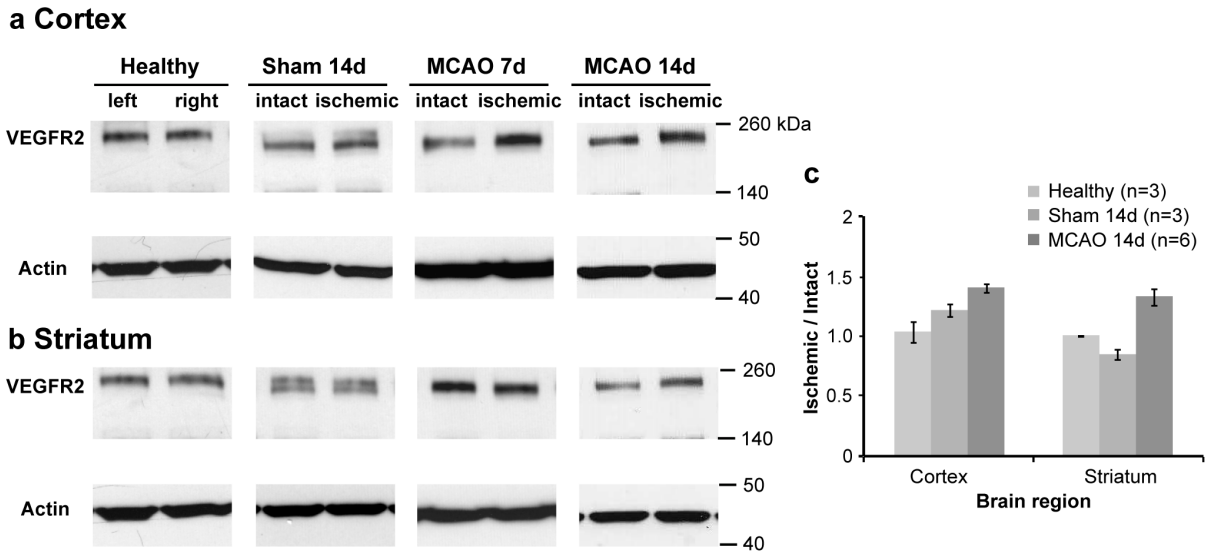

Figure 5

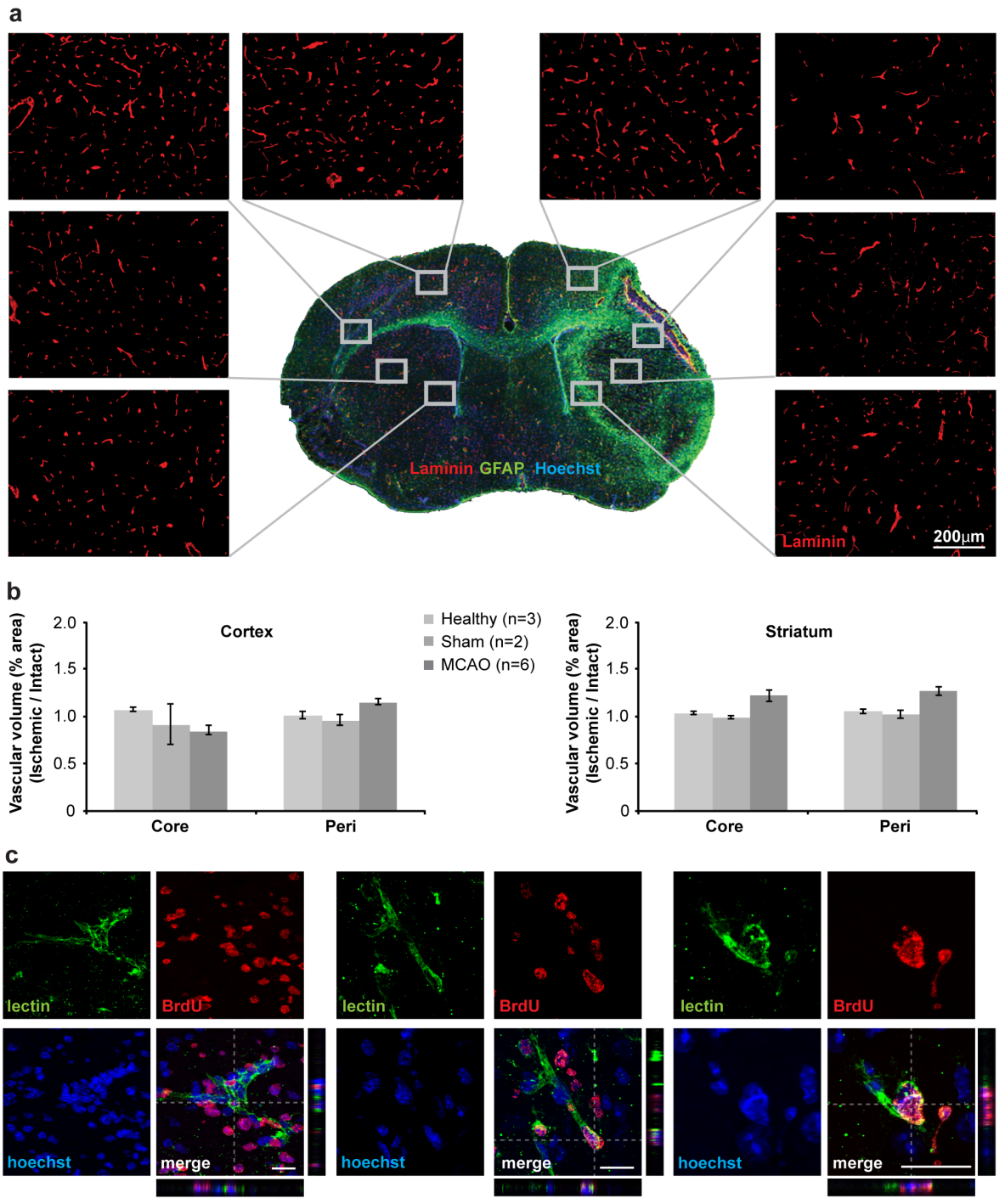
a
Laminin GFAP Hoechst
Laminin
200µm
b
Cortex
Striatum
Healthy (n=3)
Sham (n=2)
MCAO (n=6)
Vascular volume (% area)
(Ischemic / Intact)
2.0
1.5
1.0
0.5
0
Core
Peri
c
lectin
BrdU
hoechst
merge

Figure 7

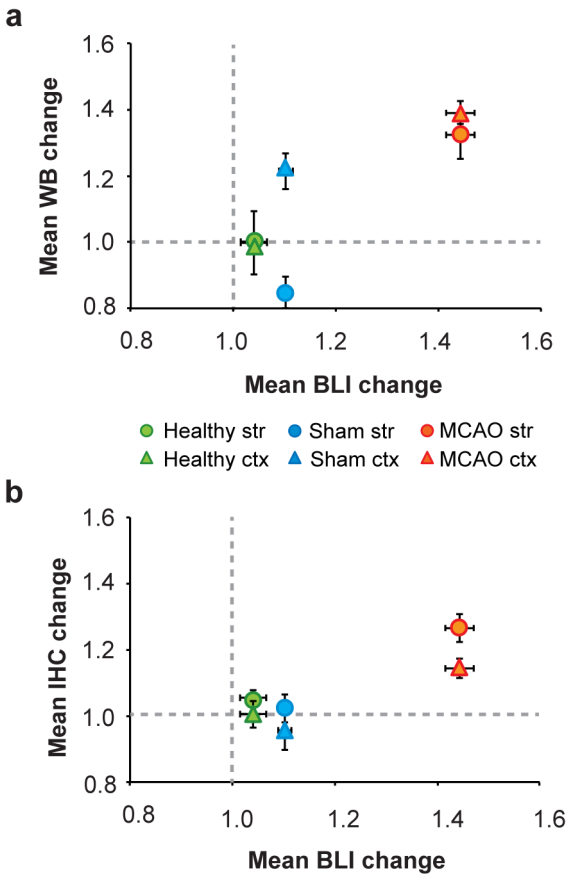
a
Mean WB change
1.6
1.4
1.2
1.0
0.8
0.8
1.0
1.2
1.4
1.6
Mean BLI change
Healthy str
Sham str
MCAO str
Healthy ctx
Sham ctx
MCAO ctx
b
Mean IHC change
1.6
1.4
1.2
1.0
0.8
0.8
1.0
1.2
1.4
1.6
Mean BLI change

II.

Vascular changes after stroke in the rat – a longitudinal study using optimized magnetic resonance imaging.

Philipp Boehm-Sturm*, Tracy D. Farr*, Joanna M. Adamczak, Jan Jikeli, Luam Mengler, Dirk Wiedermann, Therése Kallur, Valerij Kiselev, and Mathias Hoehn
Contrast Media and Molecular Imaging (2013) (accepted)
(*: authors contributed equally)

SPi | Journal Code: C M M I | Article ID: 1 5 3 4 | Dispatch: 12.02.13 | CE: | No. of Pages: 10 | ME:

Full Paper

CONTRAST MEDIA & MOLECULAR IMAGING

Received: 24 August 2012, Revised: 30 November 2012, Accepted: 15 January 2013, Published online in Wiley Online Library: 2013

(wileyonlinelibrary.com) DOI: 10.1002/cmmi.1534

Vascular changes after stroke in the rat: a longitudinal study using optimized magnetic resonance imaging

Philipp Boehm-Sturm[a†], Tracy D. Farr[a†], Joanna Adamczak[a], Jan F. Jikeli[a,b], Luam Mengler[a], Dirk Wiedermann[a], Therése Kallur[a], Valerij Kiselev[c] and Mathias Hoehn[a]*

During stroke, the reduction of blood flow leads to undersupply of oxygen and nutrients and, finally, to cell death, but also to upregulation of pro-angiogenic molecules and vascular remodeling. However, the temporal profile of vascular changes after stroke is still poorly understood. Here, we optimized steady-state contrast-enhanced magnetic resonance imaging (SSCE MRI) and followed the dynamic changes in vascular architecture for up to 4 weeks after transient middle cerebral artery occlusion (MCAO) in rats. Using MRI diffusion measurements and the changes of transversal relaxation rates ΔR_2 and ΔR_2^* after injection of a superparamagnetic contrast agent, SSCE MRI provided several hemodynamic parameters: relative cerebral blood volume (rCBV), rCBV in small vessels, microvascular density, and relative vessel size. Six rats underwent SSCE MRI before MCAO and at 7, 14, 21 and 28 days after surgery. 5-Bromo-2′deoxyuridine (BrdU) was injected between days 2 and 7 to label proliferating cells during this time. SSCE MRI depicted a decrease in microvessel density and an increase in vessel size in the ischemic striatum after stroke. A persistently decreased MRI vessel density was confirmed with histology at 28 days. BrdU+ endothelial cells were found in regions close to the infarct indicating endothelial cell proliferation during the first week after MCAO; however, late-stage angiogenesis, as would be reflected by increased vessel density, was not detected. The optimized SSCE MRI protocol was used to follow spatio-temporal changes of important vessel characteristics, which may contribute to a better understanding of the role of angiogenesis at different stages after stroke.

Supporting information may be found in the online version of this paper

Keywords: steady-state contrast-enhanced MRI; vessel density imaging; vessel size imaging; middle cerebral artery occlusion; angiogenesis

1. INTRODUCTION

Stroke is characterized by a disturbance in blood supply to the brain. Reduction of blood flow results in widespread cell death, but also activation of several molecules and signaling pathways that are thought to promote angiogenesis, reviewed in (1–3). Proliferating endothelial cells were first observed more than a decade ago in human post mortem ischemic tissue (4), and vascular casting in rodent models of middle cerebral artery occlusion (MCAO) illustrated the formation of vascular buds, some of which appeared to anastomose with surrounding vessels (5). However, it is not clear whether or not these new vessels are functional, or whether they have the capacity to play a role in stroke outcome.

Magnetic resonance imaging (MRI) has long been used to observe alterations in cerebral blood supply following stroke. While resolution is currently lacking to detect formation of new microvessels directly, under the assumption that these vessels are functional, MRI can, however, depict cerebral blood volume (CBV) changes, which in turn can be used to noninvasively estimate microvessel density and size, as reviewed in Neeman *et al.* (6) and Seevinck *et al.* (7). Here, the term microvessel usually refers to capillaries (5–10 μm diameter) in contrast to large arteries and veins (~100 μm diameter). Although the vascular tree may more accurately be described by self-similar structures of a wide range of diameters, such simple categorization into small and large vessels is under defined conditions justified in the context of MRI signal from vasculature (8). Steady-state contrast-enhanced magnetic resonance imaging (SSCE MRI) provides measures of blood volume, vessel size, and vessel density by measuring relaxivity changes (ΔR_2 and ΔR_2^*) in

* *Correspondence to: Mathias Hoehn, In-Vivo-NMR Laboratory, Max Planck Institute for Neurological Research, Cologne, Germany. Email: mathias@nf.mpg.de*

† *The first two authors contributed equally.*

a *P. Boehm-Sturm, T. D. Farr, J. Adamczak, J. F. Jikeli, L. Mengler, D. Wiedermann, T. Kallur, M. Hoehn*
In-Vivo-NMR Laboratory, Max Planck Institute for Neurological Research, Cologne, Germany

b *J. F. Jikeli*
Molecular Sensory Systems Laboratory, Center for Advanced European Studies and Research, Bonn, Germany

c *V. Kiselev*
Medical Physics, Department of Diagnostic Radiology, University Hospital Freiburg, Freiburg, Germany

tissue following injection of an intravascular superparamagnetic contrast agent (9–12).

Initial studies applying SSCE MRI in embolic stroke showed that the microvascular density in the lesion core and adjacent tissue decreased (13). However, another study reported an increase in relative cerebral blood volume (rCBV) and density of microvessels in cortical regions starting 14 days after permanent distal MCAO, interpreted as late-stage angiogenesis by those authors (14). Moreover, increased rCBV and vessel size were found in the ischemic territory of rats after MCAO and were interpreted as vasodilation in response to the stroke (15). Further work is required to better understand the optimal acquisition and analysis strategies for SSCE MRI in order to obtain deeper insight into biological processes. In the present study, we carefully refined the technique of SSCE MRI and applied it to the monitoring of vascular changes for up to 4 weeks after transient MCAO in the rat. The results were complemented with an assessment of endothelial cell proliferation during the first week after MCAO by histological means. Our ultimate aim was to elucidate the extent of angiogenesis after cerebral ischemia, which theoretically should be reflected by increased MRI-derived vessel density.

2. MATERIALS AND METHODS

2.1. Animals and experimental design

All animal experiments were conducted according to the guidelines laid out in the German Animal Welfare Act and approved by the authorities (Landesamt für Natur, Umwelt und Verbraucherschutz Nordrhein-Westfalen) under permission number 9.93.2.10.31.07.048 (dated 22 May 2007). Adult male Wistar rats (body weight 300–350 g, Harlan–Winkelmann GmbH, Borchen, Germany) were housed in cages under a 12 h light/12 h dark cycle with access to food and water *ad libitum*. During all surgical and scanning procedures animals were anesthetized and maintained with isoflurane in a 70:30 nitrous oxide–oxygen mixture, and core body temperature was maintained at 36.7 ± 1.0 °C using in-house automated feedback systems and heat blankets (medres GmbH, Cologne, Germany). Animals were scanned with MRI 4–7 days before and on days 7, 14, 21 and 28 after MCAO, and were sacrificed for histology after the last experimental session. Additionally, rats received 5-bromo-2′deoxyuridine (BrdU, 50 mg kg^{-1} twice daily i.p., Sigma-Aldrich, Hamburg, Germany) between days 2 and 7 after MCAO to label proliferating cells.

2.2. Stroke induction

Stroke was induced by occlusion of the middle cerebral artery via intraluminal filament technique (16) with the following modifications. Rats were anesthetized and an incision was made in the right temporal muscle halfway between the eye and ear. The animals were subsequently placed in a supine position and a calibrated 1 mm diameter Laser probe was placed against the right skull to monitor cerebral blood flow changes in the sensorimotor cortex following filament placement with a laser doppler perfusion monitor (Perimed, Järfälla, Sweden). A midline incision was made in the neck, and the mandibular glands, pretrachial strap, and sternomastoid muscles were retracted. The carotid artery and external carotid artery were exposed and ligated with surgical sutures and a microclip was placed on the internal carotid artery. A small incision was made in the carotid artery below the external carotid artery and internal carotid artery bifurcation and a silicone coated monofilament (410 μm diameter, Doccol Corporation, Redlands, CA, USA) was inserted and advanced up the internal carotid artery until resistance was felt and a decrease in cerebral blood flow noted (approximately 17 mm). After 60 min the filament was withdrawn, the suture on the external carotid artery removed, muscles and glands guided back into place, wounds sutured and treated with local anesthetic. Animals received 2.5 ml of physiological saline s.c. daily and were provided with moistened food until weight stabilized. Exclusion criteria stipulated any animals with subarachnoid hemorrhage, incomplete MCAO (no observable T_2 changes during MRI 1 week after MCAO) were removed from the study. Six rats entered the study, four of which had a lesion restricted to the striatum, depicted as hyperintensities on T_2 maps; two animals exhibited cortical and striatal damage. One animal did not perform the SSCE MRI measurement 2 weeks post MCAO.

2.3. SSCE MRI

2.3.1. *Theory*

In order to analytically describe the changes in MRI signal owing to i.v. injection of a paramagnetic substance, the vessel network is modeled as a set of infinitely long, randomly distributed cylinders (17,18). Proton spins are assumed to be restricted to one of two compartments: either within vessels (intravascular) or within the tissue surrounding the vessels (extravascular). Further assumptions include a small blood volume fraction $\xi_0 << 1$ and a diffusion length much smaller than the size of a strongly dephased area around the vessel, that is, $\delta\omega \cdot \rho^2/D >> 1$ (8). D represents the water diffusivity in the extravascular compartment, ρ is the vessel radius, and $\delta\omega$ is the characteristic shift in Larmor frequency of a magnetized cylinder in an external magnetic field.

Under these assumptions, the change in MRI signal from before (S_{pre}) to after (S_{post}) the contrast agent injection can simply be described by shifts of the relaxation rates measured in a spin echo (SE) ($R_2 \rightarrow R_2 + \Delta R_2$) and gradient echo (GE) experiment ($R_2^* \rightarrow R_2^* + \Delta R_2^*$) (cgs units) (11):

$$\Delta R_2 = \frac{1}{TE} \ln\left(\frac{S_{pre,SE}}{S_{post,SE}}\right) \approx 0.694 \cdot \delta\omega^{2/3} D^{1/3} \xi_0 \rho^{-2/3} \quad (1)$$

$$\Delta R_2^* = \frac{1}{TE} \ln\left(\frac{S_{pre,GE}}{S_{post,GE}}\right) \approx \frac{2}{3} \xi_0 \delta\omega \quad (2)$$

Here, TE is the echo time.

In order to assess the important tissue parameters T_2 and ΔR_2 simultaneously, we decided to use a multi spin echo pulse sequence (MSME). This results in an effective reduction of the diffusion effect $D \rightarrow D/n^2$ depending on the number of refocusing pulses n (19,20). ΔR_2 is then determined with the MRI signal S_{MSME} of the nth echo of the MSME via the modified relationship:

$$\Delta R_2 = n^b \frac{1}{TE(n)} \ln\left(\frac{S_{pre,MSME}(n)}{S_{post,MSME}(n)}\right), b = \frac{2}{3} \quad (3)$$

Neglecting the reduced diffusion effect leads to a high underestimation of ΔR_2 values. We found a lower exponent $b = 0.49$ in the experiment (Supporting Information, Fig. S1), which was used for all further analysis. The deviation from the theory will be subject to further studies.

Equations (1) and (2) show that ΔR_2 is a measure of rCBV in small vessels whereas ΔR_2^* reflects the rCBV in all vessels. However, both still depend on the concentration C of the contrast agent in blood, which usually needs to be assessed invasively or with dynamic contrast-enhanced measurements (11). Therefore, Jensen and Chandra introduced the so-called Q -factor, which is largely independent of C and is a measure of microvessel density (10).

$$Q = \frac{\Delta R_2}{(\Delta R_2^*)^{2/3}} \tag{4}$$

Q relates to the number of vessels that punctuate a cross-section of tissue per unit area. Microvessel density N is counted in units of $[N] = 1\ \mathrm{mm}^{-2}$ and can be calculated when the presence of large macrovessels can be neglected and taking into account the water diffusivity in tissue (12):

$$N = 0.218\left(Q^3/D\right), [D] = \mathrm{mm}^2 s^{-1}, [Q] = s^{-1/3} \tag{5}$$

Furthermore it can be shown that the mean vessel size holds true (11):

$$\rho = 0.425\left(\frac{1}{\gamma \Delta\chi B_0}\right)^{1/2} \cdot (D)^{1/2} \left(\frac{\Delta R_2^*}{\Delta R_2}\right)^{3/2} \tag{6}$$

Owing to the lack of *in vivo* measurements of the contrast agent concentration and thus lack of $\Delta\chi$ values, we neglected the first term in eqn (6) and used a relative vessel size R (in arbitrary units) throughout the article, which is defined as:

$$R = \left(\frac{D}{D_{lit}}\right)^{1/2} \left(\frac{\Delta R_2^*}{\Delta R_2}\right)^{3/2}. \tag{7}$$

Here, we accounted for local changes in diffusivity in the pathologic brain by multiplication with the square root of the quotient of measured diffusivity D and a known value for the healthy brain $D_{lit} = 6.64 \times 10^{-4}\ \mathrm{mm}^2\ \mathrm{s}^{-1}$ (21).

2.3.2. *MRI acquisition*

MRI was carried out on a 4.7 T animal scanner (Biospec47/30, Bruker BioSpin, Ettlingen, Germany) equipped with actively shielded gradient coils (BGA 12, 220 mT m^{-1}, 120 µs rise time, Bruker BioSpin). We used a custom-built surface radiofrequency coil 30 mm in diameter for reception and a Helmholtz coil for homogeneous transmission (medres GmbH, Cologne, Germany). Animals were fixed with tooth bar and ear bars in a custom-made animal holder (medres). Respiration rate was monitored with a pressure-sensitive pad under the thorax using DASYlab (Measurement Computing, Norton, USA) software.

The imaging protocol consisted of apparent diffusion coefficient (ADC) measurement [spin echo MRI, field of view = (2.56 cm)^2, eight contiguous 1 mm thick slices, matrix = 128^2, echo time/repetition time (TE/TR) = 40.66 ms/4 s, one diffusion direction medial-lateral in the animal coordinate system, $b_{\mathrm{eff}} = 0.26$, 600.26, and 1500.26 s mm^{-2}, TA = 12:48 min], an MSME (TE/TR = 13.55 ms/4 s, 10 echoes, TA = 8:32 min) and a multigradient echo pulse sequence (MGE, TE/TR = 5 ms/2 s, eight equidistant echoes, flip angle = 60°, TA = 8:32 min). The geometries of the MSME and MGE were matched to the ADC measurement to allow voxel-wise calculation of vessel density, except that four additional slices were acquired in order to cover the whole forebrain in the T_2 and T_2^* images.

After initial measurements, superparamagnetic iron oxide particles (Endorem, Guerbet, Sulzbach, Germany, 11.2 mg Fe ml^{-1}) were injected in the tail vein at a dose of 30 mg Fe kg^{-1} without moving the animal. We allowed the contrast agent to distribute homogeneously over the blood pool for 3 min, and then identical post-contrast MSME and MGE images were acquired.

2.4. MRI data processing

The MRI data were processed with Interactive Data Language (IDL, ITT visual information solutions, Boulder, CO, USA) and FMRIB Software Library (FSL, http://www.fmrib.ox.ac.uk/fsl).

For T_2 maps, the MRI signal $S(TE)$ in MSME scans was fitted on a voxel-wise basis with a monoexponential decay $S(TE) = A \exp(-TE/T_2) + B$ with equilibrium signal A, relaxation time T_2, and an offset B to reduce bias introduced by the use of magnitude images (22). Accordingly, ADC maps were generated by fitting the MRI signal with $S(b) = A \exp(-b \cdot ADC) + B$. Maps were co-registered to a template rat brain (an average of 34 high-resolution T_2 -weighted images from 28 rats, scaled to match the resolution of our scans) with FSL's linear registration tool.

For vessel size and density maps, the A_0 images ($b = 0.26\ \mathrm{s\ mm}^{-2}$) of the ADC scan and the first echo images of the pre- and post-contrast MSME and MGE scans were segmented with FSL's brain extraction tool. The segmented images were co-registered to the template brain with an affine transformation (12 degrees of freedom) with FSL. The determined transformation matrices were applied to the other ADC images, and the later echoes of the MSME and MGE datasets. Finally, the co-registered images were used for voxel-wise calculation of ΔR_2^*, ΔR_2, Q, N and R according to equations (2)–(5) and (7), respectively. ΔR_2 and ΔR_2^* were calculated from the second echo of the MSME and MGE images, respectively, in order to minimize error propagation in the data analysis scheme (Supporting Information, Fig. S2). Voxels with a signal to noise ratio < 5 in either the A_0 image of ADC measurements or in the first echo of the MSME or MGE were excluded from the analysis. Voxels with negative ΔR_2 or ΔR_2^* values, or those with $\Delta R_2 > \Delta R_2^*$ were also excluded.

Volume-of-interest (VOI) analysis was carried out with the freeware program ImageJ (http://rsbweb.nih.gov/ ij/). First, for anatomically selected VOIs, the intact and ischemic striatum was manually delineated in the coronal slices corresponding to −0.3 and −1.3 mm from bregma. Second, lesion-based VOIs were manually drawn in the same two slices for each animal on T_2 maps acquired 1 week post MCAO. The lesion-based VOIs encompassed voxels with increased T_2 values ($T_2 >$ mean + 2 standard deviations of contralateral striatum). Third, a VOI of the peri-infarct zone was drawn by extension of the lesion VOI by 0.4 mm in-plane (neglecting ventricles and areas outside the brain) and by subsequent subtraction of the lesion VOI. Mirroring of the lesion and peri-infarct VOIs at the midline with a custom ImageJ macro yielded the contralateral VOIs. Mean ΔR_2^*, ΔR_2, Q, N and R values were recorded and presented as a ratio of the ischemic to intact side.

The incidence maps were generated by normalization (voxel-wise division) of the post-MCAO parameter maps to the time point

before surgery. An incidence in a voxel at a certain time point was counted when that voxel showed a significant increase/decrease, that is, with a normalized parameter of interest larger/smaller than the mean ± 2 standard deviations when compared with the contralateral striatum. For each SSCE MRI parameter increase/decrease, incidences of all animals were added voxel-wise. The resulting incidence map for the group of animals was smoothed (Gauss filtered, sigma = 0.2 mm) and overlaid on the template brain.

2.5. Immunohistochemistry

After the last MRI session, animals were deeply anesthetized and perfused transcardially with cooled saline followed by cooled 4% paraformaldehyde. Brains were post-fixed overnight and cryo-protected in 30% sucrose solution prior to coronal sectioning at 40 μm on a freezing microtome (Leica Microsystems, Wetzlar, Germany). Sections were kept at −20 °C in cryo-protective solution. For double-label immunofluorescence with BrdU, free-floating sections were denatured in 1 mol l^{-1} HCl for 10 min at 65 °C, followed by 20 min incubation at room temperature and pre-incubation in appropriate blocking solution: 5% normal sera and 0.25% Triton X-100 in potassium phosphate-buffered saline for 60 min at room temperature. Incubation with primary antisera was carried out overnight at +4 °C and the following primary antibodies were used: rat anti-BrdU (1:100, Abcam, Cambridge, MA, USA), and mouse anti-Rat Endothelial Cell Antigen (RECA; 1:400, AdB Serotec, Oxford, UK). Primary antibodies were detected using either standard diaminobenzidine (DAB) immunohistochemistry or appropriate fluorescent Cy3 (Jackson ImmunoResearch, West Grove, PA, USA) or biotin-conjugated (Vector Laboratories, Burlingame, CA, USA) secondary antibodies (1:200), the latter of which was detected with Alexa 488-conjugated streptavidin (1:200, Invitrogen, Carlsbad, CA, USA). Sections were mounted on poly L-lysine coated slides (Thermo Fisher Scientific, Waltham, MA, USA) and coverslipped with glycerol-based mounting medium.

Microscopic images were acquired and double-immunoreactivity verified with a confocal laser scanning microscope (Leica TCS SP5 X, Leica Microsystems). Microvessel density was semi-quantified across the entire intact and ischemic striatum from RECA DAB stained sections located approximately −0.3 mm from bregma (corresponding to the anterior commissure) (23) using the Stereo Investigator system (MicroBrightField Europe, E.K., Magdeburg, Germany) with a counting frame of 40 μm^2 at 20× magnification. Microvessel size was estimated by measuring the diameter at the thickest point of a counted vessel every 100 frames.

2.6. Statistical analysis

Data are expressed as group means ± standard deviation of the means. Statistical analysis was performed using SPSS version 17 software and a p-value < 0.05 was used as the significance level. VOI values in the striatum/lesion/peri-infarct zone were compared using one way repeated measures analysis of variance with time as the within-subject factor followed by *post-hoc* pairwise comparisons with the least significant difference test. For comparison of histology and MRI, microvessel densities in the intact and ischemic striatum were analyzed using paired Student's t-tests.

3. RESULTS

3.1. Impact of noise and echo times on SSCE MRI results

To determine the impact of noise on the most noise-sensitive parameter N, we performed simulation experiments in which white noise was added to artificial MRI datasets. In parallel we analyzed histograms in experimental MRI datasets from animals before MCAO. Our simulations also determined that suboptimal echo times result in non-Gaussian, widespread distribution of the resulting N values (Supporting Information, Fig. S2). From this, we anticipated that, in order to detect physiologically relevant changes in N (as a marker of microvessel density), the relative change must be in the order of magnitude of 20%.

3.2. Impact of tissue water diffusivity on interpretation of SSCE MRI results

In the chronic phase after MCAO, necrosis, phagocytosis and associated cystic formation in tissue are visualized by a steep increase in ADC values. In all animals with this cyst formation ($n = 3$) regions of elevated ΔR_2 were observed within or close to the lesion core (Fig. 1a). According to the theory, increases in ΔR_2 indicate an increase of rCBV in small vessels, but as is demonstrated by eqn (1), diffusivity also plays a role. Comparison of vessel density maps calculated under inclusion of a constant diffusion value from the literature (21) (Fig. 1b) with those vessel density maps for which the local diffusivity was taken into account on an experimentally recorded, voxel-wise basis (Fig. 1c, d), revealed that the dominant effect leading to the increased ΔR_2 was highly elevated water diffusivity in necrotic tissue. Vessel staining on histological sections confirmed that tissue in these regions was not intact at 4 weeks after MCAO and that the density of small vessels in adjacent regions was not higher compared with healthy tissue (Fig. 1e, f). F1

3.3. Vascular changes after stroke

3.3.1. *MRI Incidence maps*

Incidence maps revealed that decreases in ΔR_2 and Q and an increase in R were most frequent (Fig. 2, bottom three rows). All six animals were used for map calculations but the highest number of incidences found in all pixels for any of the SSCE MRI parameters was three, indicating a regionally and temporally variable pattern of vascular changes across the different animals. Other incidence maps did not show a specific trend. F2

3.3.2. *MRI VOI analysis*

Parameter maps from all animals are presented for all time points in Fig. 3. In all maps except T_2 and ADC we observed global image intensity fluctuations between animals and time points within the whole brain that followed no defined pattern and probably reflected differences in contrast agent concentration within the blood, which was not measured in this study. To account for this, quantitative analysis was carried out in the striatum (Fig. 4a), within the lesion (Fig. 4b) and within the peri-infarct areas (Fig. 4c), and values expressed as a percentage ratio of the ipsilateral (lesioned) to the contralateral (intact) hemisphere. Only a negligible number of voxels (<0.5 ‰) were excluded from the analysis owing to the imposed thresholds on signal to noise, ΔR_2 and ΔR_2^*. F3 F4

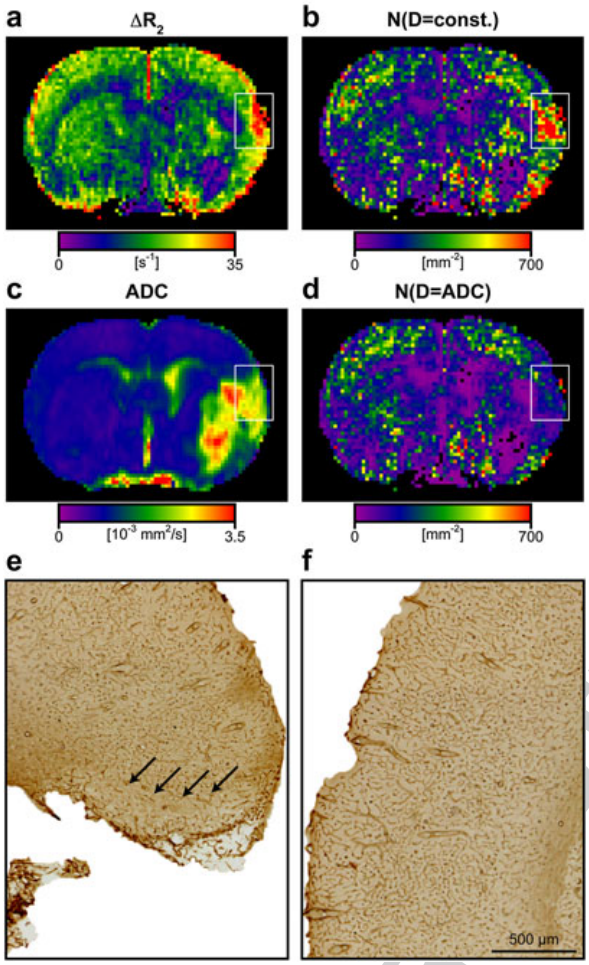

Figure 1. Impact of tissue diffusivity on MRI-derived blood volume and vessel density. All animals with cyst formation exhibited regions with highly elevated ΔR_2 close to or within the lesion core, which is usually interpreted as high rCBV in small vessels. Such an area is indicated by the box on the ΔR_2 map from a representative animal 4 weeks after MCAO (a). Assuming a constant diffusivity value for each voxel that is comparable to healthy tissue leads to high MRI-derived vessel densities (box in b). However, ADC values in this region were also elevated, which indicates necrosis and liquefaction of tissue (box in c). When we took local tissue diffusivity into account on a voxel-wise basis, the 'hot spots' in the MRI-derived vessel densities disappeared (box in d). Histology in the same region confirmed tissue necrosis (e) and a decrease in microvessel density (e, arrows) compared with the same region on the contralateral side (f). Thus, the high ΔR_2 was a result of high tissue diffusivity and not an indicator of increased rCBV in small vessels.

As expected, prior to MCAO the calculated MRI parameters were comparable between the ipsilateral and contralateral side: rCBV in small vessels ΔR_2 (striatum, 101.8 ± 1.3%; lesion, 101.6 ± 2.0%; peri-infarct, 98.5 ± 2.6%), rCBV ΔR_2^* (striatum, 100.5 ± 4.5%; lesion, 103.9 ± 8.2%; peri-infarct, 98.1 ± 4.3%), microvascular density index Q (striatum, 101.3 ± 3.3%; lesion, 99.1 ± 4.1%; peri-infarct, 99.7 ± 2.8%), vessel density N (striatum, 103.8 ± 9.0%; lesion, 98.3 ± 17.3%; peri-infarct, 97.3 ± 6.3%), and relative vessel size R (striatum, 97.1 ± 6.2%; lesion, 102.3 ± 11.4%; peri-infarct, 99.0 ± 9.3%) (Fig. 4). After stroke, the overall rCBV ΔR_2^* remained relatively constant over the course of the experiments. There was a significant effect of time in rCBV in small vessels ΔR_2 [striatum, $F(4,16)$ 3.890, $p = 0.022$; lesion, $F(4,16)$ 6.082, $p = 0.004$; peri-infarct, $F(4,16)$ 5.040, $p = 0.008$]. The percentage ratio of ΔR_2 decreased around 1 week after stroke with a trend towards subsequent increase by week 2, which was confirmed by *post-hoc* pairwise comparisons of values within the lesion before and 1 week post stroke ($p = 0.05$; Fig. 4b).

Significant effects of time were also observed for the microvascular density index Q [striatum, $F(4,16)$ 3.342, $p = 0.036$; lesion, $F(4,16)$ 6.861, $p = 0.002$; peri-infarct, $F(4,16)$ 3.339, $p = 0.036$], microvessel density N [striatum, $F(4,16)$ 3.586, $p = 0.029$; lesion, $F(4,16)$ 6.311, $p = 0.003$; peri-infarct, not significant], and relative vessel size R [striatum, $F(4,16)$ 3.259, $p = 0.039$; lesion, $F(4,16)$ 4.727, $p = 0.01$; peri-infarct, not significant]. In line with the decrease in rCBV in small vessels, Q and N ratios both decreased around 1 week after stroke, although *post-hoc* tests failed to reach significance. The decreases in N and Q at week 1 were accompanied by a dramatic increase in relative vessel size R. This persisted throughout the course of the experiments, although less pronounced for later times.

3.4. Immunohistochemistry

RECA staining clearly detected blood vessels in the brain sections 4 weeks after surgery. Photomicrographs from two representative animals indicate fewer visible vessels in the ischemic striatum (Fig. 5a and b). Histological microvessel density in the ischemic striatum was significantly lower than that of the intact striatum (585 ± 89 vs 827 ± 58 vessels mm^{-2}) [$t(5) = 4.679$, $p = 0.005$]. This corresponded roughly to a ~29% decrease (Fig. 5c, right), which is within the detectability limits determined from our simulations. A similar, significant decrease of ~27% [$t(5) = 2.705$, $p = 0.043$] was observed in MRI-derived vessel density N from the VOI analysis at 4 weeks after MCAO, that is, (209 ± 81) mm^{-2} ipsilateral and (289 ± 75) mm^{-2} contralateral (Fig. 5c, left). The mean vessel diameter, and thus size, measured from brain sections in small vessels (<40 μm) were not significantly different between the ischemic (7.4 ± 1.0 μm) and the intact striatum (7.0 ± 1.0 μm; Fig. 5d, right). However, there was a ~50% increase in R in the ischemic striatum determined from the MRI VOI analysis, although this failed to reach significance [$t(5) = -2.037$, $p = 0.097$; Fig. 5d, left].

We systematically examined sections double-stained for BrdU and RECA. No double-labeled cells were observed in the hemisphere contralateral to the infarct, and green autofluorescence within the ischemic core did not permit analysis there. However, in peri-infarct regions we found occasional individual endothelial cells that also appeared to be BrdU + (Fig. 6). Overall, very few proliferating endothelial cells were detected.

4. DISCUSSION

The present study demonstrates that the temporal profile of vascular changes after stroke can be assessed noninvasively with SSCE MRI. However, our data indicate that it is crucial to optimize MRI acquisition in order to maximize sensitivity of the method. For the first time, we show that when cystic transformation occurs, inclusion of diffusion measurements on a voxel-wise basis is essential to prevent overestimation of SSCE MRI-derived

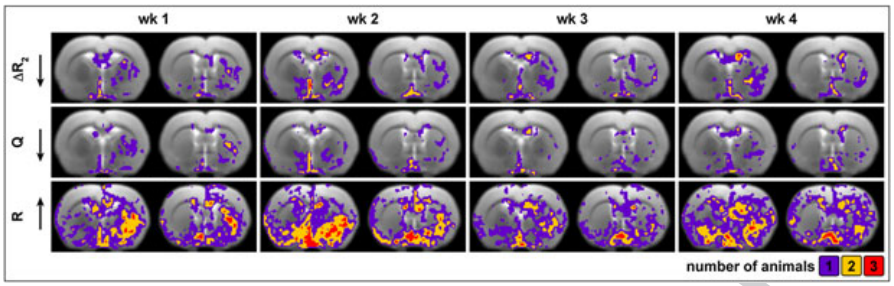

Figure 2. Incidence maps for the MRI-derived parameters. Maps indicating, for each voxel, the number of animals that exhibited a decrease in ΔR_2 or Q, or an increase in R during the 4 weeks after MCAO. For each time point the two coronal slices shown are those that are most affected by the infarct: −1.3 (left) and −0.3 mm from bregma (right). A small trend towards the decrease of ΔR_2 and Q can be observed in the ischemic hemisphere, as well as an increase in R (bottom row) mostly in areas of the striatum. The striatum was therefore used for further quantitative volume-of-interest analysis. Other incidence maps did not show a specific trend. Although six animals entered the calculations, the maximum number of incidences found in any of the parameters was three, that is, within any region, a significant, simultaneous vascular change occurred only in a subgroup of animals.

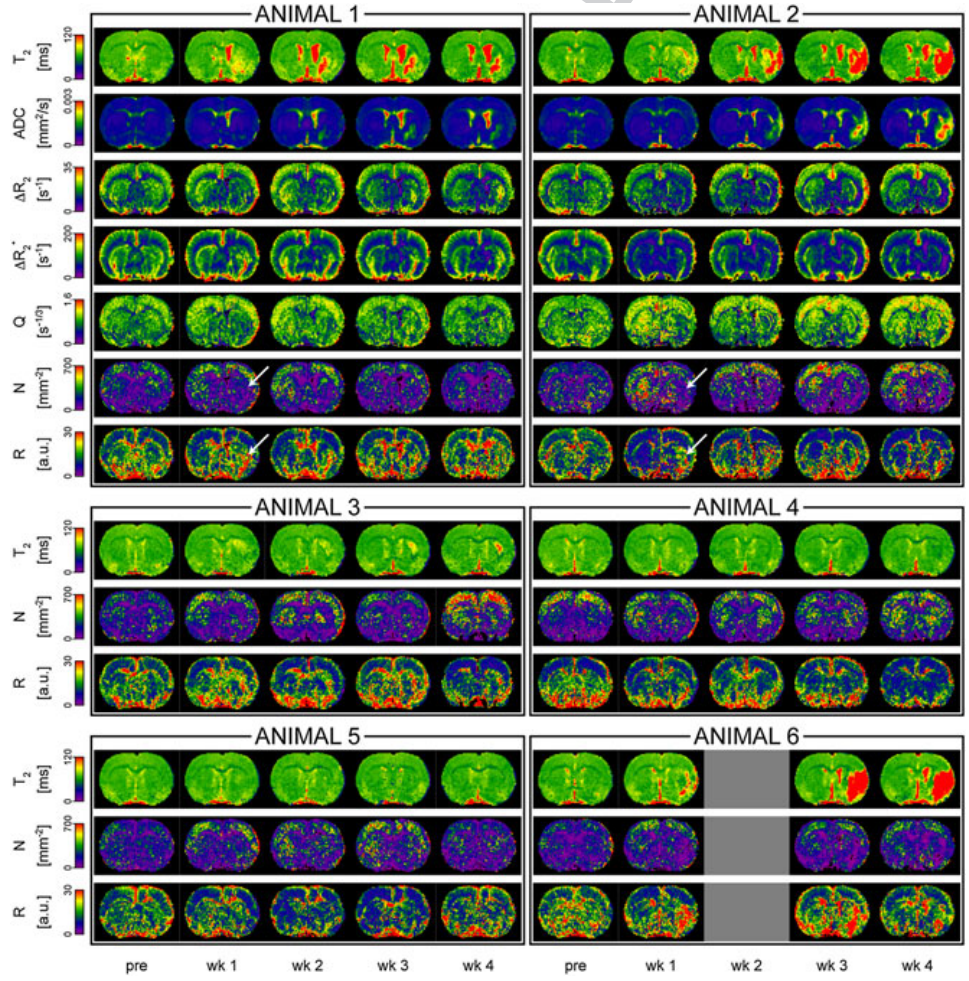

Figure 3. Temporal profile of MRI-derived parameters. T_2, ADC, ΔR_2, ΔR_2^*, Q, N and R maps before and weekly after MCAO of an animal with a lesion restricted to the striatum (animal 1) and an animal with both, cortical and striatal damage (animal 2). Most relevant maps (T_2, N and R) are shown for all other animals. ΔR_2, Q and N decreased in the ischemic regions in all animals whereas there was an observable increase in relative vessel size R. The changes were most pronounced 1 week after surgery (arrows) but persisted also at the later time points. Animal 6 did not perform the SSCE MRI measurement at 2 weeks post stroke.

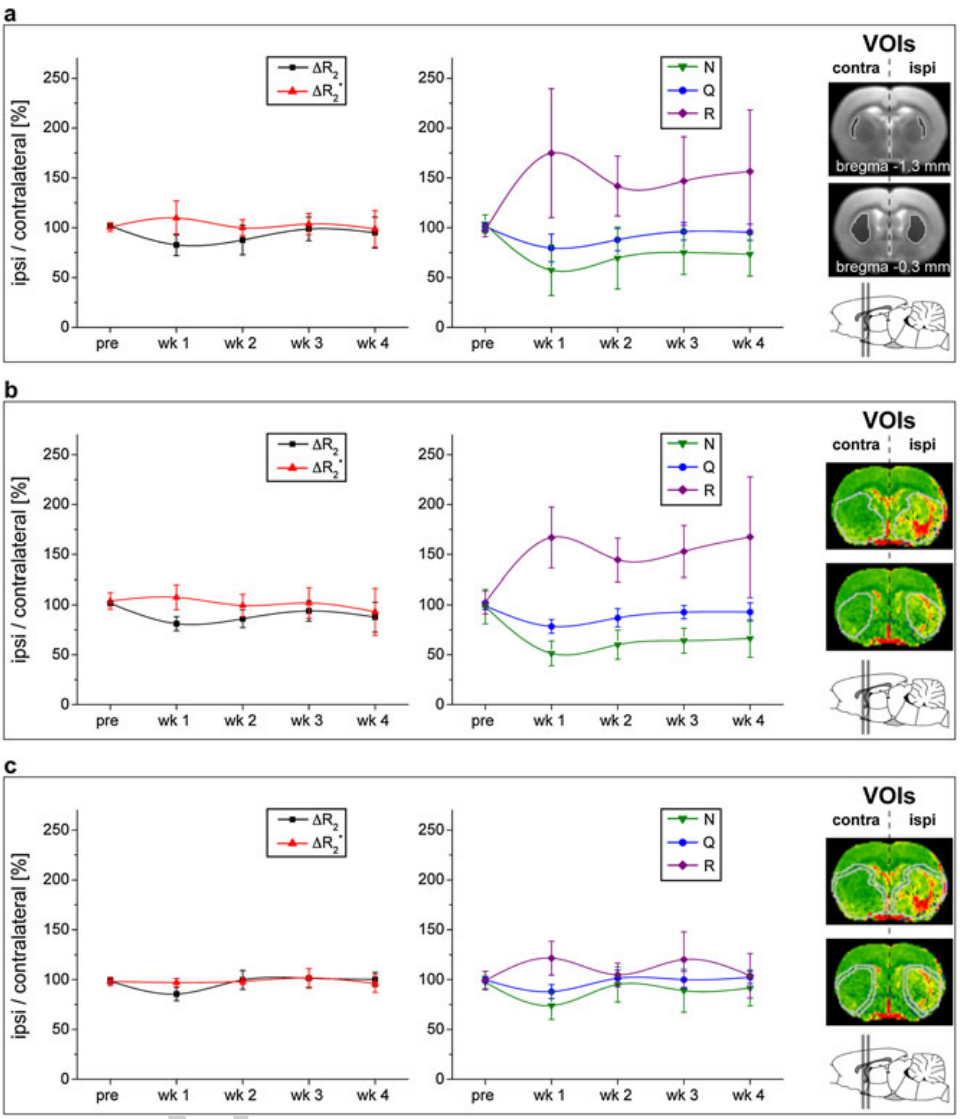

Figure 4. Quantification of MRI-derived parameters. Volume-of-interest analysis in the striatum (a), in the lesion (b), and peri-infarct zone (c) revealed a decrease in ΔR_2, *Q* and *N* and an increase in *R* in the ischemic striatum that was most pronounced 1 week after MCAO. These parameters normalized at the later time points (weeks 2–4). Values are expressed as a ratio of the ipsilateral to the contralateral side (group means ± standard deviation). The volumes of interest are indicated on coronal slices corresponding to −1.3 and −0.3 mm from bregma on a T_2-weighted template image (a) and a T_2-map (b, c) of animal 2. The two slices are illustrated in gray on a schematic sagittal view of the rat brain.

vessel densities. Our major finding was that there was a significant decrease in rCBV in small vessels, leading to a decrease in vessel density, which was accompanied by an increase in vessel size 1 week after MCAO in the ischemic striatum that persisted for several weeks. Microvessel density determination from histological brain sections confirmed that decreased vessel density was still present at 4 weeks after the initial insult. If large-scale angiogenesis occurred in response to stroke, this should have been reflected by an increase in vessel density. This was not the case, although the presence of sparse numbers of BrdU+/RECA + cells in the ischemic striatum indicated that some endothelial cell proliferation occurred during the first week after MCAO. Absence of double-labeled cells on the contralateral hemisphere indicated that the proliferation was induced by the stroke and not by natural turnover of endothelial cells.

4.1. SSCE MRI methodological considerations

When this method was first employed in a rodent model of stroke to measure changes in the vascular network (rCBV in small vessels, overall rCBV, vessel density and size) ΔR_2 was assessed with a turbo spin echo pulse sequence using multiple refocusing pulses to speed up the acquisition (14). Subsequent studies employed multi spin echo sequences in order to obtain measures of T_2 and ΔR_2 simultaneously and further included ADC measurements (13,24). This strategy is useful as both T_2 and ADC provide important

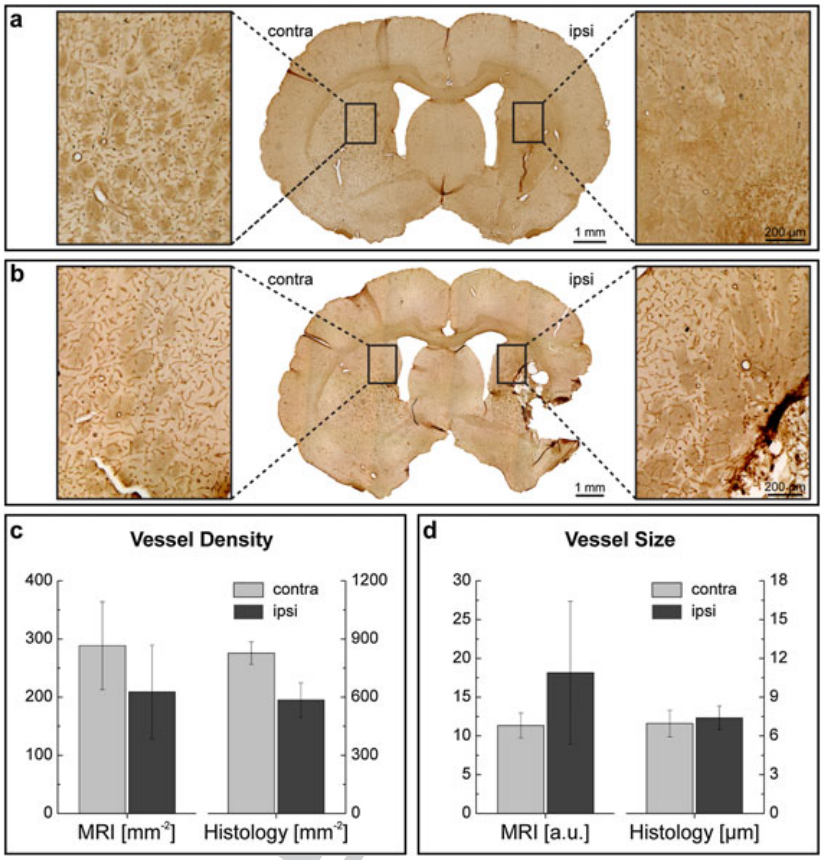

Figure 5. Comparison of MRI and histology. Tissue sections stained for vessels (RECA) of an animal with a small striatal lesion (a) and of a rat with a larger infarct (b). Semi-quantification on histological sections revealed a significant ipsilateral decrease in microvessel density (c, right) that corresponded well with the MRI results at 4 weeks after MCAO (c, left). Histological vessel diameter (of vessels <40 µm) showed only a small, nonsignificant increase in the ipsilateral striatum (d, right), whereas a highly elevated relative vessel size was found in the MRI analysis (d, left), although this failed to reach significance. For better visualization, MRI and histology data are scaled differently. Values are expressed as group means $\pm$ standard deviation.

information about the state of the ischemic tissue. However, neither of these studies performed any modification to the theory in order to account for the well-known reduction of the diffusion effect on MR transverse relaxation (19,20,25). Using the theory modification, however, leads to higher ΔR_2, Q and N values. In line with this, we found higher values of these parameters compared with the reports in which a theory correction was not applied. Furthermore, we also identified a major pitfall in the interpretation of SSCE MRI parameters when the tissue exhibits cystic transformation. In such cases, ΔR_2 is no longer a good measure of rCBV in small vessels, and neither is Q because of elevated tissue diffusivity. Our data indicate that it is essential to include local ADC values in the calculations, otherwise ΔR_2 'hot spots' may be misinterpreted as angiogenic activity.

Despite these improvements in MRI acquisition, our results show that SSCE MRI is prone to noise, especially for the vessel density estimate N. Even after optimization of acquisition parameters, the relative error in N values is on the order of ~20%. Although this is in accordance with the previous reports (13), it represents an inherent limitation of the technique. Further limitations come from the fact that the ischemic rodent brain probably violates some of the previously described assumptions that are made when applying the theory. For example, the mathematical model underlying SSCE MRI only holds for impermeable vessel walls, low blood volume fractions, and vasculature for which the microvessels can be modeled as rigid long cylinders (26). Therefore, the use of blood as an intravascular tracer through the blood oxygen level-dependent contrast seems to be an appealing alternative, e.g. to overcome problems of contrast agent leakage and heterogenous water diffusivity in peri-infarct area. Indeed, quantitative blood oxygen level-dependent approaches have been developed in order to map important parameters of oxygenation *in vivo* (27,28). Furthermore, the use of fast MR imaging during the first bolus (dynamic susceptibility MRI) or arterial spin labeling techniques could help to correlate SSCE MRI with perfusion and thus functionality of blood vessels.

4.2. Vascular changes after stroke

Using SSCE MRI we observed a decrease in microvessel density in the ischemic striatum at 1 week after stroke, a situation not surprising as this tissue has experienced widespread cell death by this time. Similar findings were reported as early as 1 day after ischemia in an embolic (13) and distal occlusion model (14). This decrease in microvessel density persisted for up to 2 weeks in the former study, which is also consistent with our results.

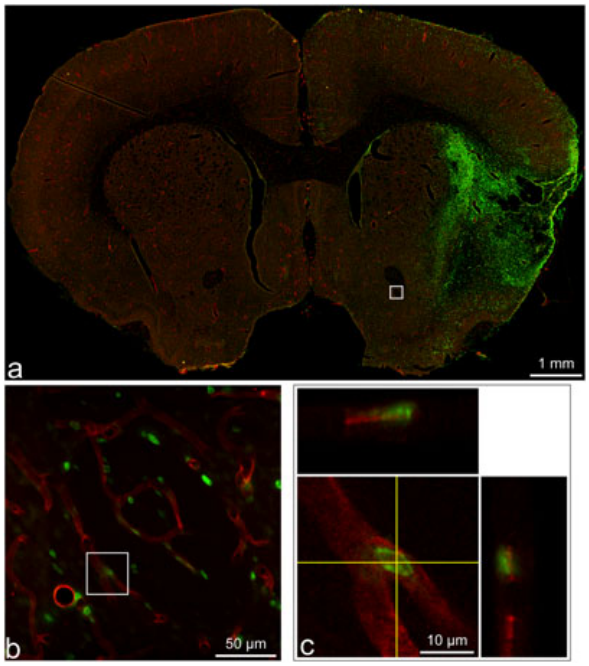

Figure 6. Confocal microscopy images of tissue sections stained for RECA (red) and BrdU (green) 4 weeks after MCAO. BrdU was administered between days 2–7 after MCAO. Overview (a) and higher magnification images (b, corresponds to the white box in a) revealed some red/green overlap and a confocal microscopy image (c, corresponds to the white box in b) confirmed this. Strong green ipsilateral staining in the lesion core (a) is due to ischemia-induced autofluorescence.

Despite the notion that the decrease in microvessel density observed in the ischemic region after stroke is persistent, the SSCE MRI study that employed the distal occlusion model noted a significant increase in microvessel density in the outer cortex of the ischemic region beginning after about 2 weeks that was attributed to angiogenesis (14). One potential reason for this discrepancy could be the choice of stroke model. However, our findings suggest that this effect could be artifactual in nature as we were able to observe a similar phenomenon in animals with cystic transformation when we employed, rather than the correct and necessary voxel-wise diffusion measurement, only a constant diffusion value to determine *N* maps. Indeed and in line with this, the authors of that study mentioned that this area of increased microvessel density was prone to cystic transformation.

In parallel to the decrease in microvessel density, we observed an increase in vessel size with SSCE MRI most pronounced at 7 days post stroke that was probably due to vasodilation of arterioles in an effort to maintain autoregulation. This phenomenon probably occurs earlier, and, indeed, Lin et al. (14) reported this observation within the first week of stroke (1–3 days), which was confirmed by an increase in the number of vessels with a diameter greater than 30 μm in tissue sections from the same time period. While that study reported a subsequent decline in vessel size, other groups suggested that this effect remains between days 7 and 21 (15) and even up to 6 weeks in the recovery region (24). In the present study, we only measured animals up to 28 days, and while *R* was still elevated at this time, this elevation was not as pronounced as during the first week. In accordance with these findings, we were also unable to observe an increase in the mean vessel diameter in the ipsilateral when compared with the contralateral striatum at 4 weeks post stroke. While it is possible that this could be an artifact of our sampling strategy, microvessel is a gross term that includes capillaries, venules and arterioles, which means that the size of vessels varies considerably even in the intact brain (29). Nevertheless, the mean vessel size estimated subcortically at 6 h post symptom onset was recently shown to be a good predictor of final infarct size at 6 days in a small cohort of patients that underwent a modified dynamic contrast-enhanced protocol similar to SSCE MRI (30). A follow-up study extended the same protocol to a larger patient cohort that presented a significant perfusion-diffusion mismatch around 24 h post symptom onset (31). Vessel size was found to be a poor predictor of infarct growth at 6 days, but microvessel density proved to be useful at discriminating infarcted from oligemic or healthy tissue. These studies highlight the utility of this technique to provide valuable information in the post-ischemic period.

4.3. Angiogenesis after stroke

Angiogenesis after ischemia is generally characterized at a cellular level by gene transcription leading to expression of pro-angiogenic molecules and finally to endothelial cell proliferation. We observed some endothelial cell proliferation during the first post-operative week, which is already well described (5), and another study observed increases in various pro-angiogenic compounds such as growth factors and endothelial nitric oxide synthase (14). While stabilization of vessel walls and formation of new networks have been reported (5), it is unclear if these processes can lead to truly functional new vasculature (7). Perfusion measurements could help to elucidate if proliferating, BrdU + endothelium belongs to functional vasculature. Unfortunately, as SSCE MRI is based on CBV measurements using an intravascular contrast agent, it is only capable of detecting perfused vessels. The evidence from the preclinical SSCE-MRI studies in stroke models consistently indicates that there is an overall decrease in microvessel density rather than a large-scale increase. The small number of animals in the present study renders general conclusions difficult. However, taken together, this implies that angiogenesis is not occurring at an advanced level and that new, functional vessel formation is limited. The histological evidence also supports this as measurements of microvessel density in tissue sections decrease corresponding to the same pattern in the MR images. From a translational point of view this may be discouraging. However, chronic hypoxia generally leads to angiogenesis and this has been shown for human stroke (4). Therefore, discrepancies owing to choice of species and model (transient ischemia in a specific rat strain versus human stroke) should further be addressed.

5. CONCLUSION

In conclusion, SSCE MRI is a useful technique to noninvasively estimate changes in the microvasculature after stroke. Our results indicate that optimization of the MR acquisition parameters is essential in order to allow robust conclusions. The focus of our study in experimental stroke has been to probe for evidence of angiogenesis in the chronic stages. Immunohistochemistry revealed endothelial cell proliferation only in peri-infarct regions, which is a sign for early angiogenesis, but newly formed endothelial cells failed to translate into higher vessel densities and functional vasculature.

6. SUPPORTING INFORMATION

Supporting information can be found in the online version of this article.

Acknowledgments

The authors thank Drs Philippe Robert and Claire Corot (Guerbet) for the generous supply of Endorem and Matthias Weigel from the Medical Physics group of the University Hospital of Freiburg for stimulating discussions. Melanie Nelles is acknowledged for technical support with histology, Ingo Przesdzing from the Department of Experimental Neurology at the Charité in Berlin with tissue section analysis, and Michael Diedenhofen for technical assistance with the data analysis. Financial support was provided from the EU-FP7 program (HEALTH-F5-2008-201842; ENCITE) and the EU-FP6 program (LSHB-CT-2006-037526; StemStroke). Funds from the German Federal Ministry of Education and Research (BMBF-0314104) and an Alexander von Humboldt fellowship for T.D.F. are gratefully acknowledged. The funders had no role in study design, data collection, analysis, the decision to publish or preparation of the manuscript.

REFERENCES

1. Beck H, Plate KH. Angiogenesis after cerebral ischemia. Acta Neuropathol 2009;117(5):481–496.
2. Hayashi T, Deguchi K, Nagotani S, Zhang H, Sehara Y, Tsuchiya A, Abe K. Cerebral ischemia and angiogenesis. Curr Neurovasc Res 2006;3 (2):119–129.
3. Slevin M, Kumar P, Gaffney J, Kumar S, Krupinski J. Can angiogenesis be exploited to improve stroke outcome? Mechanisms and therapeutic potential. Clin Sci 2006;111(3):171–183.
4. Krupinski J, Kaluza J, Kumar P, Kumar S, Wang JM. Role of angiogenesis in patients with cerebral ischemic stroke. Stroke 1994;25 (9):1794–1798.
5. Krupinski J, Stroemer P, Slevin M, Marti E, Kumar P, Rubio F. Three-dimensional structure and survival of newly formed blood vessels after focal cerebral. Neuroreport 2003;14(8):1171–1176.
6. Neeman M, Gilad AA, Dafni H, Cohen B. Molecular imaging of angiogenesis. J Magn Reson Imag 2007;25(1):1–12.
7. Seevinck P, Deddens L, Dijkhuizen R. Magnetic resonance imaging of brain angiogenesis after stroke. Angiogenesis 2010;13(2):101–111.
8. Kiselev VG. On the theoretical basis of perfusion measurements by dynamic susceptibility contrast MRI. Magn Reson Med 2001;46 (6):1113–1122.
9. Dennie J, Mandeville JB, Boxerman JL, Packard SD, Rosen BR, Weisskoff RM. NMR imaging of changes in vascular morphology due to tumor angiogenesis. Magn Reson Med 1998;40(6):793–799.
10. Jensen JH, Chandra R. MR imaging of microvasculature. Magn Reson Med 2000;44(2):224–230.
11. Tropres I, Grimault S, Vaeth A, Grillon E, Julien C, Payen JF, Lamalle L, Decorps M. Vessel size imaging. Magn Reson Med 2001;45(3):397–408.
12. Wu EX, Tang HY, Jensen JH. High-resolution MR imaging of mouse brain microvasculature using the relaxation rate shift index Q. NMR Biomed 2004;17(7):507–512.
13. Bosomtwi A, Jiang Q, Ding GL, Zhang L, Zhang ZG, Lu M, Ewing JR, Chopp M. Quantitative evaluation of microvascular density after stroke in rats using MRI. J Cerebral Blood Flow Metab 2008;28 (12):1978–1987.
14. Lin CY, Chang C, Cheung WM, Lin MH, Chen JJ, Hsu CY, Chen JH, Lin TN. Dynamic changes in vascular permeability, cerebral blood volume, vascular density, and size after transient focal cerebral ischemia in rats: evaluation with contrast-enhanced magnetic resonance imaging. J Cerebral Blood Flow Metab 2008;28(8):1491–1501.
15. Moisan A, Pannetier N, Grillon E, Richard M-J, Fraipont F, Rémy C, Barbier EL, Detante O. Intracerebral injection of human mesenchymal stem cells impacts cerebral microvasculature after experimental stroke: MRI study. NMR Biomed 2012;25(12):1340–1348.
16. Longa E, Weinstein P, Carlson S, Cummins R. Reversible middle cerebral artery occlusion without craniectomy in rats. Stroke 1989;20 (1):84–91.
17. Kiselev VG, Posse S. Analytical model of susceptibility-induced MR signal dephasing: Effect of diffusion in a microvascular network. Magn Reson Med 1999;41(3):499–509.
18. Yablonskiy DA, Haacke EM. Theory of NMR Signal behavior in magnetically inhomogeneous tissues – the static dephasing regime. Magn Reson Med 1994;32(6):749–763.
19. Carr HY, Purcell EM. Effects of diffusion on free precession in nuclear magnetic resonance experiments. Phys Rev 1954;94(3):630–638.
20. Kiselev VG. Spin echo amplitude in biological tissue with implications for vessel size imaging. Joint Annual Meeting ISMRM-ESMRMB, Stockholm 2010;01-07052010(1):1792 (Proc.).
21. Hoehn-Berlage M, Eis M, Schmitz B. Regional and directional anisotropy of apparent diffusion coefficient in rat brain. NMR Biomed 1999;12(1):45–50.
22. Koay CG, Basser PJ. Analytically exact correction scheme for signal extraction from noisy magnitude MR signals. J Magn Reson 2006;179(2):317–322.
23. Paxinos G, Watson C. The Rat Brain in Stereotaxic Coordinates. Academic Press: San Diego, CA, 1998.
24. Bosomtwi A, Chopp M, Zhang L, Zhang ZG, Lu M, Jiang Q. Mean microvessel segment length and radius after embolic stroke: comparison of magnetic resonance imaging (MRI) and laser scanning confocal microscopy (LSCM). Brain Res 2011;1381(0):217–227.
25. Ullrich RT, Jikeli JF, Diedenhofen M, Böhm-Sturm P, Unruh M, Vollmar S, Hoehn M. In-vivo visualization of tumor microvessel density and response to anti-angiogenic treatment by high resolution MRI in mice. PLoS ONE 2011;6(5):e19592.
26. Neeman M, Dafni H. Structural, functional, and molecular MR imaging of the microvasculature. Annu Rev Biomed Eng 2003;5:29–56.
27. Grüne M, van Dorsten FA, Schwindt W, Oláh L, Hoehn M. Quantitative T*(2) and T'(2) maps during reversible focal cerebral ischemia in rats: separation of blood oxygenation from nonsusceptibility-based contributions. Magn Reson Med 1999;42(6):1027–1032.
28. He X, Yablonskiy DA. Quantitative BOLD: mapping of human cerebral deoxygenated blood volume and oxygen extraction fraction: default state. Magn Reson Med 2007;57(1):115–126.
29. Turner R. How much cortex can a vein drain? Downstream dilution of activation-related cerebral blood oxygenation changes. NeuroImage 2002;16(4):1062–1067.
30. Xu C, Schmidt WUH, Villringer K, Brunecker P, Kiselev V, Gall P, Fiebach JB. Vessel size imaging reveals pathological changes of microvessel density and size in acute ischemia. J Cerebral Blood Flow Metab 2011;31(8):1687–1695.
31. Xu C, Schmidt WUH, Galinovic I, Villringer K, Hotter B, Ostwaldt AC, Denisova N, Kellner E, Kiselev V, Fiebach JB. The potential of microvessel density in prediction of infarct growth: a two-month experimental study in vessel size imaging. Cerebrovasc Dis 2012;33 (4):303–309.

Full Paper

Vascular changes after stroke in the rat: a longitudinal study using optimized magnetic resonance imaging

Philipp Boehm-Sturm, Tracy D. Farr, Joanna Adamczak, Jan F. Jikeli, Luam Mengler, Dirk Wiedermann, Therése Kallur, Valerij Kiselev and Mathias Hoehn

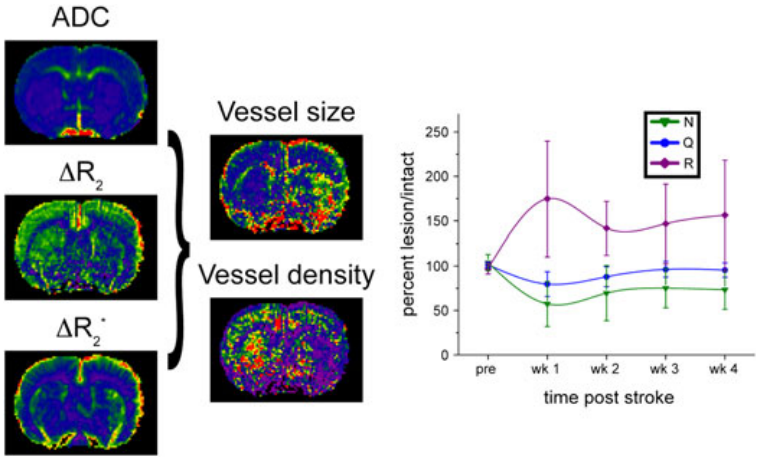

We investigated the evidence of angiogenesis after transient focal ischemia in rats using SSCE MRI, which measures diffusivity of tissue and changes in transverse relaxation rates upon i.v. administration of superparamagnetic particles. Important vessel characteristics such as blood volume, vessel size and vessel density were calculated and followed up to 4 weeks after the stroke. Following stroke, vessel size increased, whereas blood volume in small vessels and vessel density decreased, indicating limited potential of ischemic tissue to form new, functional vasculature.

III.

Optimizing bioluminescence sensitivity for noninvasive imaging of neural stem cell grafts in the mouse brain.

Markus Aswendt*, Joanna M. Adamczak*, Sebastian Couillard-Depres, Mathias Hoehn
PLoS ONE (2013) 8(2): e55662
(*: authors contributed equally)

OPEN ACCESS Freely available online

PLOS ONE

Boosting Bioluminescence Neuroimaging: An Optimized Protocol for Brain Studies

Markus Aswendt[1☯], Joanna Adamczak[1☯], Sebastien Couillard-Despres[2,3], Mathias Hoehn[1]*

1 In-Vivo-NMR Laboratory, Max-Planck-Institute for Neurological Research, Cologne, Germany, **2** Institute of Molecular Regenerative Medicine, Paracelsus Medical University, Salzburg, Austria, **3** Spinal Cord Injury and Tissue Regeneration Center Salzburg (SCI-TReCS), Salzburg, Austria

Abstract

Bioluminescence imaging is widely used for optical cell tracking approaches. However, reliable and quantitative bioluminescence of transplanted cells in the brain is highly challenging. In this study we established a new bioluminescence imaging protocol dedicated for neuroimaging, which increases sensitivity especially for noninvasive tracking of brain cell grafts. Different D-Luciferin concentrations (15, 150, 300 and 750 mg/kg), injection routes (iv, ip, sc), types of anesthesia (Isoflurane, Ketamine/Xylazine, Pentobarbital) and timing of injection were compared using DCX-Luc transgenic mice for brain specific bioluminescence. Luciferase kinetics was quantitatively evaluated for maximal photon emission, total photon emission and time-to-peak. Photon emission followed a D-Luciferin dose-dependent relation without saturation, but with delay in time-to-peak increasing for increasing concentrations. The comparison of intravenous, subcutaneous and intraperitoneal substrate injection reflects expected pharmacokinetics with fastest and highest photon emission for intravenous administration. Ketamine/Xylazine and Pentobarbital anesthesia showed no significant beneficial effect on maximal photon emission. However, a strong difference in outcome was observed by injecting the substrate pre Isoflurane anesthesia. This protocol optimization for brain specific bioluminescence imaging comprises injection of 300 mg/kg D-Luciferin pre Isoflurane anesthesia as an efficient and stable method with a signal gain of approx. 200% (compared to 150 mg/kg post Isoflurane). Gain in sensitivity by the novel imaging protocol was quantitatively assessed by signal-to-noise calculations of luciferase-expressing neural stem cells grafted into mouse brains (transplantation of 3,000–300,000 cells). The optimized imaging protocol lowered the detection limit from 6,000 to 3,000 cells by a gain in signal-to-noise ratio.

Citation: Aswendt M, Adamczak J, Couillard-Despres S, Hoehn M (2013) Boosting Bioluminescence Neuroimaging: An Optimized Protocol for Brain Studies. PLoS ONE 8(2): e55662. doi:10.1371/journal.pone.0055662

Editor: Stefano L. Sensi, University G. D'Annunzio, Italy

Received November 7, 2012; **Accepted** December 28, 2012; **Published** February 6, 2013

Funding: This work was financially supported by grants from the Volkswagen Foundation (I/83 443) and the EU-FP7 program ENCITE (HEALTH-F5-2008-201842) and TargetBraIn (HEALTH-F2-2012-279017). The funders had no role in study design, data collection and analysis, decision to publish, or preparation of the manuscript.

Competing Interests: The authors have declared that no competing interests exist.

* E-mail: mathias@nf.mpg.de

☯ These authors contributed equally to this work.

Introduction

Noninvasive imaging has gained high interest for cell tracking approaches in preclinical studies of stem cell transplantation. Bioluminescence imaging (BLI) is one of the methods to overcome the restrictions of conventional invasive histological evaluations of stem cell fate and localization. Bioluminescence (BL) is based on the oxidation of the substrate D-Luciferin in the presence of oxygen and ATP by the enzyme luciferase, which was first isolated from the firefly *Photinus pyralis* [1]. Cell localization is achieved by the specific light signal generated only by genetically modified cells expressing a luciferase gene. In case of the firefly luciferase the enzyme reaction is ATP-dependent and therefore serves also as an indicator for cell viability. In addition, gene expression is quantifiable based on the linear relationship between substrate and photon emission.

In vivo BLI is challenged by tissue related light absorbance from hemoglobin and melanin. The high blood to brain tissue ratio is particularly unfavorable for most luciferase imaging since their wavelength-windows of maximal emission overlap with the maximal absorption of hemoglobin. The photon transmission in living brain tissue is limited substantially by the multilayer anatomical barriers (skin, bone, meninges, brain tissue). Furthermore, the blood brain-barrier reduces diffusion of the luciferase substrate or even selectively transports the substrate back to the blood system [2].

For a maximized sensitivity, the technical set-up especially with an up-to-date CCD camera system is a prerequisite. At the cellular level, the photon emission per cell can be maximized by using a strong promoter and single cell cloning approaches to identify high-expression clones, which enable the detection of individual subcutaneous tumor cells in vivo [3]. On the other side, physiological parameters during in vivo imaging such as the type of anesthesia [4] and the route of substrate delivery [5,6] influence decisively BL signal outcome and experimental stability. D-Luciferin biodistribution and cell uptake kinetic studies have revealed a limitation of light emission due to restricted substrate availability, particularly in the brain [7]. Nevertheless, the general imaging protocol seems to vary substantially between studies.

Own survey on recent BLI literature indicated that many labs use an ip injected luciferin dose of 150 mg/kg under Isoflurane – a condition which we call "standard protocol" in the following investigation. The aim of our present study was to establish an optimized protocol for BLI sensitivity and reproducibility,

dedicated for imaging investigations on the rodent brain. For this purpose, we assessed the following parameters influencing the BLI signal: 1) substrate concentration, 2) substrate injection route, and 3) type of anesthesia (Isoflurane, ketamine/xylazine, Pentobarbital) and its timing relative to substrate application. The effect of the above listed parameters on maximal photon emission (PE_{max}), on total photon emission (represented by area-under-curve, AUC), and on in- and efflux kinetics of D-Luciferin (time-to-peak) was investigated. Brain-specific BLI was obtained with DCX-Luc transgenic mice expressing firefly luciferase specifically under control of the doublecortin (DCX) promoter, which is active in migrating neuroblasts and early-stage differentiated neurons. This mouse model is proven to serve as a suitable tool to follow neurogenesis in the brain [8]. Based on the evaluation of the different protocols with the transgenic mouse line, we tested the optimized protocol on nude mice, which received implants of distinct amounts of neural stem cells (NSCs) expressing the firefly luciferase. This in vivo dilution series of grafted cells served to validate our optimized protocol for maximized sensitivity for brain imaging applications.

Materials and Methods

1. Animals and Ethics Statement

Heterozygous DCX-Luc mice (n = 4) with C57/Bl6 albino background (B6(Cg)-Tyrc-2J/J) were used for optimization of the brain BLI protocol. Experiments were carried out with 4–6 months old mice. For BLI optimization, each DCX-Luc mouse underwent 12 times BLI measurements including D-Luciferin injections and anesthesia. In general, the time delay between two experiments were 2 days or more. Cell transplantations were performed with 12 male Nu/Nu mice (Janvier, Saint Berthevin Cedex, France). These mice were measured with two different BLI protocols with a time delay of 6 h or more. All animal experiments were conducted according to the guidelines laid out in the German Animal Welfare Act, in accordance with the European Council Directive 2010/63/EU, and were approved by the local authorities (Landesamt für Natur, Umwelt und Verbraucherschutz North Rhine-Westphalia, reference number 84-02.04.2011.A123). Animals were housed in individually ventilated cages under 12 h light/12 h darkness cycle with access to water and food *ad libitum*.

2. Cell Culture

The generation of neural progenitor cells (NPCs) from murine embryonic stem (mES) cells was achieved by adaption of previously described protocols [9]. The mES cell line D3 [10] (a generous gift of Dr. Tomo Saric, Institute of Neurophysiology, University at Cologne, Germany) was cultured on mitotically inactivated mouse fibroblast cells as previously described [11]. Embryoid body (EB) formation was induced in suspension for 4 days in DMEM supplemented with 15% FCS (Gibco, Darmstadt, Germany), 1× non-essential amino acids (PAA, Pashing, Austria), 2 mM L-glutamine (PAA), 1% penicillin/streptomycin (PAA). EBs were converted into neurosphere-like aggregates by culturing in N2/B27 medium consisting of DMEM/F12 (Gibco), Neurobasal (Gibco), 1× B27 (Gibco), 1× N2 (Gibco) and 2 mM L-glutamine (PAA), changing medium every 3–4 days on Poly-HEMA (Sigma-Aldrich, Schnelldorf, Germany) coated flasks. After 10–14 days, neurospheres were plated on flasks coated with 0.2% gelatin (Sigma-Aldrich). 24 hours later, medium was changed to N2Euro medium consisting of Euromed (Biozol, Eiching, Germany), 10 ng/ml EGF (Peprotech, Hamburg, Germany), 10 ng/ml b-FGF (Peprotech), 50 µg/ml BSA (PAA), 25 µg/ml Insulin (Sigma-Aldrich) and 1× N2 (Gibco). The N2Euro medium promoted proliferation of EGF and b-FGF responsive stem cells, while non-NSCs were removed by culturing and passaging with Accutase (PAA) for 20 days until the final D3WT_N2Euro cell line was established. Cells were cultured under humidified 5% CO_2 and 95% air.

3. Cloning of Luc2 Retroviral Plasmid and Generation of Transgenic NPCs

The retroviral plasmid pBabe-Luc2-T2A-copGFP-SV40P-Neo consisted of the codon optimized firefly luciferase Luc2, the ''self-cleaving'' 2A-like peptide sequences T2A for efficient multicistronic reporter expression, the superbright fluorescent protein copGFP from the copepod *Pontenilla plumata* (excitation/emission maximum = 482/502 nm) [12] and the antibiotic resistence gene neomycin (Neo) for clone selection. Retroviral packaging was done according to established protocols with transfection of the packaging Plat-E cells, which express the gag-pol and ecotropic envelope proteins [13]. The plasmid was cloned by amplifying recombinant DNA by PCR using specific primers bearing appropriate restriction sites in 2 steps: 1) Luc2 was cloned from pGL4.14 (Promega, Madison, USA) into pCDH-EF1-MCS-T2A-copGFP (Biocat, Heidelberg, Germany) with the following primer pair Luc2-*BamHI*-for (AAGGGAAA*GGATCC*GCCACCATG-GAAGATATGCCAAAAACATTAAG) and Luc2-*NotI*-rev (AAATTT*GCGGCCGC*CACGGCGATCTTGC), 2) the resulting Luc2-T2A-copGFP fragment was cloned into pBabe-Neo-GIT (a generous gift of Prof. Andreas Jacobs, European Institute of Molecular Imaging, Münster, Germany) by restriction with BamHI and NotI. Successful cloning was verified by restriction analysis and sequencing.

4. Ecotrope Transduction and Selection of Stable Transgenic NSCs

Retroviral packaging of Plat-E cells was done according to manufacturers protocol with small modifications (Cell Biolabs, San Diego, USA). Briefly, Plat-E cells were plated 24 h before the transfection at $1\times10^5/cm^2$ in 0.25 ml/cm^2 DMEM FCS (without antibiotics). The transfection mix consisted of 0.2 µg/cm^2 plasmid DNA, 20 µl/cm^2 Optimem (Gibco) plus 0.2 µl/cm^2 Lipofectamine Plus Reagent, and 0.25 µl/cm^2 Lipofectamine (Gibco) and was added dropwise to the cells covered with 0.1 ml/cm^2 Optimem containing Chloroquine (final conc.: 25 µM) and incubated for 24 h. After virus collection 48 h post transfection, the virus was used for retroviral infection of proliferating D3WT_N2Euro cells (non-confluent culture in 24-well plate), by adding 200 µl Optimem containing 7.5 ng/ml Polybrene and 200 µl virus-supernatant for 24 h. In a first step of transgenic cell selection, 500 µg/ml G-418 was added to the media. In a second step, cells were FACS-sorted (FACSAria III, BD Biosciences, San Jos, USA) according to the copGFP expression – performed to assure Luc2 expression in an equimolar range. Sustained cell viability was confirmed by PrestoBlue assay according to the manufacturers protocol (Invitrogen, Darmstadt, Germany) and measured with a microplate reader (Mithras LB940, Berthold, Bad Wildbad, Germany). In the following, we will refer to the transgenic NSCs as NSC^{Luc2+} and to non-transduced NSCs as NSC^{WT}.

5. Cell Transplantations

Nude mice were anesthetized with Isoflurane in O_2:N_2O (30:70%), and 4 mg/kg Carprofen (Pfizer, Berlin, Germany) was used for analgesia. During surgery, mice remained fixed in a stereotactic frame (Stoelting, Dublin, Ireland). The skull was

exposed by a small incision and one hole was drilled at the following coordinates relative to bregma: AP +0.5; L +2.0; DV −3.0 using a stereotactical instrument (Stoelting). The homogeneous cell suspensions were kept on ice during surgery and were subsequently injected into the brain through a Hamilton syringe (26G needle) using a micropump system with flow rates of 1.500 nl/min (withdrawal) and 500 nl/min (injection). Cell amounts were adjusted to 3×10^3, 6×10^3, 3×10^4 and 3×10^5 cells (n = 3 for each cell number) and injected in a volume of 2.0 µl after leaving the needle in place for 5 min. The wound was closed with a non-colored suture (Resorba, Nürnburg, Germany), and BLI was applied 24 h later.

6. In vitro and in vivo Imaging Set-up

D-Luciferin (Synchem, Felsberg, Germany) solutions were prepared by dilution in phosphate buffered saline (PBS) to obtain 3, 20, 50 and 100 mg/ml stock solutions, which were filtered sterile prior to use and stored at -20°C. In vitro sensitivity was evaluated with NSC^{Luc2+} and NSC^{WT} plated in different cell densities of 3×10^3, 6×10^3, 3×10^4 and 3×10^5 cells in black 96-wells (Corning, Tewksbury, USA), in four wells per condition. D-Luciferin was added in excess (0.3 mg/ml, ≈1 mM according to [1]) and the plate was subsequently measured for BLI recording data on the Photon Imager (Biospace Lab, Paris, France) for 1 min.

Before the first BLI recording, animals were shaved under Isoflurane anesthesia on the head region and on the back of similar size using a conventional hair shaver (Typ 1556, ermila, Unterkirnach, Germany). Shaving was repeated when necessary according to visual inspection. Animals were injected intraperitoneally (ip) using a 1 ml syringe with 30 gauge needle. For intravenous (iv) injections, a catheter with 30 gauge needle was placed into the tail vein, flushed with saline and 1 units/ml heparin (Braun, Melsungen, Germany). Injection volume for different D-Luciferin concentrations (15–750 mg/kg) was kept constant (approx. 200 µl) by using the appropriate stock concentration. Anesthesia was induced either by 2% Isoflurane (Iso) in 100% O_2, or subcutaneous (sc) injection of 60 mg/kg Pentobarbital (Pento), or ip injection of 100/10 mg/kg Ketamine/Xylazine (Ket/Xyl). The impact of anesthesia on photon emission was investigated in 4 DCX-Luc mice by comparing the standard procedure −150 mg/kg post Isoflurane (post-Iso) to substrate administration pre Isoflurane (pre-Iso) and injection of 150 m/kg after Pentobarbital or Ketamine/Xylazine anesthesia. In order to induce rapid Isoflurane anesthesia for the pre-Iso condition, an initial dose of 4% Isoflurane in 100% O_2 was used. The time lag between substrate injection and acquisition was recorded during each BLI experiment and used for time-line correction (acquisition time = 30 min) in order to facilitate precise data evaluation. The time lag ranged from 30 s (e.g. ip injections) to 3 min (e.g. iv injections and pre-Iso condition).

7. Data Analysis and Statistics

For in vitro analysis, photon emission per NSC^{Luc2+} was calculated from a dilution series by dividing the photons/s/cm^2/sr per well by the cell amount and averaging of 4 individual experiments.

In vivo BLI data was analyzed using the M3software (Biospace) with size-constant regions of interest (ROIs) over the brain and the back of the animal, manually drawn and based on anatomical landmarks (ears, eyes) on equally scaled BL images. Further calculations, plotting and statistical analysis were done with Veusz (GPL, Jeremy Sanders) and Origin 8G (OriginLab Corporation, Northampton, USA) according to previously described methods [14]. Dynamic time curves were obtained with 5 and 60 s temporal resolution for two regions of interest (ROIs) for each animal and experiment. The brain-specific signal was corrected for unspecific signal taken from a ROI on the skin of the animal's back. The 5 s and 60 s data from the ROI on the animal's back was subtracted from the 5 s and 60 s brain data. This correction reduced the inter-individual differences from endogenous variations in DCX-expression and exogenously administered D-Luciferin (see Supplementary Fig. 1). The maximum photon emission (PE_{max}) was determined from the acquisition of the signal-time curve, recorded with 5 s temporal resolution and by calculating the 95th percentile. The area-under-curve (AUC) value was calculated by numerical integration for comparing the total photon yield from the same acquisition. The maximum value in the 60 s resolution data was used for defining the time-to-peak value. Furthermore, the slope of the signal increase during the initial 5 min was determined for every acquisition by linear fitting of the data points. Signal-to-noise ratio (SNR) was calculated by dividing mean photon flux (ph/s/cm^2/sr) by the standard deviation of the noise. For accurate calculation of the noise, the mean of 3 randomly chosen ROIs outside the mouse was calculated.

All data are represented as mean ± SD. Unpaired t test was used to compare means of 2 groups for in vitro experiments. In vivo BLI data was analysed using a repeated measures ANOVA for each individual test regime (concentration, injection route, anesthesia, time of injection). Post hoc comparisons were corrected for multiple comparisons using Sidak correction. A p-value smaller than 0.05 was considered to be significant.

Results

1. Substrate Concentration Dependent Increase in Photon Flux

The impact of substrate concentration on photon emission was investigated by injecting 15, 150, 300 or 750 mg/kg D-Luciferin ip into DCX-Luc mice (n = 4) after 2% Isoflurane anesthesia, and subsequent BLI recording for 30 min. Substrate concentration had a significant effect on PE_{max} ($F(1.006, 3.017) = 72.862$ $p = 0.003$), AUC ($F(1.005, 3.016) = 66.988$) $p = 0.004$) and time-to-peak ($F(3, 9) = 28.693$, $p<0.001$). The PE_{max} signal exponentially increased with substrate concentration in every animal, as well as the total quantum yield represented by the AUC (Fig. 1a). A 5-times standard concentration resulted in approx. 10-fold PEmax/AUC value, together with increased error (standard deviation). This strong signal enhancement was accompanied by higher slope values in the initial inflow phase following also the exponential relationship (1.1×10^5–2.9×10^6) and a prolonged time-to-peak for high substrate concentrations (Fig. 1b, c).

2. Influence of Substrate Injection Route

The impact of substrate injection routes was evaluated by injecting 150 mg/kg D-Luciferin ip, sc, or iv followed by acquisition for 30 min in DCX-Luc mice (n = 4). Injection route had a significant effect on PE_{max} ($F(2, 6) = 75.048$ $p<0.001$), AUC ($F(2, 6) = 126.935$ $p<0.001$) and on time-to-peak ($F(2, 6) = 71.148$ $p<0.001$). According to the general model of drug absorption and resorption [15], the PE_{max} for sc reached approx. 40% of the ip experiment, whereas iv resulted in approx. 450% PE_{max}. The AUC values showed a similar behavior with a minor effect for iv - approx. 260% (Fig. 2a). The absorption kinetics was also reflected by the BLI dynamic time curves with a smaller slope for sc vs. ip ($6.1\times10^4\pm2.2\times10^3$ vs. $2.2\times10^5\pm8.6\times10^3$). The absorption-independent iv injection reached with 234% of ip the highest slope

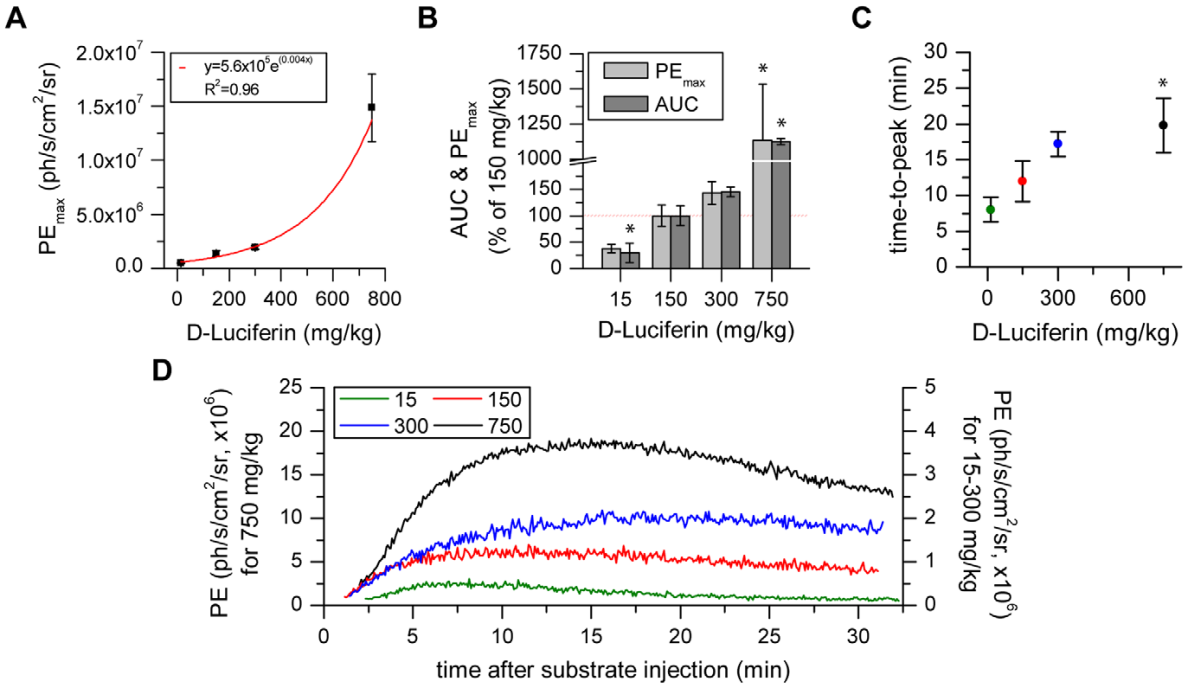

Figure 1. Substrate concentration modulates luciferase activity. a, b) The PE_{max} and AUC values increase exponentially with the D-Luciferin concentration. c) The time for maximal luciferase activity is dependent on the substrate concentration. d) The slope of initial photon emission kinetics is concentration dependent. (* statistically significant difference with $p \leq 0.05$ to standard protocol 150 mg/kg post-Iso in post hoc comparison with Sidak correction).
doi:10.1371/journal.pone.0055662.g001

$(5.1 \times 10^5 \pm 6.2 \times 10^4)$ for the initial 5 min photon flux (Fig. 2b). This effect contributed directly to the faster biodistribution for iv injections (8.7 min less than ip) and the delay in the time-to-peak for sc (additional 4.4 min compared to ip) (Fig. 2c).

3. Anesthesia-dependent Photon Flux Changes

Based on previous reports describing the inhibitory effects of volatile anesthetics and the benefit of injection anesthetics like medetomidine [4], we sought to compare luciferase performance for common injection anesthetics: Pentobarbital and Ketamine/Xylazine. In a first experiment, DCX-Luc mice (n = 4) were injected with 15, 150 and 300 mg/kg D-Luciferin pre and post induction of Isoflurane anesthesia, in order to determine the influence of an anesthesia pre-inhibited enzyme. D-Luciferin injection pre Isoflurane anesthesia resulted in significantly increased PE_{max} ($F(1, 3) = 51.585$ $p = 0.006$) and AUC ($F(1, 3) = 44.488$ $p = 0.007$). By increasing the substrate concentration the maximum and total amount of photon flux difference for pre to post condition was significantly increased (300 mg/kg to

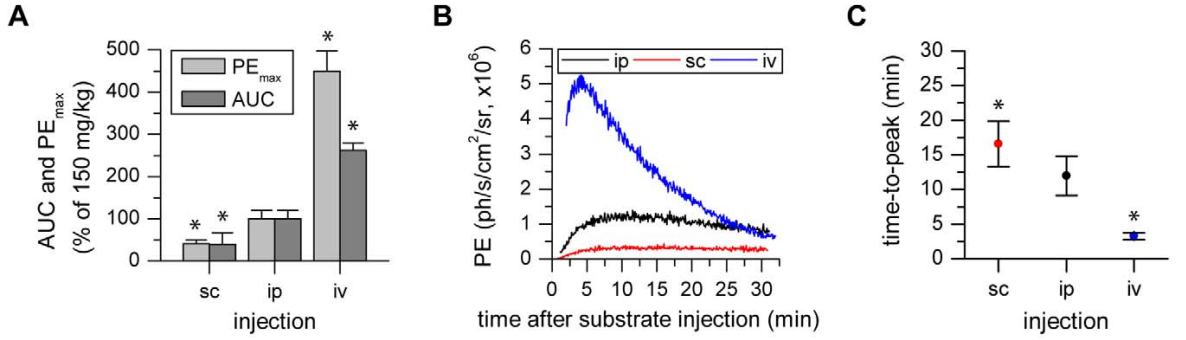

Figure 2. The photon flux maximum and timing are dependent on the route of substrate administration. a, b) The PE_{max} and AUC increase corresponding to the physiologically expected biodistribution for sc, ip and iv substrate administration, reflected by the characteristic time activity curves. c) Maximal photon flux is reached at minimal time for iv injections followed by ip and sc (* statistically significant difference with $p \leq 0.05$ to standard protocol 150 mg/kg post-Iso in post hoc comparison with Sidak correction).
doi:10.1371/journal.pone.0055662.g002

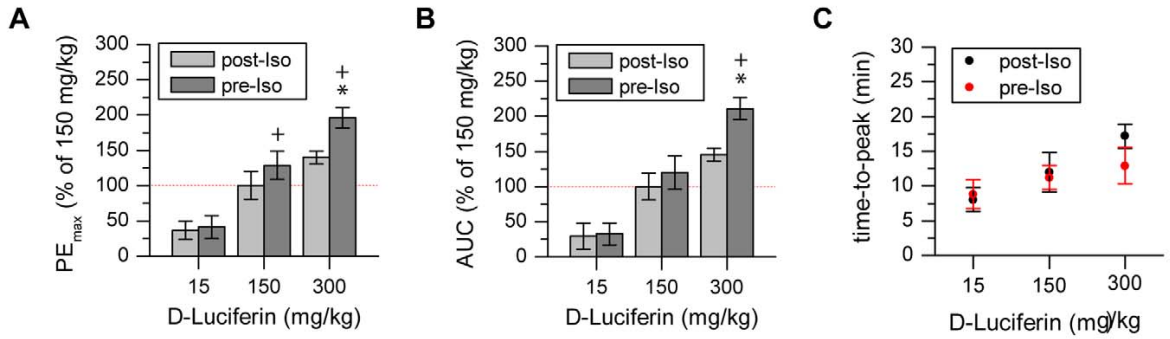

Figure 3. Luciferase inhibition by Isoflurane is avoided by substrate administration before anesthesia onset. a, b) Difference in PE_{max} and AUC under pre/post Isoflurane conditions becomes more pronounced with increasing substrate concentration. c) The order of application between Isoflurane anesthesia and substrate had no impact on the time-to-peak for 15, 150 and 300 mg/kg D-Luciferin. (* statistically significant difference with $p \leq 0.05$ to standard protocol 150 mg/kg post-Iso in post hoc comparison with Sidak correction;+statistically significant difference with $p \leq 0.05$ between pre and post condition in post hoc comparison with Sidak correction).
doi:10.1371/journal.pone.0055662.g003

150 mg/kg pre Iso: PE_{max} $p = 0.01$, AUC $p = 0.009$) (Fig. 3a, b). The time-to-peak suggested a similar D-Luciferin concentration-dependent effect; this, however, did not reach the level of statistical significance (Fig. 3c).

In a second experiment, brain specific BLI was compared for different anesthetics revealing an overall effect on PE_{max} ($F(2, 6) = 5.935$ $p = 0.038$) but no significant increase or decrease compared to Isoflurane anesthesia in post-hoc pairwise comparison (Ketamine/Xylazine: $p = 0.058$, Pento: $p = 0.742$). A significantly lower AUC value for Ketamine/Xylazine compared to Isoflurane ($F(2, 6) = 22.738$ $p = 0.002$; post-hoc $p = 0.005$) (Fig. 4) was accompanied by delayed time-to-peak values. No significant difference between the Isoflurane and Pentobarbital group was observed for time-to-peak.

4. Generation of Neural Stem Cells Expressing Luc2 and copGFP

The NSCs D3WT_N2Euro were stably transduced with the retroviral plasmid pBABE-Luc2-T2A-copGFP-Neo and sorted for copGFP/neomycin resistance to reveal a stable transgenic cell line without an effect on cell viability (Fig. 5). The NSC^{Luc2+} emit approx. 7 photons/s/cell under substrate excess (1 mM D-Luciferin) and show a linear correlation between cell number and photon emission under substrate excess.

5. Imaging Protocol-dependent in vivo Detection Limits

BLI was performed 24 h after transplantation of 3,000, 6,000, 30,000 or 300,000 NSC^{Luc2+} into the striatum of nude mice (for each cell amount, $n = 3$), repeating the in vitro dilution series under in vivo conditions in order to determine detection limits. The mice were scanned with both protocols (150 mg/kg post Isoflurane and 300 mg/kg pre Isoflurane –6 h time separation) for 30 min. The BLI detection limit was calculated assuming a $SNR \geq 3$ for a reliably detectable signal. A representative image series with the corresponding SNR values is shown in Fig. 6a. This evaluation revealed the primary advantage of the new protocol, which, on average, leads to a 2.35-fold SNR increase. This sensitivity increase can be exploited for reliable detection of half the amount of cells visible using the standard protocol. The PE_{max} values for the grafts of various cell numbers, show a linear relationship with cell number (Fig. 6b).

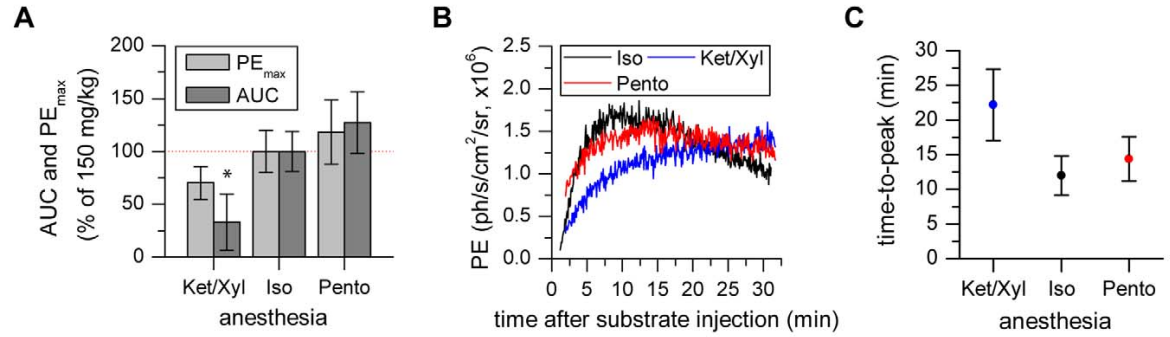

Figure 4. Photon flux is modulated by the type of anesthesia. a) PE_{max} and AUC were decreased under Ketamine/Xylazine conditions but not different for Pentobarbital compared to Isoflurane. b, c) Representative time activity curves showing the anesthesia dependent signal behavior leading to delayed time-to-peak for Ketamine/Xylazine, but no clear difference between Isoflurane and Pentobarbital anesthesia. (* statistically significant difference with $p \leq 0.05$ to standard protocol 150 mg/kg post-Iso in post hoc comparison with Sidak correction).
doi:10.1371/journal.pone.0055662.g004

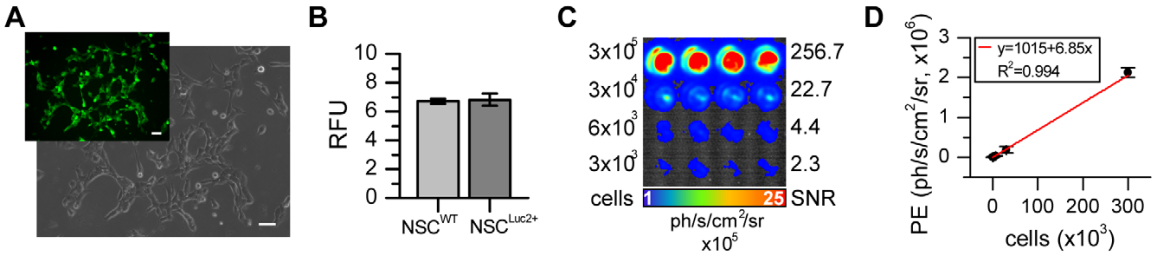

Figure 5. Characterization of Luc2-expressing NSCs. a) Efficient NSC transduction and selection process (by FACS and antibiotics) was confirmed by the homogeneous expression of the fluorescent reporter copGFP, which directly reflects Luc2 expression because of the T2A linker element (microscopic images 20× magnification, 50 µm scale bar). b) Reporter gene expression had no impact on cell viability, as confirmed with the PrestoBlue assay (data of 5 independent measurements presented as relative fluorescent units, RFU). c, d) Quantitative analysis of NSC^{Luc2+} dilution series (1 min acquisition at 37°C with 30 µg/ml D-Luciferin) revealed a linear correlation between photon emission and cell number, as well as SNR in vitro.
doi:10.1371/journal.pone.0055662.g005

Discussion

Bioluminescence imaging is emerging as a valuable tool for tracking transplanted (stem) cells in various disease models [16–19]. However, a publication survey on 20 recent reports from 2008–2012, performed in preparation of the present study, revealed the lack of a consistent protocol for in vivo BLI, but with a strong tendency to 150 mg/kg D-Luciferin injected intraperitoneally which we have used as our reference "standard protocol". This standard protocol has proved useful, primarily for peripheral applications, e.g. subcutaneous tumor cell transplants, where signal is mostly used and interpreted qualitatively. However, for a quantitative and sensitive bioluminescence imaging approach, this standard protocol does not necessarily meet the special requirements of brain imaging.

In this study, we evaluated the basic factors affecting the neuron-specific BL signal in transgenic DCX-Luc mice, including substrate concentration, route/timing of substrate administration and the type of anesthesia. The repetitive BLI measurements did not alter the BLI signal over time. As indicated by stability measurements (data not shown), repetition of the same protocol showed low variability of approx. 8%. The intrinsic inter-individual variability was 12±2%. An advanced protocol (300 mg/kg pre-Iso) was identified, which results in a 2-fold BL signal increase, while remaining user-friendly, fast applicable and cost-effective. We proved the advantages of the new protocol by boosting the sensitivity for a cell tracking approach in the mouse brain by a factor of 2 relative to the standard protocol, enabling the quantitative detection of 3,000 transplanted NSCs under the novel protocol conditions.

1. Concentration Dependent Increase in Photon Flux

The properties of the luciferase enzyme expressed in mammalian cells are well studied under in vitro conditions but missing for the in vivo situation – especially for brain specific BLI. We explored a dose-dependent BLI signal which followed an exponential increase. As was reported for 450 mg/kg D-Luciferin, in our experiments also 750 mg/kg did still not result in saturating photon emission levels. The exponential signal increase can be explained by a boost in substrate diffusion into the brain parenchyma exceeding a critical plasma level to facilitate blood brain-barrier penetration efficiently at 750 mg/kg. This is supported by the nearly 10-fold steeper slope, which most

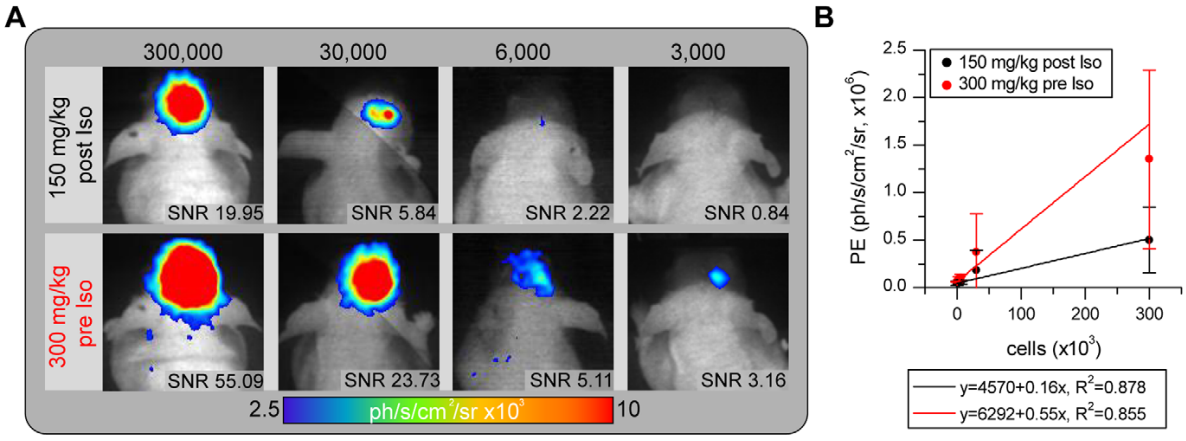

Figure 6. Photon emission is substantially increased by the modified BLI protocol. a) Representative images (equally scaled) for each cell number grafted into nude mice acquired with the standard protocol (upper row) and with the advanced protocol (lower row) reveal the objective sensitivity benefit, which is also represented in the quantitative SNR values. b) Correlation between photon emission and cell number revealed a linear relationship under in vivo conditions, with a steeper slope for the novel protocol, indicating the increased sensitivity.
doi:10.1371/journal.pone.0055662.g006

prominently represents the substrate inflow dependent photon emission in the first 5 min of acquisition.

Considering an in vitro firefly K_M of 1 mM or 0.3 mg/100 µl [20], this concentration should be reached by injection of 30 mg/kg D-Luciferin (assuming 2 ml total blood volume for a 20 g mouse). Nevertheless, by further increasing the substrate concentration, higher PE_{max} are achieved, which means that 30 mg/kg D-Luciferin is not the in vivo concentration at which the luciferase reaction rate is half of the maximum. Our results contradict previous assumptions, that the enzyme is already saturated at low substrate concentrations (5 µl of 100 mM) for subcutaneous applications in vivo [21]. However, under in vivo conditions substrate absorption and resorption is not 100% effective, meaning that not every injected molecule will reach a Luc-positive DCX neuron in the brain. Most importantly, Berger and colleagues calculated that only 5% of blood plasma D-Luciferin reach the brain [22], which explains the increasing luciferase activity at substrate concentrations which would already exceed K_M under in vitro conditions. At high substrate concentrations [21], the time-to-peak is significantly delayed. Under in vitro conditions, this would clearly be reflected in the conformational change of the luciferase enzyme, temporarily reducing the catalytic rate [23]. However, for the equivalent in vivo observation we rather suggest that high concentrations of D-Luciferin result in a prolonged concentration gradient between plasma and brain tissue facilitating a continued concentration increase at the target cells. A toxicity effect of the different D-Luciferin concentrations is not expected, as majority of studies have reported no toxic effect [24,21,25–27].

2. Influence of Injection Route

The advantage of D-Luciferin as an imaging substrate is its ability to distribute rapidly in the blood system, pass cell membranes and enters every organ (even through the placenta and blood brain-barrier) [21,28,29]. We validated the influence of the substrate injection route on the brain bioluminescence signal, by comparing sc, iv and ip injection of 150 mg/kg D-Luciferin and acquiring BLI in list mode for superior temporal resolution. According to reports about BLI of subcutaneously transplanted cells [5,6], the substrate pharmacokinetics limits the bioluminescence signal. The absorption-independent iv injection leads to a 400% maximum photon emission in ¼ the time compared to the ip injection. In contrast, after ip injection the substrate is slowly absorbed into the vascular space, which limits bioavailability and finally reduces PE_{max} while prolonging time-to-peak [6,30]. In contrast to a study of Inoue et al. the sc injection resulted in the lowest photon emission accompanied with a small slope and long time-to-peak value [5]. Although iv injection generates highest photon flux, we decided to use ip injection for the advanced protocol. The disadvantage of iv injections is the fast kinetics with lack of a plateau phase, which impedes reproducible measurements at the PE_{max} and induces additional error. The ip injection can be done with a high success rate [5], a shorter time (more mice can be measured the same time), repetitively without tissue irritation through tail vein catheterization and permits experimental flexibility by a prolonged steady-state BLI signal.

3. Anesthesia-dependent Photon Flux Changes

In vivo BLI of subcutaneously transplanted cells was reported to be strongly affected by the type of anesthesia [4]. Therefore, we investigated the effect of different anesthetics (Iso, Ket/Xyl, Pento) and the different anesthetic timing (D-Luciferin injection pre and post Iso) on brain-specific BLI. We observed a decrease in PE_{max} values for Ketamine/Xylazine anesthesia and a slight increase in PE_{max} for Pentobarbital anesthesia compared to our standard protocol using Isoflurane, however, this modulation did not reach a level of statistical significance. In vitro, Keyearts et al. found no direct inhibitory effect of Ketamine, Medetomidine (belonging to the same family of α2 adrenoreceptor agonists like Xylazine) or Pentobarbital [4]. Therefore, the modulation we observed in vivo may be the result of an altered hemodynamic situation, changing luciferase substrate distribution [31] and thereby indirectly influencing BLI signal intensity and kinetics. Nevertheless, anesthetics can have different effects on the blood system [32,33]. In a comparison study, Isoflurane resulted in the smallest reduction of cardiac output, followed by Pentobarbital with medium reduction. The strongest impact on cardiac output is expected under Ketamine/Xylazine anesthesia, which induces hypotension, bradycardia and hypothermia [32,34]. Although cerebral hemodynamics are autoregulated, the grading of the hemodynamic changes parallels our observation of delayed time-to-peak values for Pentobarbital and Ketamine/Xylazine anesthesia compared to Isoflurane.

The slight difference in PE_{max} between Pentobarbital and Isoflurane anesthesia may be due to the direct inhibitory effect of Isoflurane on the luciferase enzyme, which we studied by comparing pre vs post Isoflurane anesthesia. D-Luciferin injection before anesthesia consistently resulted in higher PE_{max}/AUC compared to the standard protocol (substrate injection into the anaesthetized animal). Direct inhibition of the luciferase enzyme by Isoflurane was reported [35,36]. It was previously suggested, that D-Luciferin inhibition by Isoflurane is a mixed style inhibition with competitive binding at the substrate binding site as well as a non-competitive binding changing the structure of the enzymatic pocket [37]. In line with previous reports, inhibition is partially reversible by higher substrate concentrations, which is due to an increased K_M value. Our data indicates that pre Isoflurane administration of D-Luciferin results in a better distribution of the substrate and hence in an increased availability of substrate in the brain compared to post Isoflurane injection. This may lead to an increased enzyme-substrate complex under pre-Iso condition, which is less affected by the inhibitory Isoflurane.

4. Imaging Protocol-dependent in vivo Detection Limits

We performed a quantitative comparison of the advanced vs. the standard imaging protocol applied to NSC^{Luc2+} transplanted into the mouse brain at different quantities. With this approach it was possible to study the detection limits of both protocols: 3,000 and 6,000 cells were not detectable with the standard protocol. Measuring these animals with the advanced protocol enables clear detection of even 3,000 transplanted NSCs (cf Fig. 6). To the best of our knowledge, such a small number of transplanted non-immortalized NSC has not been imaged in vivo before. We extracted SNR values for each graft size and determined that a SNR ≥ 3 can be used as a quantitative measure to reliably distinguish BLI signal from the noise. Visual comparison of all BL images ($n = 12$) confirmed that signals outside the cell graft exhibited SNR <3 and were identified as noise. Cell number estimation, as it was shown under in vitro conditions [38], seems to be possible in vivo providing that experimental conditions remain constant. High variability between animals receiving equal cell amounts was primarily induced by the transplantation procedure, which resulted in variations of cell number and transplantation depth, which strictly controls the percentage of transmitted bioluminescence light [39].

Conclusion

Optical brain imaging remains challenging for quantitative and sensitive approaches like the tracking of small number of transplanted cells. Here, we empirically determined a novel and efficient protocol with ip injection of 300 mg/kg pre to Isoflurane anesthesia. This novel protocol turned out to be twice as sensitive as the conventionally applied "standard protocol". Our quantitative analysis of the luciferase in vivo kinetics and the signal-to-noise ratio can serve as the basis of reliable detection limits for further studies.

Supporting Information

Figure S1 Background correction for ROI analysis of the DCX-Luc BLI data. a) Representative overlay of BLI data and a photograph of a mouse during BLI acquisition. ROIs mark the area of data analysis on the head (upper circle) and on the back of the animal. b) The background data were subtracted from the brain data resulting in a data set corrected for the difference in Luc expression and D-Luciferin distribution among the animals. Each color represents one individual DCX-Luc mouse.
(TIF)

Acknowledgments

We gratefully acknowledge Gabriele Schneider and Nadine Henn for excellent technical support.

Author Contributions

Conceived and designed the experiments: MA JA SCD MH. Performed the experiments: MA JA. Analyzed the data: MA JA SCD MH. Wrote the paper: MA JA SCD MH.

References

1. de Wet JR, Wood KV, DeLuca M, Helinski DR, Subramani S (1987) Firefly Luciferase Gene : Structure and Expression in Mammalian Cells. Molecular and Cellular Biology 7: 725–737. doi:10.1128/MCB.7.2.725.Updated.
2. Pichler A, Prior JL, Piwnica-Worms D (2004) Imaging reversal of multidrug resistance in living mice with bioluminescence: MDR1 P-glycoprotein transports coelenterazine. Proc Natl Acad Sci U S A 101 (6): 1702–1707. doi:10.1073/pnas.0304326101.
3. Kim J-B, Urban K, Cochran E, Lee S, Ang A, et al. (2010) Non-invasive detection of a small number of bioluminescent cancer cells in vivo. PloS one 5: e9364. doi:10.1371/journal.pone.0009364.
4. Keyaerts M, Remory I, Caveliers V, Breckpot K, Bos TJ, et al. (2012) Inhibition of firefly luciferase by general anesthetics: effect on in vitro and in vivo bioluminescence imaging. PloS one 7: e30061. doi:10.1371/journal.pone.0030061.
5. Inoue Y, Kiryu S, Izawa K, Watanabe M, Tojo A, et al. (2009) Comparison of subcutaneous and intraperitoneal injection of D-luciferin for in vivo bioluminescence imaging. European journal of nuclear medicine and molecular imaging 36: 771–779. doi:10.1007/s00259-008-1022-8.
6. Keyaerts M, Verschueren J, Bos TJ, Tchouate-Gainkam LO, Peleman C, et al. (2008) Dynamic bioluminescence imaging for quantitative tumour burden assessment using IV or IP administration of D: -luciferin: effect on intensity, time kinetics and repeatability of photon emission. European journal of nuclear medicine and molecular imaging 35: 999–1007. doi:10.1007/s00259-007-0664-2.
7. Lee K-H, Byun SS, Paik J-Y, Lee SY, Song SH, et al. (2003) Cell uptake and tissue distribution of radioiodine labelled D-luciferin: implications for luciferase based gene imaging. Nuclear medicine communications 24: 1003–1009. doi:10.1097/01.mnm.0000090431.24184.49.
8. Couillard-Despres S, Finkl R, Winner B, Ploetz S, Wiedermann D, et al. (2008) In vivo optical imaging of neurogenesis: watching new neurons in the intact brain. Molecular imaging 7: 28–34. doi:10.2310/7290.2008.0004.
9. Conti L, Pollard SM, Gorba T, Reitano E, Toselli M, et al. (2005) Niche-independent symmetrical self-renewal of a mammalian tissue stem cell. PLoS biology 3: e283. doi:10.1371/journal.pbio.0030283.
10. Doetschman TC, Eistetter H, Katz M, Schmidt W, Kemler R (1985) The in vitro development of blastocyst-derived embryonic stem cell lines: formation of visceral yolk sac, blood islands and myocardium. Journal of embryology and experimental morphology 87: 27–45.
11. Gissel C, Voolstra C, Doss MX, Koehler CI, Winkler J, et al. (2005) An optimized embryonic stem cell model for consistent gene expression and developmental studies A fundamental study. Thromb Haemost 94: 719–727. doi:10.1160/TH05.
12. Shagin DA, Barsova EV, Yanushevich YG, Fradkov AF, Lukyanov KA, et al. (2004) GFP-like proteins as ubiquitous metazoan superfamily: evolution of functional features and structural complexity. Molecular biology and evolution 21 (5): 841–850. doi:10.1093/molbev/msh079.
13. Morita S, Kojima T, Kitamura T (2000) Plat-E: an efficient and stable system for transient packaging of retroviruses. Gene Ther 7 (12): 1063–1066. doi:10.1038/sj.gt.3301206.
14. Keyaerts M, Caveliers V, Lahoutte T (2012) Bioluminescence imaging: looking beyond the light. Trends in molecular medicine 18: 164–172. doi:10.1016/j.molmed.2012.01.005.
15. Gerbino PP (2005) Drug Absorption and Disposition. In: Troy DB (ed) Remington: The Science and Practice of Pharmacy. Lippincott Williams & Wilkins.
16. Pendharkar AV, Chua JY, Andres RH, Wang N, Gaeta X, et al. (2010) Biodistribution of neural stem cells after intravascular therapy for hypoxic-ischemia. Stroke; a journal of cerebral circulation 41: 2064–2070. doi:10.1161/STROKEAHA.109.575993.
17. Sher F, van Dam G, Boddeke E, Copray S (2009) Bioluminescence imaging of Olig2-neural stem cells reveals improved engraftment in a demyelination mouse model. Stem cells (Dayton, Ohio) 27: 1582–1591. doi:10.1002/stem.76.
18. Tang Y, Shah K, Messerli SM, Snyder E, Breakefield X, et al. (2003) In vivo tracking of neural progenitor cell migration to glioblastomas. Human gene therapy 14: 1247–1254. doi:10.1089/104303403767740786.
19. Sutton EJ, Henning TD, Pichler BJ, Bremer C, Daldrup-Link HE (2008) Cell tracking with optical imaging. European radiology 18 (10): 2021–2032. doi:10.1007/s00330-008-0984-z.
20. Ignowski JM, Schaffer DV (2004) Kinetic analysis and modeling of firefly luciferase as a quantitative reporter gene in live mammalian cells. Biotechnology and bioengineering 86: 827–834. doi:10.1002/bit.20059.
21. Contag CH, Spilman SD, Contag PR, Oshiro M, Eames B, et al. (1997) Visualizing Gene Expression in Living Mammals Using a Bioluminescent Reporter. Photochemistry and Photobiology 66: 523–531. doi:10.1111/j.1751-1097.1997.tb03184.x.
22. Berger F, Paulmurugan R, Bhaumik S, Gambhir SS (2008) Uptake kinetics and biodistribution of 14C-D-luciferin–a radiolabeled substrate for the firefly luciferase catalyzed bioluminescence reaction: impact on bioluminescence based reporter gene imaging. European journal of nuclear medicine and molecular imaging 35: 2275–2285. doi:10.1007/s00259-008-0870-6.
23. Lembert N, Idahl La (1995) Regulatory effects of ATP and luciferin on firefly luciferase activity. The Biochemical journal 305 (Pt 3: 929–933.
24. Choy G, O'Connor S, Diehn FE, Costouros N, Alexander HR, et al. (2003) Comparison of noninvasive fluorescent and bioluminescent small animal optical imaging. BioTechniques 35: 1022–1026, 1028–1030.
25. Edinger M, Cao Y-a, Hornig YS, Jenkins DE, Verneris MR, et al. (2002) Advancing animal models of neoplasia through in vivo bioluminescence imaging. European Journal of Cancer 38: 2128–2136.
26. Hasan MT, Schönig K, Berger S, Graewe W, Bujard H (2001) Long-term, noninvasive imaging of regulated gene expression in living mice. Genesis New York NY 2000 29: 116–122. doi:10.1002/gene.1014.
27. Luker GD, Bardill JP, Prior JL, Pica CM, Piwnica-Worms D, et al. (2002) Noninvasive Bioluminescence Imaging of Herpes Simplex Virus Type 1 Infection and Therapy in Living Mice. Journal of Virology 76: 12149–12161.
28. Lipshutz GS, Gruber CA, Y C, Hardy J, Contag CH, Gaensler KM (2001) In utero delivery of adeno-associated viral vectors: intraperitoneal gene transfer produces long-term expression. Molecular therapy the journal of the American Society of Gene Therapy 3: 284–292.
29. Rehemtulla A, Stegman LD, Cardozo SJ, Gupta S, Hall DE, et al. (2000) Rapid and quantitative assessment of cancer treatment response using in vivo bioluminescence imaging. Neoplasia (New York, NY) 2: 491–495.
30. Wang W, El-Deiry WS (2012) Bioluminescent molecular imaging of endogenous and exogenous p53-mediated transcription in vitro and in vivo using an HCT116 human colon carcinoma xenograft model. Cancer biology & therapy 2: 196–202. doi:10.2144/000113917.
31. Pawson P, Forsyth S (2008) Chapter 5 - Anesthetic agents. Small Animal Clinical Pharmacology. W.B. Saunders, Edinburgh.
32. Janssen BJa, De Celle T, Debets JJM, Brouns AE, Callahan MF, et al. (2004) Effects of anesthetics on systemic hemodynamics in mice. American journal of physiology Heart and circulatory physiology 287: H1618–1624. doi:10.1152/ajpheart.01192.2003.
33. Zuurbier CJ, Emons VM, Ince C (2002) Hemodynamics of anesthetized ventilated mouse models: aspects of anesthetics, fluid support, and strain. American journal of physiology Heart and circulatory physiology 282: H2099–2105. doi:10.1152/ajpheart.01002.2001.
34. Hildebrandt IJ, Su H, Weber Wa (2008) Anesthesia and other considerations for in vivo imaging of small animals. ILAR journal/National Research Council, Institute of Laboratory Animal Resources 49: 17–26.

35. Franks NP, Jenkins A, Conti E, Lieb WR, Brick P (1998) Structural basis for the inhibition of firefly luciferase by a general anesthetic. Biophysical journal 75: 2205–2211. doi:10.1016/S0006-3495(98)77664-7.
36. Szarecka A, Xu Y, Tang P (2007) Dynamics of firefly luciferase inhibition by general anesthetics: Gaussian and anisotropic network analyses. Biophysical journal 93: 1895–1905. doi:10.1529/biophysj.106.102780.
37. Leitão JMM, Esteves da Silva JCG (2010) Firefly luciferase inhibition. Journal of photochemistry and photobiology B, Biology 101: 1–8. doi:10.1016/j.jphotobiol.2010.06.015.
38. Nguyen VT, Morgange M, Bensaude O (1988) Firefly Luciferase Luminescence Assays Using Scintillation Counters Quantitation in Transfected Mammalian Cells. Analytical biochemistry 171: 404–408.
39. Pesnel S, Pillon A, Créancier L, Guilbaud N, Bailly C, et al. (2011) Quantitation in bioluminescence imaging by correction of tissue absorption for experimental oncology. Molecular imaging and biology : MIB : the official publication of the Academy of Molecular Imaging 13: 646–652. doi:10.1007/s11307-010-0387-9.

IV.

High field BOLD response to forepaw stimulation in the mouse.

Joanna M. Adamczak, Tracy D. Farr, Jörg Seehafer, Daniel Kalthoff and Mathias Hoehn
NeuroImage (2010). 51(2): 704-712

NeuroImage 51 (2010) 704–712

Contents lists available at ScienceDirect

NeuroImage

journal homepage: www.elsevier.com/locate/ynimg

High field BOLD response to forepaw stimulation in the mouse

Joanna M. Adamczak, Tracy D. Farr, Jörg U. Seehafer, Daniel Kalthoff, Mathias Hoehn *

In-vivo-NMR Laboratory, Max Planck Institute for Neurological Research, Cologne, Germany

ARTICLE INFO

Article history:
Received 28 December 2009
Revised 11 February 2010
Accepted 28 February 2010
Available online 6 March 2010

Keywords:
fMRI
BOLD
Forepaw stimulation
Mouse
High field MRI
Somatosensory evoked potentials
Medetomidine anesthesia

ABSTRACT

We have established a robust protocol for longitudinal fMRI in mice at high field MRI using a medetomidine anesthesia. Electrical forepaw stimulation in anesthetized animals is widely used to produce BOLD contrast in the primary somatosensory cortex. To preserve neuronal activity, most fMRI experiments used α-chloralose to produce sedation, but severe side effects make this procedure unsuitable for survival experiments. As advantageous alternative, the α_2-adrenergic receptor agonist medetomidine has been applied successfully to permit longitudinal fMRI studies in rats. With the advent of transgenic technology, mouse models have become increasingly attractive raising the demand for implementation of a suitable fMRI protocol for mice. Therefore, we investigated the use of medetomidine for repetitive fMRI experiments in C57BL/6 mice. We evaluated the optimal medetomidine dose for subcutaneous application. Somatosensory evoked potentials (SSEPs) in the contralateral somatosensory cortex were recorded to assess brain activity under medetominidine following forepaw stimulation. Repetitive administration of medetomidine, the requirement for longitudinal brain activation studies, was well tolerated. Using the forepaw stimulation paradigm, we observed BOLD contrast in the contralateral somatosensory cortex in ~50% of the performed scans using gradient echo-echo planar imaging (GE-EPI). However, imaging the small mouse brain at high field strength is challenging and we observed strong susceptibility artifacts in GE-EPI images in the cortex. We have developed an agar gel cap for successful compensation of these artifacts as prerequisite for successful mouse fMRI at 11.7T. The established protocol will be suitable for brain activation studies in transgenic animals and for studies of functional deficit and recovery after brain injury in mice.

Introduction

Functional magnetic resonance imaging (fMRI) using endogenous blood-oxygenation-level-dependent (BOLD) contrast (Ogawa et al., 1990) is a widely used technique to study brain activity non-invasively. Neuronal activation increases local energy demands and O_2 consumption, which leads to a shift in the relative concentration of oxygenated and deoxygenated haemoglobin in the capillary bed. This produces a susceptibility difference, which is the basis of BOLD imaging. The most common fMRI paradigm in rodents requires electrical stimulation of the fore- or hindlimbs to produce BOLD contrast in the corresponding regions of the primary somatosensory (S1) cortex (Bock et al., 1998). For this purpose, most studies employ α-chloralose to produce sedation and preserve neuronal activity (Ueki et al., 1992). However, these experiments are acute protocols (Silverman and Muir, 1993) and as such, alternative protocols have been established to perform longitudinal and non-invasive fMRI. Recently, the use of the α_2-adrenergic receptor agonist medetomidine was introduced as an anesthetic for fMRI (Weber et al., 2006) and is now being used frequently in fMRI studies in the rat (Pawela et al., 2008; Weber et al., 2008; Zhao et al., 2008). Medetomidine produces sedation, analgesia and muscle relaxation by binding to central α_2-adrenoreceptors located primarily in the brainstem (Ruffolo and Hieble, 1994). It decreases the release of noradrenalin, thereby causing a general inhibition of the sympathetic nervous system (Sinclair, 2003).

Up to now, it has been difficult to perform fMRI in mice. One reason for this is that it is extremely challenging to maintain tight control over physiological parameters in the mouse. Another reason is that the small neuroanatomical functional unit of the mouse requires high field strength to be resolved. Furthermore, the small mouse head leads to stronger susceptibility artifacts in GE-EPI with increasing field strength causing signal loss in the prominent brain structures of interest. To date, very few studies have attempted fMRI in the mouse. The first of which employed the classical α-chloralose paradigm and hindlimb stimulation combined with a gradient echo fast low angle shot (FLASH) sequence at 11.7 Tesla (T) (Ahrens and Dubowitz, 2001). They reported a 7% BOLD change in the somatosensory cortex, which was even higher in the draining veins. Subsequent studies employed low levels of isoflurane and intravenous contrast agent to measure changes in cerebral blood volume (CBV) at 7 T following hindpaw stimulation (Mueggler et al., 2001), or BOLD change at 9.4 T with spin echo-echo planar imaging (SE-EPI) (Nair and Duong, 2004). In these studies, electrical stimulation of the hindpaws ranged up to 6 mA, which is quite high but was required, most likely because isoflurane

* Corresponding author. In-vivo-NMR-Laboratory, Max Planck Institute for Neurological Research, Gleuelerstrasse 50, D-50931 Köln, Germany. Fax: +49 221 4726 337.
E-mail address: mathias@nf.mpg.de (M. Hoehn).

1053-8119/$ – see front matter © 2010 Elsevier Inc. All rights reserved.
doi:10.1016/j.neuroimage.2010.02.083

strongly suppresses neural activity. Therefore, the present study was designed to investigate the feasibility of establishing the medetomidine protocol, already proven very successful in rats, to produce sedation in mice for the purpose of fMRI. It was the goal to establish a robust protocol suitable for longitudinal brain activation studies in mice.

Materials and methods

Animals

Animal experiments were performed in accordance with the German Laws for Animal Protection and were approved by the local animal care committee and governmental body (Bezirksregierung Köln). Twenty-nine adult male C57BL/6 mice (20–35 g body weight) were used. Animals were housed individually at a 12/12 h light/dark cycle and had *ad libitum* access to water and standard diet.

Anesthesia

All animals were initially anesthetized with 4% isoflurane in O_2:N_2O (30:70). Isoflurane was reduced to 1.5% for maintenance during preparation. Isoflurane was required during preparation primarily to prevent the pain response to insertion of the infusion needle, insertion of the stimulation electrodes, and scalp incision for the SSEP procedure. Body temperature was continuously monitored with a rectal probe and maintained at 37.0 ± 0.5 °C with in-house feedback controlled water or electrical blankets. Respiration rate was continuously monitored using a pressure sensitive pad and DASYLab software (National Instruments, Austin, TX, USA). When respiration was stable at 110–130 breaths per min, animals received a subcutaneous bolus of medetomidine (Domitor®, Pfizer, Karlsruhe, Germany) through a 23 Gauge (G) needle placed into the back that was connected to a 0.58 mm inner diameter polythene tubing, and administered via a syringe pump (Kent Scientific Corporation, Torrington, USA) outside the magnet room. Isoflurane was slowly discontinued over the course of the next 10 min (by approximately 0.2% every 1 min starting 3 min after bolus administration) so that no isoflurane was available at 10 min after bolus administration. When respiration rate decreased more than 50 bpm in the first 3 min after bolus administration, isoflurane was discontinued faster. At the time point of 10 min after bolus administration, a subcutaneous infusion of medetomidine was started and the N_2O in the inhalation gas was replaced by N_2. At the end of the experiment, mice received an intraperitoneal injection of atipamezole (Antisedan®, Pfitzer) at five times the initial dose of medetomidine in order to reverse the effects.

Experimental design

The first objective was the evaluation of the optimal dose of medetomidine for mice. Theoretically, the optimal dose would provide sufficient sedation for a maximum period of time and allow for full recovery after the experiment was concluded. The second objective was to establish whether neuronal activity was preserved following medetomidine sedation with the optimized dose. This was accomplished by recording somatosensory evoked potentials (SSEPs) during forepaw stimulation. The third objective was to optimize MR image quality using a combination of shimming techniques and home-developed agar gel head caps (cf. below). The fourth objective was to perform serial fMRI measurements in the same mice using an identical forepaw stimulation paradigm, thus proving the protocol suitability for longitudinal functional studies.

Dose response

Six different doses of medetomidine (bolus: 0.2, 0.3, 0.4, 0.5, 0.6, and 0.7 mg/kg; and corresponding infusion: 0.4, 0.6, 0.8, 1.0, 1.2, 1.4 mg/kg/h respectively; $n = 2$ each) were tested in 12 mice. Sedation duration (i.e. time between bolus administration and the time when the animal woke up), respiration rate and recovery were monitored for each dose. Additionally, trend of partial pressure of carbon dioxide (pCO_2) was monitored with a transcutaneous blood gas analyzer (TCM4, Radiometer Copenhagen) optimized for rodent recordings. For this, a 2 cm circle of fur was removed from the abdomen with an electrical razor and depilatory cream, and an electrode was secured with a fixation ring and contact fluid. Once sedation became light and animals began to move, they received the corresponding dose of atipamezole (1.0, 1.5, 2.0, 2.5, 3.0, and 3.5 mg/kg) and were returned to their home cages.

SSEP recording

Somatosensory evoked potentials were recorded in mice ($n = 5$) sedated with 0.3 mg/kg medetomidine, which was determined as the optimal dose from the dose response experiments. Animals were originally anesthetized with isoflurane and positioned in a stereotaxic apparatus. The skin over the skull was retracted and custom-built silverball electrodes were placed over the left and right S1 cortices (2.4 mm lateral from bregma) with conducting gel. Home-built steel needle (30 G) electrodes were placed subcutaneously into both forepaws. Once preparation was complete, medetomidine sedation was initiated. Stimulation was performed with 100 rectangular pulses (2 mA, 6 Hz, 0.3 ms; STG 1004 Stimulator, Multi Channel Systems, Reutlingen, Germany). Each paw was stimulated 4 times with random sequencing between the paws. The response was recorded and averaged with DasyLab software so that one evoked potential was obtained per stimulation period. At the conclusion of the experiments, low doses of isoflurane (0.8–1%) were administered in order to suture the wound, and local anesthetic (Xylocain Gel 2%, AstraZeneca, Wedel, Germany) was applied to minimize pain. Animals were subsequently recovered with 1.5 mg/kg of atipamezole and returned to their home cages.

MRI

MRI experiments were conducted at a horizontal 11.7T Biospec system (Bruker BioSpin, Ettlingen, Germany) with a 16 cm diameter bore magnet and using ParaVision 5 software. RF transmission was achieved with a quadrature resonator (Bruker) and the signal was detected using a mouse quadrature surface coil (Bruker). Animals were mounted in an animal holder (Bruker) using a toothbar and earbars for stable positioning. Body core temperature was controlled and monitored with an in-house designed automated temperature control unit complete with water blanket.

Image quality experiments

Single shot gradient echo-echo planar imaging (GE-EPI) was employed on two mice using the following imaging parameters: TE approximately equal to the T_2^* value of the cortex (17.5 ms), TR = 3000 ms, BW = 150 kHz, 1 mm slice thickness, field of view = 1.28 × 1.28 mm^2, matrix 64 × 64 pixels. Microscopic field gradients at interfaces of air, bone and brain resulted in signal loss artifacts in the S1 cortex. Therefore, different shim methods were used to improve image quality: global shim, local shim and field map-based shimming (MAPSHIM, ParaVision 5). The field map, a 3D volume of the B0 field distribution, was acquired with TE = 2 ms, TR = 20 ms, and isotropic resolution of (150 µm)^3. The shim volume for all shim methods was a (4 mm)^3 cube positioned in the mouse brain including the S1 cortex. As no improvement of image quality was visible, field maps were acquired after each shim method in order to visualize the field line distributions. Additionally, field maps were acquired for different positions of the S1 relative to the isocenter (−4, −2, 0, 2, and 4 mm along the z-axis) to locate the origin of distortions. Finally, in

order to reduce field inhomogeneity, a 2% agarose gel was molded into a head cap and introduced between the head and surface coil, which was followed by shimming and acquisition of field maps. The shape of the head cap was a half moon. It was made by pouring liquid agarose into a plastic tube of 2 cm diameter that had been sliced in half lengthwise. A second tube (1.6 cm diameter) was then placed on top of the hardening gel. In general, the thickness of the caps ranged at the most caudal part being 0.5–1 mm thick and the most rostral part being 1–1.5 mm thick. The cap was 1.5 cm long and as wide as the surface coil.

fMRI

Following optimization, 10 animals were employed to assess protocol suitability for repetitive fMRI sessions. All 10 mice were scanned twice (with 3 weeks interval between sessions) and 5 of them received a third session after another 3 weeks rest. Anesthesia preparation was performed as described above with the evaluated medetomidine dose: an initial 0.3 mg/kg bolus followed by a 0.6 mg/kg/h subcutaneous infusion. Following positioning, local shim was performed using a $(4\ \text{mm})^3$ cube positioned in the brain, including the S1. Field maps were then acquired and used to perform MAP-Shim with the same cube volume. GE-EPI was performed as described above (cf. Image quality experiments) with 5 consecutive (1 mm thin) coronal slices with the central slice positioned in the center of the S1 (3.5 mm caudal to the rhinal fissure). Forepaw stimulation was performed with the above described parameters (cf. *SSEP recording*) in a paradigm that employed 140 repetitions, consisting of 5 blocks. Each block consisted of a 45 s resting period and a 30 s activation period. The fMRI scan ended with an additional 45 s resting period, which resulted in a total scan time of 7 min. Animals were allowed to rest for 5 min between fMRI scans. The number of fMRI scans per paw varied between 4 (long sedation) and 2 (short sedation) and was randomized between left and right paw. An additional GE-EPI scan with 60 repetitions but no stimulation was included in order to determine temporal signal-to-noise ratio (tSNR).

Image analysis

Temporal signal-to-noise ratio (tSNR) was calculated voxelwise using ImageJ software (Rasband, 1997–2009), by dividing the mean signal intensity of the 60 individual images by its standard deviation over time. Subsequently, circular regions of interest (ROIs) of 25 pixels from each, the left and right forepaw representation in the somatosensory cortex, were averaged to obtain one representative tSNR value for each animal per session.

T2* values were acquired from 5 coronal slices (1 mm slice thickness, 128×128 pixel matrix, 1.28 cm × 1.28 cm field of view, 30° flip angle) during resting phases in between fMRI scans, using a multi-gradient-echo sequence (MGE) with 10 echoes ranging from 5 to 50 ms and a TR of 2500 ms. T2* maps were calculated using ImageJ software and average T2* values were obtained from two regions of interest (circles of 104 pixels) from the left and right primary somatosensory cortex of the central slice through the S1.

Statistical analysis was performed with STIMULATE software (Strupp, 1996) using a pixel by pixel paired Student´s *t*-test and a 95% confidence level. The largest cluster of activated pixels of the central image slice was taken for further analysis. The number of activated pixels was counted and the percentage signal change of each pixel was averaged into a mean percent BOLD change for the cluster.

Results

Repetitive medetomidine sedation was well tolerated by mice. Most animals recovered to a normal activity level within 2 min after atipamezole administration. One animal was lost during the second fMRI experiment due to experimental error. Following the third administration of medetomidine, 2 of the 5 mice died within 4 h after what appeared to have been a normal recovery.

Dose response

Maximal sedation length during the dose response study performed on 12 mice on the bench was around 90 min (Fig. 1A). Mice which received an initial bolus of 0.3 mg/kg in combination with an continuous infusion of 0.6 mg/kg/h remained sedated for 67 and 62 min while sedation was 93 and 82 min with an initial bolus of 0.4 mg/kg combined with an infusion of 0.8 mg/kg/h. Animals sedated with doses ranging from 0.5 to 0.7 mg/kg (infusion 1.0 to 1.4 mg/kg/h, respectively) exhibited variable sedation lengths, and particularly with the highest dose, recovered slower and exhibited adverse behavior such as hunching and lethargy during 24 h post sedation. Therefore, three animals were euthanized and doses equal to or higher than 0.5 mg/kg were subsequently excluded. Although a bolus dose of 0.4 mg/kg combined with a subsequent infusion of 0.8 mg/kg/h resulted in longest sedation periods, we decided to use a dose of 0.3 mg/kg in combination with a continuous infusion of 0.6 mg/kg/h for functional MRI studies. This decision was based primarily on the fact that the sedation length was more similar in the animals that received the lower of the 2 doses, as well as for safety considerations since already the dose of 0.5 mg/kg with an infusion of 1.0 mg/kg led to unwanted side effects.

In 4 of the 6 animals treated with 0.2–0.4 mg/kg (0.4–0.8 mg/kg/h infusion respectively), a slight decrease in respiration rate (around 20 breaths/min) was observed between 1 and 5 min after the medetomidine bolus (Fig. 1C). When isoflurane was discontinued, all animals showed an increase in respiratory rate, which stabilized approximately 20 min after the initial medetomidine bolus. The respiration rate for mice sedated with medetomidine was between 160 and 200 breaths/min. In all animals, transcutaneous pCO_2 showed an initial increase upon medetomidine administration which stabilized after 15 min (Fig. 1D).

SSEP recording

Investigation of electrophysiological behavior under medetomidine was carried out on 5 animals sedated with 0.3 mg/kg. SSEPs were consistently recorded in the contralateral hemisphere following all 4 stimulations of each forepaw. Average SSEP waveforms for each of the 5 mice are depicted in Fig. 1B. The SSEPs exhibited the standard peaks P1, N1 and P2 with average amplitudes of 148.8 ± 110.6, -135.8 ± 124.3, and 5.1 ± 25.4 μV, and average latencies of 20.4 ± 1.0, 28.9 ± 1.3, and 37.1 ± 4.8 ms, respectively, as summarized in Table 1.

Image quality experiments

The small mouse brain makes shimming difficult, and image distortions were prevalent. This was particularly so in regions of tissue interface changes, such as the cortex, and therefore, there was often loss of signal in the S1. Several strategies were employed to investigate this situation. Field maps of the brain were acquired for different positions of the S1 relative to the isocenter of the magnet along the *z*-axis (Fig. 2A). Magnetic field inhomogeneities were located in the olfactory bulbs and posterior half of the brain. This was found to be independent of animal position relative to the isocenter. Therefore, different shim strategies were employed, including Global Shim, Local Shim and MAPSHIM, but none succeeded alone or in combination in recovering the lost signal in the S1 (Fig. 2B–C). However, the introduction of an agar head cap between the head and surface coil (Fig. 2F), substantially improving the susceptibility homogeneity across the mouse head volume, significantly improved the image quality (Fig. 2D–E), even before shimming. Homogeneity

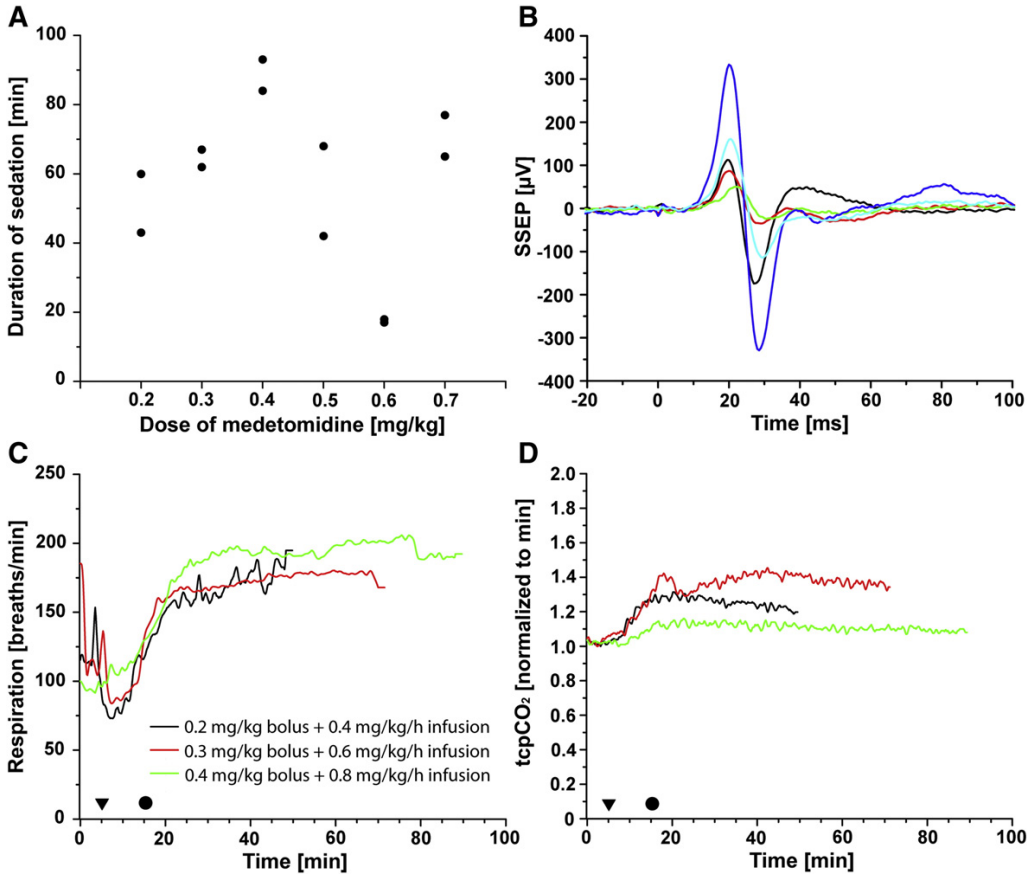

Fig. 1. The effects of medetomidine on sedation duration, SSEP recording, respiration rate and transcutaneous CO_2. (A) Sedation length in response to different doses of medetomidine. The longest sedation was achieved with 0.4 mg/kg while doses between 0.5 and 0.7 mg/kg were more variable, but also resulted in unwanted side effects. (B) Somatosensory evoked potentials for 5 mice (represented by different colors), sedated with 0.3 mg/kg of medetomidine. Each line represents the average of 8 evoked potentials recorded from one mouse following electrical forepaw stimulation. Representative respiration rates (C) and transcutaneous CO_2 ($tcpCO_2$) (D) for three different animals that received different doses of medetomidine during the dose response experiments. (▼) Time of bolus administration; (●) time of complete isoflurane discontinuation and beginning of continuous infusion.

drastically improved at the level of the eyes, as well in the posterior half of the brain (Fig. 2E). However, following shimming on the $(4\ mm)^3$ shim volume, geometric distortions appeared in the lower brain parts with varying intensity.

fMRI

The 10 mice that underwent fMRI experiments exhibited slightly longer sedation periods (112 ± 21 min, $n = 24$ anesthesia sessions) with 0.3 mg/kg medetomidine than was earlier observed during the dose response experiments. Sedation length varied between the animals, and therefore also the number of performed scans per session varied between 4 and 8 (Table 2). Following the stimulation of each forepaw, BOLD activation was detected in the contralateral S1 in approximately 50% of the performed scans (Table 2). Despite this somewhat variable situation from scan to scan, we reproduced the BOLD response between two independent sessions in 6 animals (Fig. 3C–H).

Results for all 10 mice over both fMRI sessions are summarized in Table 2. Overall, during the first fMRI session, a significant BOLD response was detected in 8 of the 10 mice (Table 2). One of these eight animals died during the second session, and of the remaining seven mice, six showed a BOLD response during the second session (Fig. 3C–H). The remaining two animals that did not show BOLD response during the first session did, however, exhibit a strong response during the second session (Table 2). Despite the overall trend, there was some variability of BOLD detection between individual scans in some animals. BOLD was detected in every scan in 2 animals during the first session (Table 2: Animals 4 + 8). However, in some animals, especially during the second session, only one BOLD positive scan was observed per session (Table 2: Animals 2, 6, 7, 9, and 10). BOLD prevalence from the first session across all animals was 30 BOLD positive scans out of 52 performed scans (57.7%). Following the second session, prevalence decreased to 45 positive scans out of 105 performed scans (42.9%). The average increase in the BOLD signal fluctuated around 1% with the

Table 1
Average SSEP peak latency and amplitude recorded during forepaw stimulation over the S1 from medetomidine anesthetized mice.

Animal #	Latency P1 (ms)	Latency N1 (ms)	Amplitude P1 (μV)	Amplitude N1 (μV)
1	19.9 ± 0.7	27.9 ± 1.2	119.9 ± 47.0	-184.4 ± 107.0
2	20.0 ± 0.7	29.7 ± 2.4	90.0 ± 28.7	-42.9 ± 25.7
3	22.1 ± 1.9	32.4 ± 4.2	56.3 ± 7.5	-34.0 ± 13.8
4	20.4 ± 0.7	28.8 ± 1.3	336.8 ± 403.0	-322.8 ± 427.6
5	20.6 ± 0.6	30.0 ± 1.2	161.0 ± 117.5	-110.25 ± 115.4
Average	20.6 ± 1.1	29.8 ± 1.9	152.8 ± 109.8	-140.9 ± 123.2

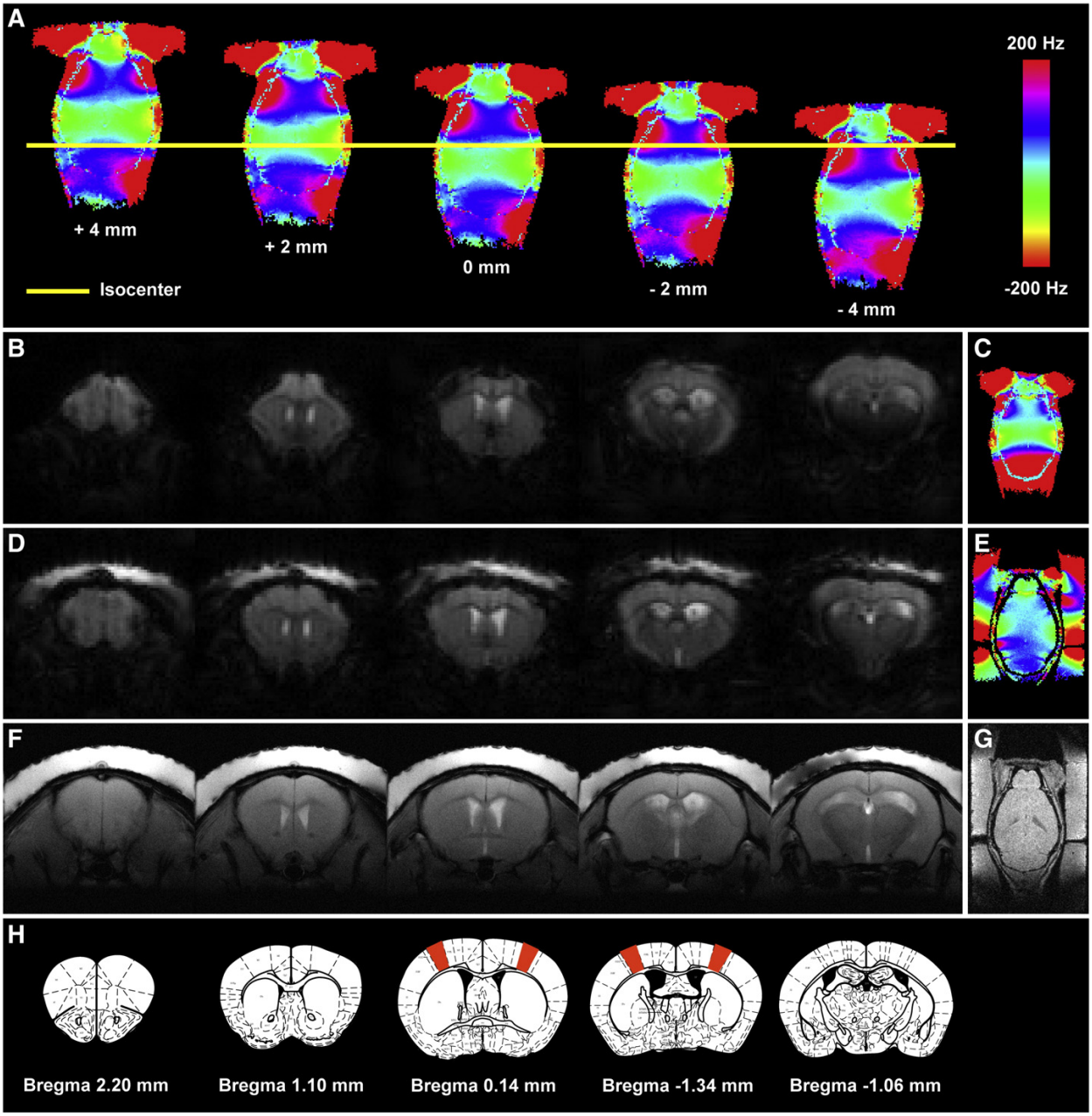

Fig. 2. Evaluation of image quality. (A) Field maps for different positions of the S1 relative to the isocenter along the *z*-axis. Note that inhomogeneities were present in rostral brain regions independent of animal position. (B, C) GE-EPI images and corresponding field map of an animal following shimming procedures. Note the signal loss from the cortex. (D, E) GE-EPI images and corresponding field map of an animal with an agar gel cap between the head and surface coil. Note the retained signal in the cortices and substantial improvement of homogeneity in the field map. (F, G) Coronal and horizontal anatomical FLASH images from an animal with the agar gel cap, and (H) corresponding schematics of coronal brain slices with S1 cortices highlighted in orange. Note in panel (G): The break of the gel (black lines) on both sides of the brain indicates the location of the ear bars for head fixation.

overall average over both sessions of $1.3 \pm 0.4\%$. The average number of BOLD positive pixels in the center slice varied from 5 to 13, with an overall average of 7.4 ± 4.4 pixels (Table 2). As can be seen in Fig. 3B + I–K, spontaneous fluctuations of the signal challenge the easy monitoring of the fMRI signal. Especially, BOLD signal peaks were not sustained over the period of stimulation. Nevertheless, average signal increase during stimulation periods was significant at a confidence level of 95%.

Temporal SNR was subject to some variation between sessions. All 10 mice showed a good and stable temporal SNR of 48 ± 6 during the first session, which decreased, however, during the second session to 39 ± 11. Specifically, the first 4 animals of the second session had a good tSNR of 50 ± 6, while the 5 last scanned mice had a tSNR of 27 ± 4. However, the detectability of the BOLD response did not appear to be dependent on tSNR, since no correlation was found between the total number of activated pixels weighted by the number of performed scans of one session and the tSNR value ($R^2 = 0.07$). Nevertheless, the 5 mice with the lowest tSNR (around 27) during the second session underwent a third fMRI session. tSNR was significantly improved to 41 ± 7 during

Table 2
BOLD success rate for all 10 animals undergoing two separate fMRI sessions.

Animal	Session 1			Session 2		
	BOLD positive scans/ total no. of scans	Average no. of activated pixels of central slice ± standard deviation	Mean BOLD change ± standard deviation	BOLD positive scans/ total no. of scans	Average no. of activated pixels of middle slice ± standard deviation	Mean BOLD change ± standard deviation
1	3/6	8.0 ± 2.6	1.5 ± 0.4	5/7	6.4 ± 2.6	1.2 ± 0.3
2	2/6	5.0 ± 3.8	1.4 ± 0.4	1/4	6	0.8
3	2/3	11.5 ± 2.1	1.2 ± 0.5	2/4	11.5 ± 9.2	0.9 ± 0.1
4	6/6	13.3 ± 6.4	1.4 ± 0.2	–*	–*	–*
5	3/6	9.7 ± 4.9	1.5 ± 0.4	3/8	5.3 ± 1.5	1.0 ± 0.1
6	6/6	7.8 ± 3.5	0.9 ± 0.2	1/8	7	1.4
7	0/4	–	–	1/5	4	1.8
8	4/4	12.8 ± 6.4	0.9 ± 0.2	0/4	–	–
9	0/5	–	–	1/6	10	1.9
10	4/6	8.5 ± 2.4	1.3 ± 0.3	1/7	9	1.3
Average	(Sum)30/52	9.7 ± 5.5	1.3 ± 0.4	(Sum)15/53	6.3 ± 2.2	1.2 ± 0.4
Average over both sessions		7.9 ± 4.4	1.3 ± 0.4			

– indicates no BOLD change observed. * indicates no measurement obtained due to earlier death of the animal.

the third session. The average BOLD response was comparable to the previous sessions (1.4 ± 0.3% signal increase) with an average of 10.8 ± 6.5 activated pixels. Total BOLD outcome of all three sessions was 53 BOLD positive scans from 131 performed scans (40.5%).

T2* values for the left and right somatosensory cortex varied between 10 and 23 ms. The overall average of the T2* value was 18.0 ± 3.5 ms.

Discussion

In the present study, we have established a longitudinal and non-invasive protocol for fMRI of the somatosensory cortex of mice. Medetomidine, an α_2-adrenoreceptor agonist, was used to achieve sedation. Following evaluation of the optimal dose of 0.3 mg/kg, the sedation was characterized by a stable respiration rate and transcutaneous CO_2 level. Somatosensory evoked potentials (SSEPs) were recorded during electrical forepaw stimulation from the contralateral S1 in medetomidine sedated mice and subsequent BOLD change was observed longitudinally in 6 of 9 mice, which underwent longitudinal fMRI. The BOLD response was specific to the stimulus, showing the largest cluster of activated pixels in the S1 cortex contralateral to the stimulated forepaw. This protocol will allow for the first time access to the investigation of functional brain activation changes in different transgenic mouse models. Furthermore, it will help to elucidate mechanisms of functional brain deficit and recovery, respectively, in mice having undergone brain injury such as e.g. stroke and stem cell therapy.

Somatosensory evoked potentials showed the well established shape of a fast positive deflection (P1) followed by a fast negative deflection (N1) and a second positive wave (P2), which is consistent with literature for rodent SSEPs (Brinker et al., 1999; Franceschini et al., 2008; Gsell et al., 2006). The amplitude of P1 and N1 is in good agreement with previously recorded SSEPs from the S1 cortex in mice, P1 = 51.3 ± 6.4 μV, N1 = −93.6 ± 11 μV (Troncoso et al., 2000). In the present study, the average amplitudes varied in the range of 56 to 336 μV for P1 and from −34 to −332 μV for N1 between individual animals. Also the ratio of P1 to N1 amplitude is subject of variation, and mostly P1 is larger than N1. This is different than previously observed in α-chloralose anesthetized rats. We cannot exclude that a sedation effect may contribute to the amplitude differences and ratio variations among animals, but it can also be influenced by small differences in electrode position, as well as contact quality. Furthermore, Troncoso et al. proposed light anesthesia as a confounding factor in SSEP recordings, resulting in decreased SNR due to cortical desynchronization (Troncoso et al., 2000), which may also have contributed to the observed variation in the ratio of P1 to N1 amplitude. However, it is noteworthy that Hayton et al. (1999), in earlier studies of SSEPs of rats under medetomidine, reported P1/N1 amplitude ratios very much in line with our present results. These authors argued that medetomidine as an α2 adrenergic receptor agonist disrupts the signal transduction from thalamus to cortex and therefore more synapses have to be passed in order to generate cortical components. Latencies for P1 and N1 were extremely stable (20.6 ± 1.1 ms and 29.8 ± 1.9 ms, respectively), although they are somewhat longer than what has been observed previously: (14 ± 0.6 ms and 24 ± 1.1 ms) (Troncoso et al., 2000). One possible explanation for this is that Troncoso et al. used pentobarbital to produce anesthesia, and different anesthetic agents have been shown to produce different effects on both the latencies and amplitudes of SSEPs (Hayton et al., 1999). Furthermore, it has been shown that the optimal frequency of the forepaw stimulation can be different depending on the anesthetic agent. For example, a frequency of 1.5–3 Hz resulted in the largest amplitude SSEP recordings in α-chloralose anesthetized rats (Brinker et al., 1999; Silva et al., 1999), whereas this was reported to be 8–12 Hz for isoflurane anesthetized rats (Masamoto et al., 2007). We used a frequency of 6 Hz because the BOLD response under medetomidine sedation was shown to be maximal in the range between 6 and 9 Hz in rats (Zhao et al., 2008). While no other frequencies were tested in our hands, the results show that stable SSEPs can be obtained with the selected 0.3 mg/kg medetomidine dose.

A BOLD response was observed (53/131 scans) using our sedation strategy with a mean signal change around 1.3 ± 0.4%. This is comparable to other studies that employed isoflurane and similar stimulation parameters (2 mA, 0.3 ms pulse width, but 3 Hz instead of 6 Hz) at 9.4 T (Nair and Duong, 2004). A higher BOLD response was produced to around 3% by increasing the stimulation current to 6 mA while decreasing the isoflurane concentration to 0.75% (Nair and Duong, 2004). However, irregular respiration patterns and changes in mean arterial blood pressure (MABP) were reported when stimulation was increased to 7 mA, suggesting a non-specific BOLD effect already at 6 mA due to a contribution of pain response. Also in isoflurane anesthetized rats, a current of minimum 6 mA was reported necessary to result in a BOLD increase of approximately 1% (Liu et al., 2004). However, despite these apparent positive BOLD reports of isoflurane as a gaseous anesthetic with the advantage of good control over anesthesia depth and fast recovery, it is known to be a suppressor of neuronal activity and a potent vasodilator. Isoflurane decreased the amplitudes of evoked potentials by 54% and increased cerebral blood flow by 45% when compared to α-chloralose (Masamoto et al., 2007). Since the BOLD response is highly dependent on CBF (Cohen et al., 2002), most fMRI studies tend to avoid isoflurane in favour of α-chloralose in order to preserve functional-metabolic coupling (Ueki et al., 1992). However, the α_2-adrenergic receptor agonist medetomidine, employed in the present study, is now increasingly preferred due to the ease of implementation and, more importantly still, because

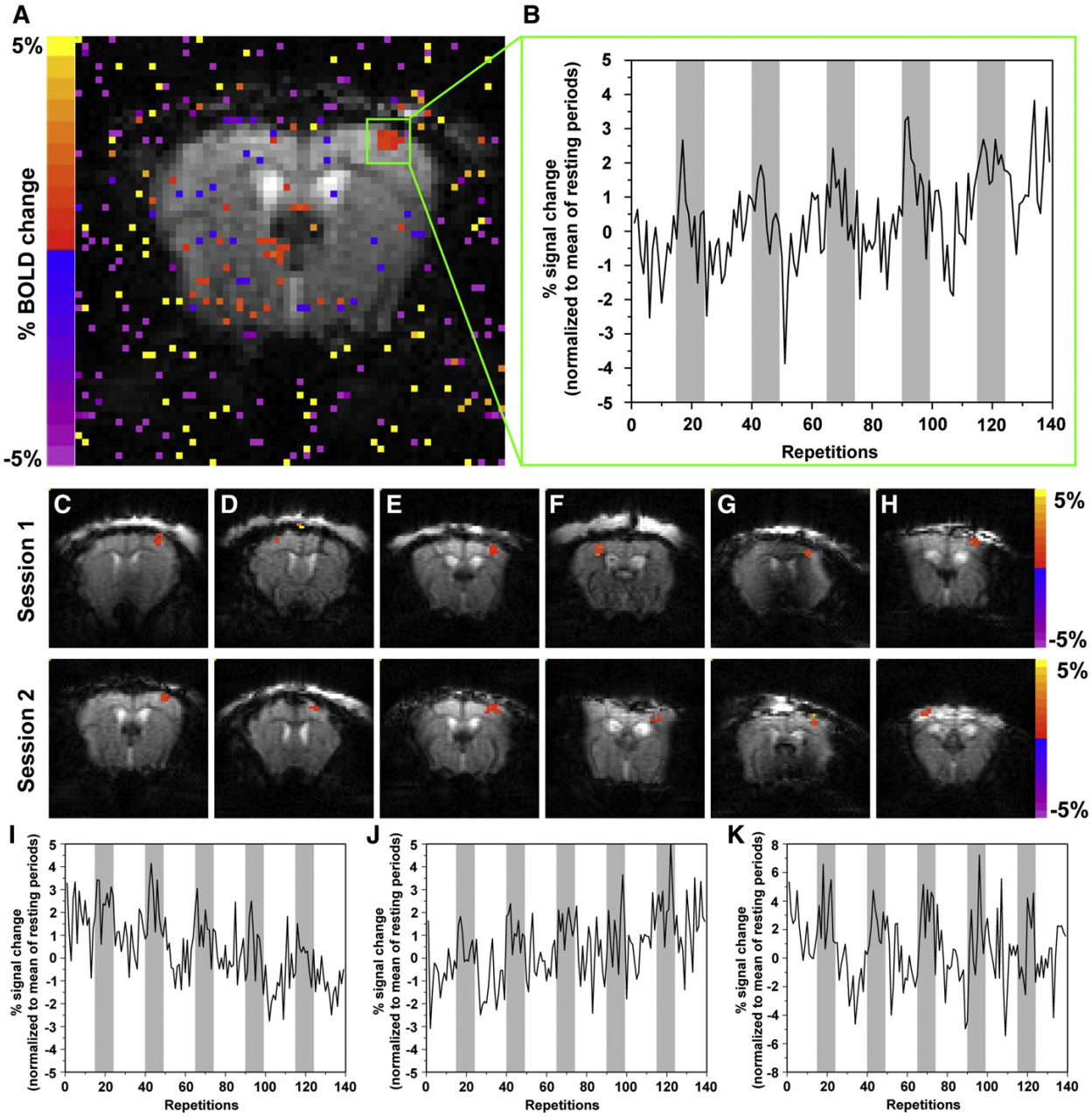

Fig. 3. BOLD activation in the contralateral S1 cortex during unilateral forepaw stimulation. (A) An activation map shows a 2% BOLD change in statistically activated pixels in the S1 when overlayed on a GE EPI image. (B) Time course of the activated pixels from (A) with resting periods indicated in white and stimulation periods in gray. (C–H) BOLD signal observed in 6 of the 9 animals over the course of 2 independent sessions, separated by 3 weeks. Note: images show only the largest cluster of activated pixels. (I-K) Time courses of three different sessions from one animal (H).

of its option to perform longitudinal experiments in the same animals (Pawela et al., 2008; Weber et al., 2008, 2006; Zhao et al., 2008). Similar to α-chloralose (Lindauer et al., 1993; Nakao et al., 2001) dexmedetomidine, the active ingredient of medetomidine is known to reduce cerebral blood flow, as measured by laser Doppler flowmetry in rats (Ganjoo et al., 1998).

BOLD increase in medetomidine sedated rats does not appear to differ from α-chloralose anesthetized rats, and was in the same percentage range (1–1.5%) (Pawela et al., 2008; Weber et al., 2006; Zhao et al., 2008) as observed in our study. However, there are important differences in medetomidine sedation between rats and mice. Maximal average sedation duration in mice achieved in this study was almost 2 h while up to 3.5 h were obtained in rats (Weber et al., 2006). This has been reported to be even extendable up to 6 h (Pawela et al., 2009). However, increasing the dose above 0.4 mg/kg did not increase sedation duration but, instead, resulted in a potential overdose so that some mice had to be euthanized. Since medetomidine also activates α_1-adrenergic receptors, it is possible that arousal and vigilance were increased with higher doses. Studies reviewed by Sinclair et al. (Sinclair, 2003) have shown that activation of central α_1-adrenergic receptors antagonizes

the sedative response to even potent α_2-agonists, such as medetomidine, particularly with high (toxic) doses. The dose of 0.3 mg/kg with a continuous infusion of 0.6 mg/kg/h used here provided stable respiration and transcutaneous recording of CO_2 at a sufficient sedation to perform the fMRI experiments. We cannot exclude that further experimenting with the protocol may further improve the sedation length, though the reported duration was more than sufficient for our purposes. Also repetitive sedation with the dose of 0.3 mg/kg in combination with an infusion of 0.6 mg/kg/h was well tolerated by most mice. However, two mice died in a time window of 4 h after the second sedation, which we cannot exclude to be in context with the sedation.

Using the same field strength as in the present study (11.7T), Ahrens et al. (Ahrens and Dubowitz, 2001) observed a 7% BOLD change in mice, sedated with α-chloralose, upon electrical hindpaw stimulation with much lower stimulation of 50 μA and 3 Hz, the optimal stimulation frequency for α-chloralose anesthesia in rats (Gyngell et al., 1996; Keilholz et al., 2004; Silva et al., 1999). The BOLD intensity in that report is clearly higher than our observed 1.4 + 0.3%. Differences in spatial resolution (leading to varying partial volume dilution of the BOLD effect) can be excluded as explanation: we used $200 \times 200 \times 1000\ \mu m^3$ while Ahrens and Dubowitz reported $180 \times 180 \times 1500\ \mu m^3$. We believe that the difference in BOLD strength must rather be sought for in the physiological and experimental conditions. While all studies so far dealing with electrical paw stimulation needed 1–2 mA for a detectable stimulation, Ahrens and Dubowitz used only 50 μA. As we know from our earlier fMRI studies in rats, hindpaws (used by Ahrens and Dubowitz) need even higher currents than forepaws (Bock et al., 1998). That makes detectability of activation in the somatosensory cortex difficult to understand when using only 50 μA. It appears most likely that the authors recorded at such low stimulation current only slight hemodynamic responses in larger vessels at the surface of the cortex instead of in the deeper layers of the S1 cortex area itself. In favor of this explanation speaks the rather short TE of 7 ms chosen by Ahrens and Dubowitz for their FLASH fMRI experiments compared to the 17.5 ms used in the present study. As shown by Grüne et al. (1999) in FLASH-based fMRI experiments on the somatosensory cortex in rats, the susceptibility gradient from tissue to bone leads to increasing weighting of the BOLD signal to cortical surface vessels with decreasing TE values. Functional brain activation in mice has also been measured with cerebral blood volume (CBV) using an intravenous contrast agent and rapid acquisition relaxation enhancement (RARE) sequence (Mueggler et al., 2001). Changes in CBV upon hindpaw stimulation with 1.5 Hz and 2 mA were around 17%, but temporal resolution was lacking with 21 s per image. Furthermore, this CBV-based fMRI approach has the disadvantage of invasive addition of contrast agent and, in consequence, limited repetitions of activation scans following the contrast agent injection.

The reproducibility of the BOLD response was approximately 50% in the present study. The BOLD response in rats sedated with the medetomidine protocol is more stable, but is also subject to variations. One reason for the lower robustness of the protocol in mice is obviously the strong spontaneous fluctuation of the signal visible in the time courses. Clearly the noise is a complicating factor of mouse fMRI, leading to noisier signal-time curves than in rats. Although transcutaneous CO_2 was stable during the period of sedation, we did not measure absolute partial pressure of CO_2 in arterial blood. We therefore cannot exclude the possibility of a suppressing effect of high CO_2 levels on the hemodynamic response and consequently on BOLD.

Image quality is a key factor for reproducible fMRI experiments. Susceptibility artifacts are prevalent at interfaces of air, bone and tissue and can cause strong local field gradients, leading in consequence to signal loss in T2*-weighted images (Yang et al., 1999). This is particularly so at high magnetic field and is further compounded by the difficulty in shim optimization over small sample volumes like the mouse brain (Ahrens and Dubowitz, 2001; Nair and Duong, 2004). In the present study, T2* values were variable in the S1 cortex from session to session (10–24 ms), consistent with previous reports that suffered even greater variations which those authors did not succeed in removing by shimming (Ahrens and Dubowitz, 2001). We experienced similar field gradients, and the 2nd order MAPSHIM failed repeatedly. However, the introduction of agar in between the mouse head and surface coil substantially increased the field homogeneity so that 2nd order MAPSHIM could be applied successfully. Temporal stability of our image series was found variable between separate sessions (tSNR = 20–60). The variability of the tSNR in our GE-EPI images can be the result of many influencing factors, including physiological factors like respiration rate and heart rate. But most likely we believe that the newly introduced agar head cap leads to a somewhat variable distance between rf surface coil and brain. This will in the future be further optimized.

Conclusions

With the present study, we have established a new, experimental protocol for fMRI studies in mice under controlled physiological conditions. We have demonstrated the feasibility to perform longitudinal and non-invasive fMRI studies following forepaw stimulation in mice sedated with medetomidine. A reproducible BOLD signal was observed in the somatosensory cortex, demonstrating that this new protocol is well suited to be applied for functional brain activation studies in transgenic animal models or for investigations on functional deficit and recovery, respectively, for the assessment of therapeutical strategies in models of brain injury.

Acknowledgments

We wish to thank Andreas Beyrau for assistance with animal preparation. This work was supported in part by grants from the StemStroke EU-FP6 program (LSHB-CT-2006-037526), ENCITE EU-FP7 program (HEALTH-F5-2008-201842), the German BMBF network "Stem cell based regeneration after stroke" (01GN0509), and an Alexander von Humboldt Research Fellowship to TDF.

References

Ahrens, E.T., Dubowitz, D.J., 2001. Peripheral somatosensory fMRI in mouse at 11.7T. NMR Biomed. 14, 318–324.
Bock, C., Krep, H., Brinker, G., Hoehn-Berlage, M., 1998. Brainmapping of alpha-chloralose anesthetized rats with T2*-weighted imaging: distinction between the representation of the forepaw and hindpaw in the somatosensory cortex. NMR Biomed. 11, 115–119.
Brinker, G., Bock, C., Busch, E., Krep, H., Hossmann, K.A., Hoehn-Berlage, M., 1999. Simultaneous recording of evoked potentials and T2*-weighted MR images during somatosensory stimulation of rat. Magn. Reson. Med. 41, 469–473.
Cohen, E.R., Ugurbil, K., Kim, S.G., 2002. Effect of basal conditions on the magnitude and dynamics of the blood oxygenation level-dependent fMRI response. J. Cereb. Blood Flow Metab. 22, 1042–1053.
Franceschini, M.A., Nissila, I., Wu, W., Diamond, S.G., Bonmassar, G., Boas, D.A., 2008. Coupling between somatosensory evoked potentials and hemodynamic response in the rat. Neuroimage 41, 189–203.
Ganjoo, P., Farber, N.E., Hudetz, A., Smith, J.J., Samso, E., Kampine, J.P., Schmeling, W.T., 1998. In vivo effects of dexmedetomidine on laser-Doppler flow and pial arteriolar diameter. Anesthesiology 88, 429–439.
Grüne, M., Pillekamp, F., Schwindt, W., Hoehn, M., 1999. Gradient echo time dependence and quantitative parameter maps for somatosensory activation in rats at 7T. Magn. Reson. Med. 42, 118–126.
Gsell, W., Burke, M., Wiedermann, D., Bonvento, G., Silva, A.C., Dauphin, F., Buhrle, C., Hoehn, M., Schwindt, W., 2006. Differential effects of NMDA and AMPA glutamate receptors on functional magnetic resonance imaging signals and evoked neuronal activity during forepaw stimulation of the rat. J. Neurosci. 26, 8409–8416.
Gyngell, M.L., Bock, C., Schmitz, B., Hoehn-Berlage, M., Hossmann, K.A., 1996. Variation of functional MRI signal in response to frequency of somatosensory stimulation in alpha-chloralose anesthetized rats. Magn. Reson. Med. 36, 13–15.
Hayton, S.M., Kriss, A., Muller, D.P., 1999. Comparison of the effects of four anaesthetic agents on somatosensory evoked potentials in the rat. Lab Anim. 33, 243–251.
Keilholz, S.D., Silva, A.C., Raman, M., Merkle, H., Koretsky, A.P., 2004. Functional MRI of the rodent somatosensory pathway using multislice echo planar imaging. Magn. Reson. Med. 52, 89–99.

Lindauer, U., Villringer, A., Dirnagl, U., 1993. Characterization of CBF response to somatosensory stimulation: model and influence of anesthetics. Am. J. Physiol. 264, H1223–H1228.
Liu, Z.M., Schmidt, K.F., Sicard, K.M., Duong, T.Q., 2004. Imaging oxygen consumption in forepaw somatosensory stimulation in rats under isoflurane anesthesia. Magn. Reson. Med. 52, 277–285.
Masamoto, K., Kim, T., Fukuda, M., Wang, P., Kim, S.G., 2007. Relationship between neural, vascular, and BOLD signals in isoflurane-anesthetized rat somatosensory cortex. Cereb. Cortex 17, 942–950.
Mueggler, T., Baumann, D., Rausch, M., Rudin, M., 2001. Bicuculline-induced brain activation in mice detected by functional magnetic resonance imaging. Magn. Reson. Med. 46, 292–298.
Nair, G., Duong, T.Q., 2004. Echo-planar BOLD fMRI of mice on a narrow-bore 9.4T magnet. Magn. Reson. Med. 52, 430–434.
Nakao, Y., Itoh, Y., Kuang, T.Y., Cook, M., Jehle, J., Sokoloff, L., 2001. Effects of anesthesia on functional activation of cerebral blood flow and metabolism. Proc. Natl. Acad. Sci. U. S. A. 98, 7593–7598.
Ogawa, S., Lee, T.M., Kay, A.R., Tank, D.W., 1990. Brain magnetic resonance imaging with contrast dependent on blood oxygenation. Proc. Natl. Acad. Sci. U. S. A. 87, 9868–9872.
Pawela, C.P., Hudetz, A.G., Ward, B.D., Schulte, M.L., Li, R., Kao, D.S., Mauck, M.C., Cho, Y.R., Neitz, J., Hyde, J.S., 2008. Modeling of region-specific fMRI BOLD neurovascular response functions in rat brain reveals residual differences that correlate with the differences in regional evoked potentials. Neuroimage 41, 525–534.
Pawela, C.P., Biswal, B.B., Hudetz, A.G., Schulte, M.L., Li, R., Jones, S.R., Cho, Y.R., Matloub, H.S., Hyde, J.S., 2009. A protocol for use of medetomidine anesthesia in rats for extended studies using task-induced BOLD contrast and resting-state functional connectivity. Neuroimage 46, 1137–1147.
Rasband, W.S., 1997-2009. ImageJ. U.S. National Institutes of Health, Bethesda, Maryland, USA, http://rsb.info.nih.hov/ij/.
Ruffolo Jr., R.R., Hieble, J.P., 1994. Alpha-adrenoceptors. Pharmacol. Ther. 61, 1–64.
Silva, A.C., Lee, S.P., Yang, G., Iadecola, C., Kim, S.G., 1999. Simultaneous blood oxygenation level-dependent and cerebral blood flow functional magnetic resonance imaging during forepaw stimulation in the rat. J. Cereb. Blood Flow Metab. 19, 871–879.
Silverman, J., Muir III, W.W., 1993. A review of laboratory animal anesthesia with chloral hydrate and chloralose. Lab. Anim. Sci. 43, 210–216.
Sinclair, M.D., 2003. A review of the physiological effects of alpha2-agonists related to the clinical use of medetomidine in small animal practice. Can. Vet. J. 44, 885–897.
Strupp, J.P., 1996. Stimulate: a GUI based fMRI analysis software package. Neuroimage 3, 607.
Troncoso, E., Muller, D., Czellar, S., Zoltan Kiss, J., 2000. Epicranial sensory evoked potential recordings for repeated assessment of cortical functions in mice. J. Neurosci. Methods 97, 51–58.
Ueki, M., Mies, G., Hossmann, K.A., 1992. Effect of alpha-chloralose, halothane, pentobarbital and nitrous oxide anesthesia on metabolic coupling in somatosensory cortex of rat. Acta Anaesthesiol. Scand. 36, 318–322.
Weber, R., Ramos-Cabrer, P., Wiedermann, D., van Camp, N., Hoehn, M., 2006. A fully noninvasive and robust experimental protocol for longitudinal fMRI studies in the rat. Neuroimage 29, 1303–1310.
Weber, R., Ramos-Cabrer, P., Justicia, C., Wiedermann, D., Strecker, C., Sprenger, C., Hoehn, M., 2008. Early prediction of functional recovery after experimental stroke: functional magnetic resonance imaging, electrophysiology, and behavioral testing in rats. J. Neurosci. 28, 1022–1029.
Yang, Q.X., Smith, M.B., Briggs, R.W., Rycyna, R.E., 1999. Microimaging at 14 tesla using GESEPI for removal of magnetic susceptibility artifacts in T(2)(*)-weighted image contrast. J. Magn. Reson. 141, 1–6.
Zhao, F., Zhao, T., Zhou, L., Wu, Q., Hu, X., 2008. BOLD study of stimulation-induced neural activity and resting-state connectivity in medetomidine-sedated rat. Neuroimage 39, 248–260.

Discussion

The aim of this thesis was to investigate regenerative processes after cerebral ischemia. Therefore, specialized methods were established using bioluminescence imaging and magnetic resonance imaging. In particular, the aim was to generate methods that are non-invasive, in order to perform longitudinal studies and monitor the whole dynamic aspect of regeneration. Up to date, the vast majority of studies still employ invasive methods (Thored et al., 2006, Thored et al., 2007, Yu et al., 2007), which allow only single time point measurements and large animal numbers are needed to establish a temporal profile of events. This work combined novel, non-invasive imaging strategies and followed regeneration after stroke for the first time in parallel on different levels: the vascular, the neuronal and the functional level. Post-stroke vascular remodeling was observed longitudinally with two complementary methods. The dynamics of early phases of angiogenesis were visualized by molecular imaging of VEGFR2 expression. Increased VEGFR2 expression revealed the initiation of angiogenesis already early after the insult. This change on the molecular level lead to structural remodeling of the vascular network, which was monitored for up to 4 weeks with a specific MRI based method. Post-stroke neurogenesis was observed with bioluminescence imaging. After the establishment of a brain-specific BLI protocol, increased proliferation of neural progenitor cells was sensitively detected up to 2 weeks after the insult. For the investigation of stroke-induced changes of brain activity, the first non-invasive functional MRI protocol was established for the specific use in mice, as most methods used in this thesis are based on transgenic mice. Differential changes in brain activity and potential spontaneous functional recovery was observed in ischemic mice.

This thesis employed a novel concept of multimodal imaging to look at regeneration after stroke in its entity. It emphasizes the value of non-invasive imaging for pre-clinical stroke research as time courses of dynamic processes can be established and events on different levels can be monitored in parallel. Future studies can combine the individual methods presented in this thesis into a multimodal approach for application in the same animal. This holds the exceptional opportunity to gain an integrated view of different aspects of endogenous regeneration after ischemia with regard to individual-related differences. In particular, the simultaneous and non-invasive observation of angiogenesis and neurogenesis in the same animal will offer to investigate their interaction.

1. Angiogenesis after stroke

This thesis investigated two different approaches for non-invasive imaging of vascular changes after stroke. First, the VEGFR2 was employed as a molecular marker of post-stroke angiogenesis. VEGFR2 is the main receptor involved in angiogenic signaling cascades and invasive methods reported increased expression after stroke (Issa et al., 1999, Marti et al., 2000, Hayashi et al., 2003). Second, SSCE-MRI was chosen to elucidate structural changes of the vascular network after stroke. SSCE-MRI reports changes in regional cerebral blood volume, vessel size and vessel density based on relaxivity changes induced by intravascular contrast agent. While VEGFR2 is an early marker of ongoing vascular changes and already present during the initial destabilization of the existing vascular network, vascular changes visible for SSCE-MRI require functional perfused vessels, which may only occur at later time points during the remodeling process. Hence, these two methods look at different levels and phases of the vascular remodeling process and provide complementary information.

1.1. Imaging angiogenesis on the molecular level

Biological aspects

This study found increased VEGFR2 expression already at 3 days after MCAO, which stayed elevated until the study`s endpoint at 14 days. Western blotting for VEGFR2 confirmed increased expression and immunohistochemical analysis of vessel density revealed slight increases in peri-infarct areas. Similar temporal profiles for VEGFR2 expression after stroke were reported for studies using histological and genetic methods (Issa et al., 1999, Marti et al., 2000). Increased expression started 1 day and persisted for up to 7 days, but levels returned to baseline at 21 days (Hayashi et al., 2003). The expression of VEGFRs was already previously used to investigate angiogenesis non-invasively after cerebral ischemia (Cai et al., 2009). In a rodent model of distal MCAO the expression pattern of VEGFRs was similar to those found in the study presented here. Levels of the VEGFRs increased with peak expression at 9 days, persisting for up to 16 days but returned to baseline after 23 days. An immunohistological quantification confirmed highest VEGFR2 expression around day 10, which is in line with the Western blot results presented in this thesis, showing increased VEGFR2 content on day 7 and day 14 after stroke. 5-bromo-2'-deoxyuridine (BrdU) injection between the second and seventh day after stroke revealed proliferating endothelial cells in the peri-infarct region, indicating the presence of active vascular remodeling. This study performed quantification of vessel numbers and detected slightly increased vessel density in the peri-infarct striatum close to the SVZ, which is known

to be the location of intensive vascular remodeling after stroke (Thored et al., 2007). A direct correlation of changes in VEGFR2 expression levels to increased vessel density cannot be expected, because VEGFR2 expression primarily occurs during the early stages of angiogenic remodeling. The subsequent maturation of vascular sprouts into functional vessels is guided by other molecular cues (angiopoietin 1 - Ang1, platelet-derived growth factor - PDGF), which will increase their signaling at later stages while VEGFR2 will continuously decrease (Hayashi et al., 2003, Marti et al., 2000). It has to be mentioned that some stroke-induced expression of VEGFR2 occurs on neurons and astrocytes (Beck et al., 2002, Hayashi et al., 2003, Li et al., 2011, Lennmyr et al., 1998, Issa et al., 1999). Nevertheless, VEGFR2 is primarily involved in angiogenesis, and, following stroke, predominantly increases expression in endothelial cells (Marti et al., 2000).

Methodological aspects

Within this PhD thesis, VEGFR2 expression after stroke was investigated with BLI using a transgenic mouse line (Lyons et al., 2005). Photon emission is proportional to the amount of luciferase, if the substrate luciferin is given in excessive amounts (Virostko et al., 2004). In-vivo BLI has to deal with tissue-induced light absorption and scattering, but can be used as semi-quantitative measure (Keyaerts et al., 2012a). If the same condition is followed over time, relative changes can be calculated. Usually the relative change is calculated to a control condition, however, as injection-related signal variation can be observed between time points, it is advisable to include this control within each imaging session. In the present study the intact hemisphere was used as control condition, thus, injection-induced variation of signal intensity was subtracted from the measurement.

Stroke induces injury to endothelial cells and the blood brain-barrier (BBB), which results in increased permeability for molecules circulating through the vasculature (Strbian et al., 2008). Although luciferin is a molecule with small molecular weight and freely diffusible across the BBB (Hochgrafe and Mandelkow, 2012), a frequently discussed complication of BLI in the stroke pathology is the potentially increased substrate availability due to the open BBB. Careful observation of the kinetics between intact and ischemic hemisphere, as well as comparison of sham and MCAO animals in the presented study, suggest only a minor effect of destroyed BBB on maximal photon emission. Photon emission during the acute phase (at day 3 after stroke) was similar in sham and MCAO animals, although MCAO animals are expected to have a more severely injured BBB. The photon emission during the steady state (starting approximately 10 min after injection), can be considered to be proportional to the luciferase content (Virostko and Jansen, 2009), since luciferin is assumed to have distributed equally throughout the system.

Recently, the VEGFR2 expression pattern following stroke was non-invasively investigated employing PET (Cai et al., 2009). Similar to BLI, PET has a high sensitivity and low spatial resolution. The major advantage of the model investigated in this thesis is the low invasiveness and the simplicity of the experimental execution, which does not need the time-consuming production of radioactive tracers. Thus many repetitive experiments are possible and give the opportunity to establish a temporal profile with an hourly resolution.

This non-invasive imaging approach is the first to monitor the dynamics of angiogenesis on the molecular level with BLI using a transgenic mouse that expresses luciferase under the control of the VEGFR2 promotor. VEGFR2 is primarily involved in angiogenesis initiation and can specifically report early phases of the angiogenic response to stroke. The implementation of VEGFR2 as a biomarker for post-stroke angiogenesis revealed the temporal profile of the molecular regulation of vascular remodelling after cerebral ischemia. The herein observed increased VEGFR2 expression up to 14 days after the insult indicates continuous active vascular remodelling even at chronic phases. Vascular remodelling translated into increased vessel density in distinct peri-infarct areas.

1.2. Imaging angiogenesis on the structural level

Biological aspects

This thesis observed significantly decreased vessel density in the ischemic striatum at 7d after stroke. Stroke induced endothelial injury and subsequent endothelial apoptosis were reported in this phase after stroke (Hayashi et al., 2003) and result in detectable vascular regression. At the same time, mean vessel size was significantly increased, which is a commonly observed characteristic of vasculature after stroke (Bosomtwi et al., 2008, Lin et al., 2008a) and may be attributable to vasodilation in response to hypoxic cues, as well as a possible result of predominant regression of small capillaries shifting the mean vessel size to arterioles. Although BrdU labeling proved the presence of endothelial cell proliferation in the first week after stroke, this thesis could not detect any elevation of vessel density above pre-stroke values in the striatum or in the peri-lesional area with SSCE-MRI. During the process of angiogenesis early vessels are not yet perfused (Ohab et al., 2006). The observation presented here indicates that not all new vascular sprouts become functional and perfused. Recent reports even indicate that angiogenesis after stroke is transient process (Thored et al., 2007, Yu et al., 2007) and only a minor population of vessels might reach maturity, which would explain the normalization of vessel density at around 2 weeks after stroke. Immunohistological quantification of vessel numbers at 28 days post stroke confirms no additional increase in vessel density above baseline levels.

Methodological aspects

The method of SSCE MRI detects specific characteristics of the vasculature, like total CBV and CBV in microvessels (5-10 µm), and conveys this measure into information about mean vessel size and mean vessel density. As only perfused vessels contribute to the signal, this method can detect changes in the amount of functional vessels. The large body of literature providing positive reports about increase in vessel density after stroke used classical immunohistological approaches of endothelial cell staining (Glut-1, RECA-1, CD31, vWF) or basement membrane staining (laminin), which do not reveal the functional status of the vasculature. An improved immunohistological protocol, employing the perfusion of the vasculature with a fluorescent dye and thereby labeling only functional vessels, could verify non-perfused vessels in the peri-infarct area (Ohab et al., 2006). Since SSCE-MRI only visualizes perfused vessels (Yu et al., 2007, Thored et al., 2007), these newly generated non-perfused vessels are not detected. Previous studies employing SSCE-MRI to track angiogenesis after stroke were also not able to detect increased vessel density in striatal or cortical tissue (Bosomtwi et al., 2008, Lin et al., 2008a). Only vessels of the pial network in the leptomeninges showed increased density in response to distal MCAO (Lin et al., 2002, Lin et al., 2008b), which may be in relation with the choice of the stroke model. Nevertheless, vascular remodeling after stroke is an established concept (Arai et al., 2009). Angiogenic sprouting and subsequent vascular maturation may be present only in small distinct areas of the brain (Thored et al., 2007), the detection of which is obscured by analysis of mainly large areas of interest, as is common in SSCE-MRI. Additionally, we noted that SSCE-MRI has an inherent susceptibility to noise, with variation of up to 20%. Changes in vessel density below this threshold may therefore not be reliably detectable.

1.3. New insights into vascular remodeling after stroke

In this thesis vascular changes after stroke were monitored with two different non-invasive methods, which evokes the unique position to integrate the complementary information into a multi-dimensional result. Vascular remodeling was monitored on the molecular and on the structural level with additional indication of vessel functionality. The strong up-regulation of VEGFR2 in response to stroke in the ischemic hemisphere is in agreement with previous studies (Cai et al., 2009, Hayashi et al., 2003, Issa et al., 1999, Marti et al., 2000). It persisted up to 14 days and revealed ongoing angiogenic signaling on the molecular level even during chronic phases after ischemia. Vascular remodeling during this phase was supported with invasive methods by the detection of endothelial cell proliferation and by increased vessel density in distinct areas around the lesion. SSCE-MRI reported pronounced structural changes of the vasculature during the first three weeks after

stroke. An initial strong decrease of vessel density in ischemic core areas was followed by renormalization around 2 weeks after ischemia. Invasive methods revealed endothelial cell proliferation within the first week after stroke but vessel density did not rise above pre-stroke values during chronic phases. The overall integration of the two complementary studies suggests that post-stroke vascular remodeling resulted in new microvessels, but not all became functional. Therefore the MRI based method only detected renormalization of vessel density but no increase compared to contralateral values. However, the detection of increased vessel density may have been obscured by analysis of a large area of interest, as is common in SSCE-MRI. Elevated vessel density above normal levels was predominantly reported from distinct areas of the peri-infarct region (Thored et al., 2007), which may be blurred by the analysis of a larger area. Furthermore, a species-dependent effect can not be excluded, as the BLI study used mice and the SSCE-MRI study used rats. The angiogenic response may vary between species, especially since the ischemic intensity will differ. Preliminary results of a SSCE-MRI study on a mouse model of MCAO, which was performed in conjunction with this thesis, indicate the non-invasive detection of areas with increased vessel density. However, especially small regions of interest were employed for the analysis to bypass the possible blur effect.

Valuable information about post-stroke vascular remodeling was gained by the integration of the results from two complementary non-invasive methods. For the first time the aspects of molecular, structural and functional changes are presented in a temporal context. Longitudinal BLI of VEGFR2 expression as a biomarker for post-stroke angiogenesis revealed continuous angiogenic signaling on the molecular level far into the chronic phase. Structural and functional changes of the vasculature were detected by SSCE-MRI and showed an initial pronounced loss of functional vessels in the ischemic territory. Angiogenic cues translated into new functional microvessels and increased vessel density beginning 2 weeks after the insult. Vessel density increased above baseline values only in distinct peri-infarct areas. However, overall vessel density of the ischemic territory normalized beginning 2 weeks after the insult.

2. Adult neurogenesis after stroke

Since the discovery of adult neurogenesis several techniques have been employed to study the dynamic process of neurogenesis with non-invasive methods, including iron oxide labeling for MRI (Shapiro et al., 2006, Granot et al., 2011, Sumner et al., 2009), radionucleotide-labeled thymidine analog for PET (Rueger et al., 2010), or viral transduction with reporters for optical imaging (Vande Velde et al., 2011, Reumers et al., 2008). The aim of this thesis was to establish a new sensitive method to follow endogenous neurogenesis more specifically than previous approaches. Recently, a special transgenic mouse was created, which expresses firefly luciferase under the control of the doublecortin promotor.

Doublecortin is a microtubule binding protein and its expression is specific for proliferative and migratory neural progenitor cells (Brown et al., 2003). The visualization of adult neurogenesis becomes possible with BLI (Couillard-Despres et al., 2008). This transgenic mouse was employed to establish for the first time a brain-specific BLI protocol optimized for sensitivity. Subsequently, this thesis detected sensitively and specifically the endogenous neurogenic response to stroke for the first time with a non-invasive strategy.

2.1. Brain-specific bioluminescence imaging

The high sensitivity of BLI is advantageous for in vivo imaging of neurogenesis because numbers of neural stem/progenitor cells in the brain are low. In mice a total amount of 35 proliferating neural progenitor cells were counted in the neurogenic niche of the SVZ (Kazanis and Ffrench-Constant, 2012). After injury, the amount of proliferating progenitor cells was approximately 10 times higher (Kazanis and Ffrench-Constant, 2012). These numbers illustrate the need for an optimized BLI protocol in order to be able to track changes of only small magnitude. This thesis investigated increasing substrate concentration, different injection routes, different anesthesia regimens and timing of anesthesia using the DCX-luc mouse (Couillard-Despres et al., 2008) in order to find the optimal protocol for this specific model. In accordance to previous studies, increasing luciferin concentration led to increased photon emission (Keyaerts et al., 2012b). However, even the highest concentration did not saturate the luciferase in contrast to other reports (Contag et al., 1997). The results presented in this thesis show an exponential increase in photon emission with increasing luciferin concentration. A boost in substrate diffusivity across the BBB can be assumed as the major contributor to exponentially increased photon emission, which is further supported by the observation of a steeper photon emission slope within the first 5 min, indicating a faster inflow of luciferin into the brain. According to observations in other model systems, iv injection of luciferin yielded a higher emission compared to classical ip injection. In our DCX-luc model iv injection led to 4 times higher emission than ip injection. Anesthesia was reported to have an effect on luciferase kinetics (Keyaerts et al., 2012b). This study compared isoflurane, ketamin/xylazin and pentobarbital. In contrast to previously published observations pentobarbital did not lead to significantly increased photon emission (Keyaerts et al., 2012b) and ketamin/xylazin decreased the emission compared to isoflurane anesthesia. Furthermore, emission peaks were delayed under pentobarbital and ketamin/xylazin anesthesia compared to isoflurane anesthesia, which corresponds to the stronger impact of these anesthetics on the cardiovascular system (Janssen et al., 2004). A great boost in photon emission was achieved when luciferin was injected into awake animals before anesthesia with isoflurane. This indicates that the enzyme-substrate complex is less

inhibited by isoflurane. Integration of all observations under practical, financial and temporal aspects revealed an optimal protocol: 300 mg/kg luciferin ip injected before anesthesia with isoflurane. This advanced BLI protocol allowed to visualize unambiguously 3000 intracerebrally transplanted neural stem cells, which were transduced to express clickbeetle luciferase under a constitutive active promotor. The direct comparison to a BLI protocol most often used in literature (150 mg/kg luciferin after isoflurane anesthesia) revealed that not even 6000 cells were unambiguously detectable. This study is unique, as it evaluated systematically many BLI influencing factors with special regard to brain specific application, and small cell populations can be tracked in the brain in future studies.

2.2. Bioluminescence imaging of endogenous neurogenesis after stroke

This study employed the DCX-luc mouse model with the optimized BLI protocol to follow the neurogenic response to stroke. Ten male homozygote DCX-luc mice (Couillard-Despres et al., 2008) (age 6 months) received a MCAO (30 min occlusion time) and 3 mice received sham surgery. We recorded photon emission before, 7 days and 14 days post MCAO. Additionally, we performed MRI and calculated T2-maps for the visualization of lesion extension. Before stroke, photon emission was equal from left and right hemisphere. Seven days after MCAO, photon emission was increased around 4% above the ischemic hemisphere (Figure 10). No change in photon emission between left and right hemisphere was observed 7 days after sham surgery. Increased photon emission from the ischemic hemisphere was still present at 14 days after MCAO. Immunohistochemical analysis of DCX^+ cells did not reveal massive increase in the amount of DCX^+ cells. However, a somewhat thicker SVZ was noted at the rostral end of the SVZ (Figure 10D).

These preliminary results suggest that even small changes in proliferation of neural progenitor cells in the SVZ upon stroke can be detected and followed by BLI. In particular, increased proliferation was present over 2 weeks after stroke. This time course was previously introduced by invasive studies (Thored et al., 2006, Thored et al., 2007, Yamashita et al., 2006, Zhang et al., 2004) and can be refined now. We detected increased photon emission from the ischemic hemisphere at 7 and 14 days, indicating increased proliferation of DCX^+ cells. Enhanced proliferation of neural progenitor cells within the SVZ was described as early as 2 days after the insult, peaked at 1-2 weeks, and returned in some studies to baseline proliferation at 3-4 weeks. In particular, the number of DCX^+ cells reached peak numbers around 2-3 weeks and was still elevated for up to 6 weeks after stroke (Zhang et al., 2004, Thored et al., 2006, Yamashita et al., 2006). The magnitude of increase was

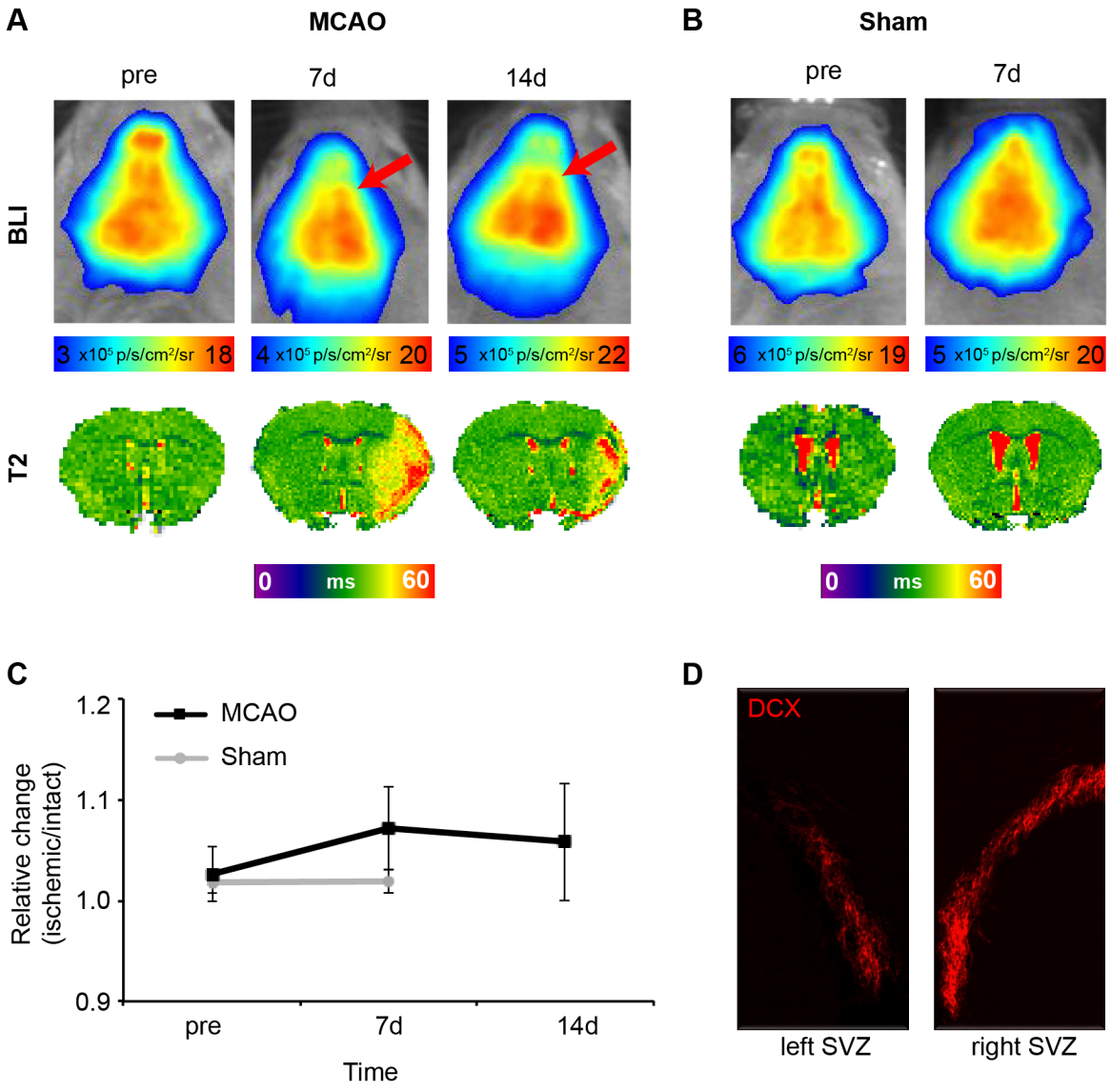

Figure 10: Longitudinal and non-invasive observation of increased neurogenesis after stroke. **A** Representative brain BLI from one exemplary DCX-luc mouse showing increased photon emission from the ischemic (right) hemisphere at 7 and 14 days after MCAO. **B** Sham surgery did not lead to changes in photon emission. **C** Quantification of the stroke-induced changes in BLI signal revealed an approximately 4% increase in photon emission compared to the intact hemisphere. Healthy and sham animals retained equal photon emission from both hemispheres. **D** Exemplary immunohistological staining of DCX^+ cells in the left and right subventricular zone (SVZ).

between a 2-fold increase up to a 7-fold increase in DCX^+ cells within the SVZ (Parent et al., 2002, Yamashita et al., 2006). This study detected only an increase of a few percent, which may be due to signal absorption by tissue resulting in signal attenuation from deeper structures in the brain. Furthermore, as this study normalized the signal from the ischemic hemisphere to the intact side, any increase in proliferation on the intact hemisphere will decrease the effect from the ischemic hemisphere. Nevertheless, such a strategy was chosen in order to be quantitative and control for any irregularities in signal intensities between imaging sessions. The neurogenic response to stroke not only consists of increased proliferation in the SVZ, but also directed migration towards the injury as well as integration and differentiation into the appropriate neuronal cell type is initiated (Arvidsson et al., 2002, Parent et al., 2002, Thored et al., 2006). For example, DCX positive cells migrate along blood vessels towards the ischemic striatum (Yamashita et al., 2006, Thored et al., 2007, Kojima et al., 2010) and the first DCX^+ cells were detected in peri-infarct areas as early as 24h after ischemia (Jin et al., 2003). Although the resolution of BLI is poor due to scattering, previous studies were able to resolve the migration along the rostral migratory stream under healthy conditions (Reumers et al., 2008, Vande Velde et al., 2011). This study indicates a shift of the major migratory direction from the dorso-rostral axis (rostral migratory stream) into a more lateral migration (towards the ischemic striatum) as a shift of the center of mass is visible on bioluminescence images (Figure 10A).

Initially, the neurogenic response to stroke was studied with invasive techniques, e.g. quantifying BrdU incorporation (Jin et al., 2001, Zhang et al., 2001) or immunohistochemical labeling of neural precursor specific proteins (Arvidsson et al., 2002, Parent et al., 2002, Jin et al., 2003, Thored et al., 2006). To date, only one study followed stroke-induced neurogenic proliferation in the SVZ non-invasively employing PET in combination with a radionucleotide-labeled thymidine analog (Rueger et al., 2010). However, this study is not completely neurogenesis-specific, since also other cell types, like astrocytes, start to proliferate in the SVZ after stroke. Bioluminescence imaging was successfully applied to follow the endogenous neurogenesis under healthy conditions (Reumers et al., 2008, Vande Velde et al., 2011, Couillard-Despres et al., 2008). However, these studies employed viral vectors to label all proliferating cells in the SVZ (Reumers et al., 2008, Vande Velde et al., 2011). Under healthy conditions, proliferating cells within the SVZ are predominantly neural precursors, but under ischemic conditions astrocytic and endothelial cell proliferation will confound the specificity. The study presented in this thesis is the first to investigate the temporal profile of the neurogenic response to stroke non-invasively with BLI. In particular, it is very specific to neurogenesis, since it uses an approach with a molecular marker specific for neural precursor cells. Thus, the DCX-luc mouse model is an optimal tool to follow stroke-induced neurogenesis and provides the opportunity to investigate neurogenesis-related therapies.

This thesis established an optimal protocol for brain-specific BLI. No systematic evaluation of so many factors influencing the BLI signal existed before with the focus on brain-specific circumstances. Increased neurogenesis in response to stroke was monitored with exceptional sensitivity in a transgenic mouse expressing luciferase under the control of the DCX-promotor, a neural progenitor cell-specific protein. This is the first report of non-invasive and specific monitoring of post-stroke neurogenesis.

3. Functional brain activity after stroke

The primary goal of any stroke therapy is to restore or protect brain function. Until recently, the benefit of a therapy was measured by lesion size. However, this does not necessarily correlate with functional improvement. It is therefore indispensible to evaluate the effect of a given therapy on functional recovery. Non-invasive functional MRI can visualize the activity of specific brain areas and can follow any changes in brain function due to the insult. Functional MRI is an established method in rats and several studies investigated the effect of therapies on functional recovery. As the availability of transgenic mouse models is increasing and already most studies within this thesis are dependent on the use of a specific transgenic mouse, this thesis also established the first non-invasive fMRI protocol for mice and subsequently investigated functional changes of brain activity after stroke.

3.1. Establishment of mouse functional magnetic resonance imaging

Biological aspects

The implementation of a longitudinal and non-invasive protocol for mouse fMRI involved the choice of an appropriate anesthesia. Classical anesthetics like isoflurane allow repetitive measurements on the same animal but suppress functional brain activity or induce vasodilation, which intervenes negatively with the physiological basis of the BOLD contrast generation. Nevertheless, isoflurane was employed for functional studies of the mouse brain but required very low levels of the anesthetics (e.g. 0.4 – 0.7%) in combination with strong peripheral electrical stimulation (6mA) (Nair and Duong, 2004). In some cases the additional administration of a muscle relaxant to reduce movement during image acquisition was implemented, which made artificial ventilation necessary (Mueggler et al., 2003). To overcome these drawbacks, we chose the sedative agent medetomidine, which allows spontaneous breathing and was already successfully employed in functional studies of the rat brain. Medetomidine is an α_2-adrenoreceptor agonist, the main effects of which are relayed in the locus ceruleus and brain stem. Activation of α_2-adrenoeceptors by medetomidine reduces the global sympathetic output resulting in sedation, analgesia and

muscle relaxation. Side effect of medetomidine include decreased cardiac output, hypotension, hypothermia and diuresis. Slight hypercapnia was observed after medetomidnie administration (Adamczak et al., 2010, Ramos-Cabrer et al., 2005), which can circumvent BOLD signal detection due to cerebral vasodilation. However, pCO_2 and pO_2 monitoring revealed hypercapnia is only transient in mice and BOLD detection under medetomidine sedation is possible after a transition period of a few minutes. Unilateral forepaw stimulation resulted in contralateral activation of the primary and the secondary somatosensory cortex (S1 and the S2), which is in agreement with previously observed responses to forepaw stimulation in rats (Weber et al., 2006). Mouse hindpaw stimulation was performed under α-chloralose sedation and reported contralateral activation of the hindpaw representation. However, also bilateral activation was observed in response to unilateral forepaw stimulation in mice (Bosshard et al., 2010).

Methodological aspects

MRI can visualize functionally active brain regions non-invasively using the differential magnetic properties of oxy-hemoglobin versus deoxy-hemoglobin. Upon neural activity, the hemodynamic response increases the supply of oxy-hemoglobin and gives rise to the BOLD contrast. The BOLD contrast is an indirect measure of neural activity, which is already routinely used in human studies due to its good temporal and spatial resolution. Recently, a protocol for functional MRI studies of the rat brain was established and found application in the investigation of stroke recovery after stem cell therapy (Ramos-Cabrer et al., 2010). This thesis established the first protocol for longitudinal and non-invasive imaging of brain function in mice. Previous fMRI protocols for mice were either using anesthetics not appropriate for functional studies (isoflurane (Nair and Duong, 2004, Mueggler et al., 2001)) or anesthetics with strong side effects not appropriate for survival studies (α-chloralose). Therefore the establishment of the new mouse fMRI protocol offers the opportunity to employ transgenic mice to study the long-term effect of specific genes on functional activity or functional reorganization after stroke.

The small mouse brain has an unfavorable “surface to volume”-ratio. Susceptibility difference of air, skull and brain tissue induce strong field inhomogeneities (Yang et al., 1999), resulting in strong signal voids along the cerebral cortex. It was not possible to restore field homogeneity by implemented shimming methods. Only the introduction of an agarose cap on the mouse head was capable of reducing signal voids within the cortex. The high field strength of 11.7 Tesla used in this fMRI study had on the one hand positive effects on temporal and spatial resolution, but had negative influence on the field homogeneity around the small mouse head. The implementation of mouse fMRI at lower field strength would augment the strong signal voids, as field inhomogeneities will be less severe. The application

of a cryogenic coil has high potential for future studies as active cooling of the coil results in decreased electronic noise levels and can therefore detect small changes due to the BOLD signal more sensitively (Bosshard et al., 2010).

3.2. Imaging functional activity after stroke

The new protocol for functional studies of the mouse brain was established with the aim to investigate functional recovery processes after cerebral ischemia. Therefore, 6 mice were subjected to right MCAO (30 min occlusion time) and received a T2 scan 2 days after MCAO for lesion location. Functional response to forepaw stimulation was investigated 21 days after MCAO and 100 days after MCAO. These pilot experiments on ischemic mice successfully detected brain activity upon forepaw stimulation. The sedation with medetomidine was well tolerated by the weak mice with cerebral ischemia. Even repetitive administration did not result in any complication (data not shown). Although the lesion in the brain gave rise to small signal distortions, brain activity was unambiguously detectable even close to the lesion (Figure 11).

The preliminary results indicate differential behavior of functional brain responses to stroke. One mouse with only striatal lesion responded with BOLD signal in both, the left and right somatosensory cortex, after contralateral forepaw stimulation (Figure 11A). No functional activation in the ischemic hemisphere was observed in a mouse with the lesion extending into the S1 cortex, while activation in the intact hemisphere was preserved (Figure 11B). However, another mouse also presenting with a lesion in the S1 cortex showed retained functionality on both sides. Activation on the ischemic hemisphere was shifted caudally when compared to the activation on the intact hemisphere (Figure 11C).

Spontaneous functional recovery of the somatosensory cortex was observed in a rat model of MCAO (Weber et al., 2008). Animals lost the functional response to forepaw stimulation temporarily but recovered functionality around 2 weeks after stroke. However, animals that did not recover until 14 days post MCAO, lost the functionality of the S1 permanently. Similar observations were made in this thesis and the feasibility to investigate spontaneous recovery processes in mice was demonstrated.

This thesis established the first non-invasive functional MRI protocol for the specific needs of mice. It is now possible to investigate brain function when employing a transgenic mouse for a study. The first non-invasive studies of brain activity on ischemic mice revealed differential spontaneous recovery of function in the somatosensory cortex.

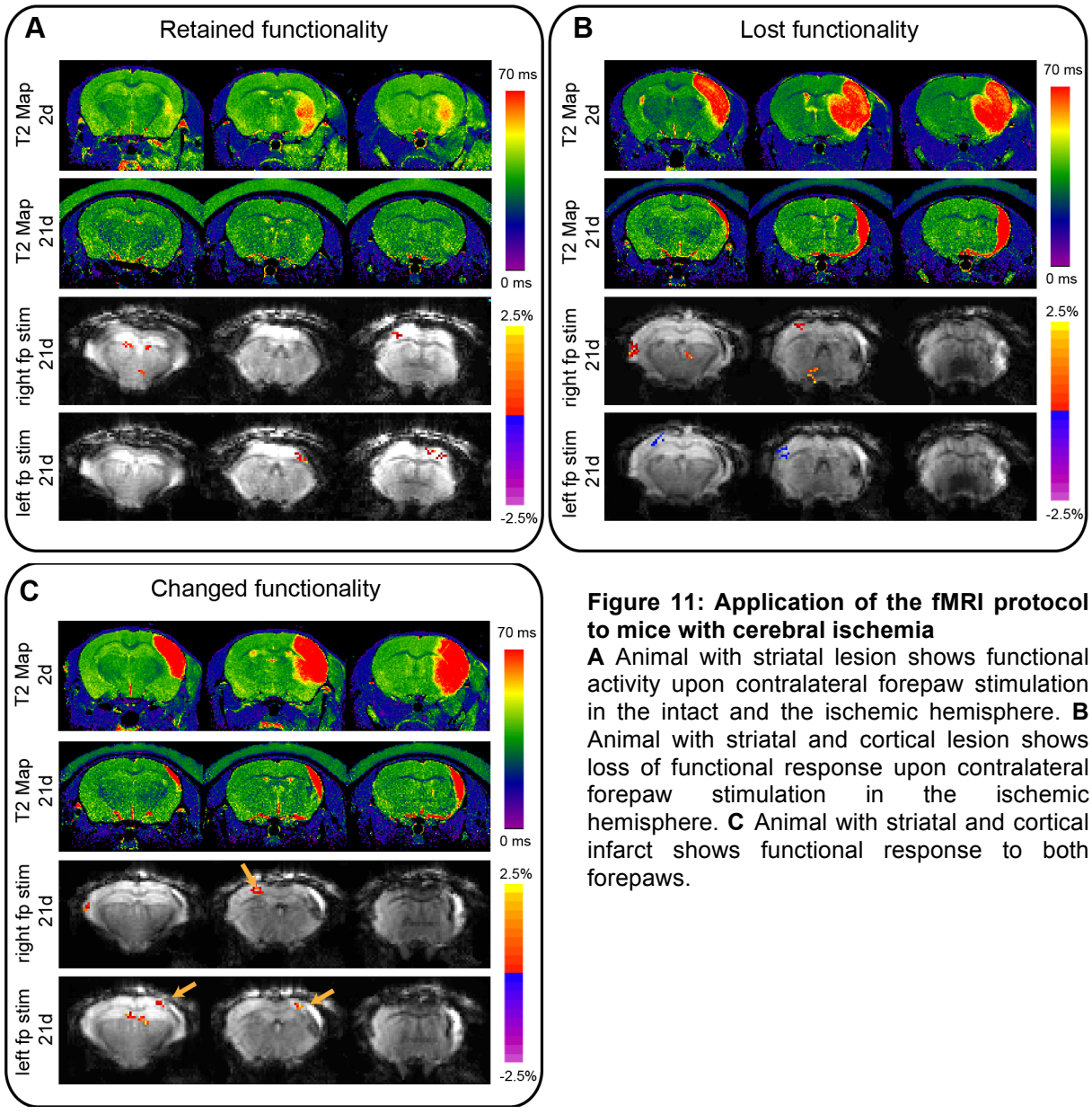

Figure 11: Application of the fMRI protocol to mice with cerebral ischemia
A Animal with striatal lesion shows functional activity upon contralateral forepaw stimulation in the intact and the ischemic hemisphere. **B** Animal with striatal and cortical lesion shows loss of functional response upon contralateral forepaw stimulation in the ischemic hemisphere. **C** Animal with striatal and cortical infarct shows functional response to both forepaws.

4. Summary

The aim of this thesis was to investigate regenerative processes after cerebral ischemia with non-invasive imaging methods. Two major regenerative processes are initiated after stroke: angiogenesis and neurogenesis. This thesis has successfully tracked the processes of angiogenesis and neurogenesis after stroke. In particular, the BLI and MRI-based methods, optimized and established for the present approach, raised the exceptional opportunity to follow their temporal and spatial dynamics, as it has not been possible before. Post-stroke vascular remodeling was observed longitudinally with two complementary methods. The dynamics of early phases of angiogenesis were visualized by molecular imaging of VEGFR2 expression, a receptor highly involved in angiogenic signal transduction. For the first time a transgenic mouse expressing luciferase under the control of the VEGFR2 promotor was employed for BLI imaging of angiogenesis regulation in response to ischemia. Increased VEGFR2 expression revealed the initiation of angiogenesis already early after the insult. This change on the molecular level lead to structural remodeling of the vascular network, which was monitored for up to 4 weeks with a specific MRI based method. SSCE-MRI employs an intravascular contrast agent to report microvessel density and microvessel size of perfused vessels. Thus, SSCE-MRI detects the functional status of microvessels and revealed that part of the new vascular network became perfused after 2 weeks post the insult. Endogenous neurogenesis was observed with bioluminescence imaging using a transgenic mouse expressing luciferase under the control of the DCX promotor, a neural progenitor cell specific protein. This thesis reports the first systematic investigation of factors influencing the BLI signal with special regard to brain application. An optimal protocol for the sensitive investigation of post-stroke neurogenesis was established. Subsequently, for the first time it was possible to specifically detect increased proliferation of endogenous neural progenitor cells in response to stroke. Since regeneration should lead to functional improvement, this thesis further established a non-invasive functional readout to track the changes of functional activity of distinct brain regions in the mouse model of stroke. This is the first report of functional MRI in mice. It is of exceptional importance as, similar to this thesis, most regenerative studies are performed on mice or transgenic mice. Pilot experiments performed in mice with ischemic brain lesions detected differential behavior of spontaneous functional recovery. These results underline the importance of the fMRI protocol for mice, as the effect of therapies on functional recovery can be determined and separated from spontaneous recovery.

5. Outlook

This thesis investigated each regenerative process individually. However, these processes occur in parallel and in close physical proximity. Angiogenesis and neurogenesis even share signal molecules and thereby influence each other. This thesis lays the basis to investigate the interdependency of angiogenesis and neurogenesis. All methods are purposely non-invasive, which not only reduces animal numbers and fulfills the requirements of ethics committees, but also allows the combination into multimodal approaches. This offers the exceptional opportunity to monitor both processes in parallel in one animal. In particular, the response of both processes to a treatment can be observed and thereby allocate the primary treatment effect. For example, angiogenesis enhancing therapy can be now applied to the DCX-luc mouse model. While the MR-based method of SSCE-MRI will monitor the changes in vascular density and size after angiogenesis enhancing therapy, the DCX-luc mouse will show the therapeutic effect on neurogenesis. The overall functional benefit of the treatment can be investigated with the fMRI protocol.

This thesis lays down a portfolio of methods, which can be combined into multimodal approaches for pre-clinical investigation of post-stroke regeneration. This will facilitate the discovery of new therapeutic targets within the endogenous regenerative capacity. Furthermore, new therapeutic approaches can be tested easily and quickly for their effect on angiogenesis and neurogenesis as well as for their effect on functional recovery.

References

Adamczak, J. M., Farr, T. D., Seehafer, J. U., Kalthoff, D. & Hoehn, M. 2010. High field BOLD response to forepaw stimulation in the mouse. *Neuroimage,* 51**,** 704-12.

Adams, R. H. & Alitalo, K. 2007. Molecular regulation of angiogenesis and lymphangiogenesis. *Nat Rev Mol Cell Biol,* 8**,** 464-78.

Albers, G. W., Clark, W. M., Madden, K. P. & Hamilton, S. A. 2002. ATLANTIS trial: results for patients treated within 3 hours of stroke onset. Alteplase Thrombolysis for Acute Noninterventional Therapy in Ischemic Stroke. *Stroke,* 33**,** 493-5.

Alvarez-Buylla, A., Seri, B. & Doetsch, F. 2002. Identification of neural stem cells in the adult vertebrate brain. *Brain Res Bull,* 57**,** 751-8.

Arai, K., Jin, G., Navaratna, D. & Lo, E. H. 2009. Brain angiogenesis in developmental and pathological processes: neurovascular injury and angiogenic recovery after stroke. *FEBS J,* 276**,** 4644-52.

Arvidsson, A., Collin, T., Kirik, D., Kokaia, Z. & Lindvall, O. 2002. Neuronal replacement from endogenous precursors in the adult brain after stroke. *Nat Med,* 8**,** 963-70.

Attwell, D., Buchan, A. M., Charpak, S., Lauritzen, M., Macvicar, B. A. & Newman, E. A. 2010. Glial and neuronal control of brain blood flow. *Nature,* 468**,** 232-43.

Attwell, D. & Laughlin, S. B. 2001. An energy budget for signaling in the grey matter of the brain. *J Cereb Blood Flow Metab,* 21**,** 1133-45.

Bang, O. Y., Lee, J. S., Lee, P. H. & Lee, G. 2005. Autologous mesenchymal stem cell transplantation in stroke patients. *Ann Neurol,* 57**,** 874-82.

Beck, H., Acker, T., Puschel, A. W., Fujisawa, H., Carmeliet, P. & Plate, K. H. 2002. Cell type-specific expression of neuropilins in an MCA-occlusion model in mice suggests a potential role in post-ischemic brain remodeling. *J Neuropathol Exp Neurol,* 61**,** 339-50.

Beck, H., Acker, T., Wiessner, C., Allegrini, P. R. & Plate, K. H. 2000. Expression of angiopoietin-1, angiopoietin-2, and tie receptors after middle cerebral artery occlusion in the rat. *Am J Pathol,* 157**,** 1473-83.

Beck, H. & Plate, K. H. 2009. Angiogenesis after cerebral ischemia. *Acta Neuropathol,* 117**,** 481-96.

Belayev, L., Alonso, O. F., Busto, R., Zhao, W. & Ginsberg, M. D. 1996. Middle cerebral artery occlusion in the rat by intraluminal suture. Neurological and pathological evaluation of an improved model. *Stroke,* 27**,** 1616-22; discussion 1623.

Belayev, L., Busto, R., Zhao, W., Fernandez, G. & Ginsberg, M. D. 1999. Middle cerebral artery occlusion in the mouse by intraluminal suture coated with poly-L-lysine: neurological and histological validation. *Brain Res,* 833**,** 181-90.

Bosomtwi, A., Jiang, Q., Ding, G. L., Zhang, L., Zhang, Z. G., Lu, M., Ewing, J. R. & Chopp, M. 2008. Quantitative evaluation of microvascular density after stroke in rats using MRI. *J Cereb Blood Flow Metab,* 28**,** 1978-87.

Bosshard, S. C., Baltes, C., Wyss, M. T., Mueggler, T., Weber, B. & Rudin, M. 2010. Assessment of brain responses to innocuous and noxious electrical forepaw stimulation in mice using BOLD fMRI. *Pain,* 151**,** 655-63.

Brown, J. P., Couillard-Despres, S., Cooper-Kuhn, C. M., Winkler, J., Aigner, L. & Kuhn, H. G. 2003. Transient expression of doublecortin during adult neurogenesis. *J Comp Neurol,* 467**,** 1-10.

Cai, W., Guzman, R., Hsu, A. R., Wang, H., Chen, K., Sun, G., Gera, A., Choi, R., Bliss, T., He, L., Li, Z. B., Maag, A. L., Hori, N., Zhao, H., Moseley, M., Steinberg, G. K. & Chen, X. 2009. Positron emission tomography imaging of poststroke angiogenesis. *Stroke,* 40**,** 270-7.

Carmeliet, P. & Tessier-Lavigne, M. 2005. Common mechanisms of nerve and blood vessel wiring. *Nature,* 436**,** 193-200.

Chavez, J. C., Hurko, O., Barone, F. C. & Feuerstein, G. Z. 2009. Pharmacologic interventions for stroke: looking beyond the thrombolysis time window into the penumbra with biomarkers, not a stopwatch. *Stroke,* 40**,** e558-63.

Christie, K. J. & Turnley, A. M. 2013. Regulation of endogenous neural stem/progenitor cells for neural repair—factors that promote neurogenesis and gliogenesis in the normal and damaged brain. *Frontiers in Cellular Neuroscience,* 6.

Clapp, C., Thebault, S., Jeziorski, M. C. & Martinez De La Escalera, G. 2009. Peptide hormone regulation of angiogenesis. *Physiol Rev,* 89**,** 1177-215.

Clark, W., Lutsep, H., Barnwell S, Nesbit G, Egan R, North E, Yanase L, Lowenkopf T, Petersen B, Grunwald Iq, Mayer T, Doerfler A, Struffert T, Engelhorn T, Richter G, Grunwald Iq, Reith W, Berkefeld J, Madison M, Myers M, Goddard J, Lassig J, Lopes D, Shownkeen H, Echiverri H, Nour F, Mazumdar A, Budzik R, Pema P, Frei D, Huddle D, Bellon R, Heck D, Ferguson R, Mcdougall C, Flaster M, Frey J, Albuquerque F, Malkoff M, Zaidat O, Branca V, Ahktar N, Rymer M, Rai A, Brooks C, Carpenter J, Popovich T, Chaloupka J, Hellinger F, Rasmussen P, Masaryk T, Fiorella D, Woo H, Rudolph S, Spiegel G, Silverman I, Ohki S & J., G. 2009. The penumbra pivotal stroke trial: safety and effectiveness of a new generation of mechanical devices for clot removal in intracranial large vessel occlusive disease. *Stroke,* 40**,** 2761-8.

Contag, C. H., Spilman, S. D., Contag, P. R., Oshiro, M., Eames, B., Dennery, P., Stevenson, D. K. & Benaron, D. A. 1997. Visualizing gene expression in living mammals using a bioluminescent reporter. *Photochem Photobiol,* 66**,** 523-31.

Couillard-Despres, S., Finkl, R., Winner, B., Ploetz, S., Wiedermann, D., Aigner, R., Bogdahn, U., Winkler, J., Hoehn, M. & Aigner, L. 2008. In vivo optical imaging of neurogenesis: watching new neurons in the intact brain. *Mol Imaging,* 7**,** 28-34.

Curtis, M. A., Kam, M., Nannmark, U., Anderson, M. F., Axell, M. Z., Wikkelso, C., Holtas, S., Van Roon-Mom, W. M., Bjork-Eriksson, T., Nordborg, C., Frisen, J., Dragunow, M., Faull, R. L. & Eriksson, P. S. 2007. Human neuroblasts migrate to the olfactory bulb via a lateral ventricular extension. *Science,* 315**,** 1243-9.

Ding, G., Jiang, Q., Li, L., Zhang, L., Zhang, Z. G., Ledbetter, K. A., Panda, S., Davarani, S. P., Athiraman, H., Li, Q., Ewing, J. R. & Chopp, M. 2008. Magnetic resonance imaging investigation of axonal remodeling and angiogenesis after embolic stroke in sildenafil-treated rats. *J Cereb Blood Flow Metab,* 28**,** 1440-8.

Dirnagl, U., Iadecola, C. & Moskowitz, M. A. 1999. Pathobiology of ischaemic stroke: an integrated view. *Trends Neurosci,* 22**,** 391-7.

Donnan, G. A., Fisher, M., Macleod, M. & Davis, S. M. 2008. Stroke. *Lancet,* 371**,** 1612-23.

Durukan, A. & Tatlisumak, T. 2007. Acute ischemic stroke: overview of major experimental rodent models, pathophysiology, and therapy of focal cerebral ischemia. *Pharmacol Biochem Behav,* 87**,** 179-97.

Ehrenreich, H., Hasselblatt, M., Dembowski, C., Cepek, L., Lewczuk, P., Stiefel, M., Rustenbeck, H. H., Breiter, N., Jacob, S., Knerlich, F., Bohn, M., Poser, W., Ruther, E., Kochen, M., Gefeller, O., Gleiter, C., Wessel, T. C., De Ryck, M., Itri, L., Prange, H., Cerami, A., Brines, M. & Siren, A. L. 2002. Erythropoietin therapy for acute stroke is both safe and beneficial. *Mol Med,* 8**,** 495-505.

Ehrenreich, H., Weissenborn, K., Prange, H., Schneider, D., Weimar, C., Wartenberg, K., Schellinger, P. D., Bohn, M., Becker, H., Wegrzyn, M., Jahnig, P., Herrmann, M., Knauth, M., Bahr, M., Heide, W., Wagner, A., Schwab, S., Reichmann, H., Schwendemann, G., Dengler, R., Kastrup, A. & Bartels, C. 2009. Recombinant human erythropoietin in the treatment of acute ischemic stroke. *Stroke,* 40**,** e647-56.

Ekdahl, C. T., Kokaia, Z. & Lindvall, O. 2009. Brain inflammation and adult neurogenesis: the dual role of microglia. *Neuroscience,* 158**,** 1021-9.

Eriksson, P. S., Perfilieva, E., Bjork-Eriksson, T., Alborn, A. M., Nordborg, C., Peterson, D. A. & Gage, F. H. 1998. Neurogenesis in the adult human hippocampus. *Nat Med,* 4**,** 1313-7.

Fagan, S. C., Waller, J. L., Nichols, F. T., Edwards, D. J., Pettigrew, L. C., Clark, W. M., Hall, C. E., Switzer, J. A., Ergul, A. & Hess, D. C. 2010. Minocycline to improve neurologic outcome in stroke (MINOS): a dose-finding study. *Stroke,* 41**,** 2283-7.

Fatahzadeh, M. & Glick, M. 2006. Stroke: epidemiology, classification, risk factors, complications, diagnosis, prevention, and medical and dental management. *Oral Surg Oral Med Oral Pathol Oral Radiol Endod,* 102**,** 180-91.

Ferrara, N. 1999. Molecular and biological properties of vascular endothelial growth factor. *J Mol Med (Berl),* 77**,** 527-43.

Ferrara, N. 2004. Vascular endothelial growth factor: basic science and clinical progress. *Endocr Rev,* 25**,** 581-611.

Ginsberg, M. D. 2003. Adventures in the pathophysiology of brain ischemia: penumbra, gene expression, neuroprotection: the 2002 Thomas Willis Lecture. *Stroke,* 34**,** 214-23.

Gould, E., Reeves, A. J., Graziano, M. S. & Gross, C. G. 1999. Neurogenesis in the neocortex of adult primates. *Science,* 286**,** 548-52.

Granot, D., Scheinost, D., Markakis, E. A., Papademetris, X. & Shapiro, E. M. 2011. Serial monitoring of endogenous neuroblast migration by cellular MRI. *Neuroimage,* 57**,** 817-24.

Hacke, W., Kaste, M., Bluhmki, E., Brozman, M., Davalos, A., Guidetti, D., Larrue, V., Lees, K. R., Medeghri, Z., Machnig, T., Schneider, D., Von Kummer, R., Wahlgren, N. & Toni, D. 2008. Thrombolysis with alteplase 3 to 4.5 hours after acute ischemic stroke. *N Engl J Med,* 359**,** 1317-29.

Hacke, W., Kaste, M., Fieschi, C., Von Kummer, R., Davalos, A., Meier, D., Larrue, V., Bluhmki, E., Davis, S., Donnan, G., Schneider, D., Diez-Tejedor, E. & Trouillas, P. 1998. Randomised double-blind placebo-controlled trial of thrombolytic therapy with intravenous alteplase in acute ischaemic stroke (ECASS II). Second European-Australasian Acute Stroke Study Investigators. *Lancet,* 352**,** 1245-51.

Hastings, J. W. 1996. Chemistries and colors of bioluminescent reactions: a review. *Gene,* 173**,** 5-11.

Hata, R., Maeda, K., Hermann, D., Mies, G. & Hossmann, K. A. 2000. Evolution of brain infarction after transient focal cerebral ischemia in mice. *J Cereb Blood Flow Metab,* 20**,** 937-46.

Hayashi, T., Noshita, N., Sugawara, T. & Chan, P. H. 2003. Temporal profile of angiogenesis and expression of related genes in the brain after ischemia. *J Cereb Blood Flow Metab,* 23**,** 166-80.

Hayward, N. M., Yanev, P., Haapasalo, A., Miettinen, R., Hiltunen, M., Grohn, O. & Jolkkonen, J. 2011. Chronic hyperperfusion and angiogenesis follow subacute hypoperfusion in the thalamus of rats with focal cerebral ischemia. *J Cereb Blood Flow Metab,* 31**,** 1119-32.

Hochgrafe, K. & Mandelkow, E. M. 2012. Making the Brain Glow: In Vivo Bioluminescence Imaging to Study Neurodegeneration. *Mol Neurobiol*.

Iadecola, C. & Anrather, J. 2011a. The immunology of stroke: from mechanisms to translation. *Nat Med,* 17**,** 796-808.

Iadecola, C. & Anrather, J. 2011b. Stroke research at a crossroad: asking the brain for directions. *Nat Neurosci,* 14**,** 1363-8.

Iadecola, C. & Nedergaard, M. 2007. Glial regulation of the cerebral microvasculature. *Nat Neurosci,* 10**,** 1369-76.

Inoue, Y., Kiryu, S., Izawa, K., Watanabe, M., Tojo, A. & Ohtomo, K. 2009. Comparison of subcutaneous and intraperitoneal injection of D-luciferin for in vivo bioluminescence imaging. *Eur J Nucl Med Mol Imaging,* 36**,** 771-9.

Inouye, S. 2010. Firefly luciferase: an adenylate-forming enzyme for multicatalytic functions. *Cell Mol Life Sci,* 67**,** 387-404.

Issa, R., Krupinski, J., Bujny, T., Kumar, S., Kaluza, J. & Kumar, P. 1999. Vascular endothelial growth factor and its receptor, KDR, in human brain tissue after ischemic stroke. *Lab Invest,* 79**,** 417-25.

Janssen, B. J., De Celle, T., Debets, J. J., Brouns, A. E., Callahan, M. F. & Smith, T. L. 2004. Effects of anesthetics on systemic hemodynamics in mice. *Am J Physiol Heart Circ Physiol,* 287**,** H1618-24.

Jiang, Q., Zhang, Z. G., Ding, G. L., Zhang, L., Ewing, J. R., Wang, L., Zhang, R., Li, L., Lu, M., Meng, H., Arbab, A. S., Hu, J., Li, Q. J., Pourabdollah Nejad, D. S., Athiraman, H. & Chopp, M. 2005. Investigation of neural progenitor cell induced angiogenesis after embolic stroke in rat using MRI. *Neuroimage,* 28**,** 698-707.

Jin, K., Minami, M., Lan, J. Q., Mao, X. O., Batteur, S., Simon, R. P. & Greenberg, D. A. 2001. Neurogenesis in dentate subgranular zone and rostral subventricular zone after focal cerebral ischemia in the rat. *Proc Natl Acad Sci U S A,* 98**,** 4710-5.

Jin, K., Sun, Y., Xie, L., Peel, A., Mao, X. O., Batteur, S. & Greenberg, D. A. 2003. Directed migration of neuronal precursors into the ischemic cerebral cortex and striatum. *Mol Cell Neurosci,* 24**,** 171-89.

Kazanis, I. & Ffrench-Constant, C. 2012. The number of stem cells in the subependymal zone of the adult rodent brain is correlated with the number of ependymal cells and not with the volume of the niche. *Stem Cells Dev,* 21**,** 1090-6.

Keyaerts, M., Caveliers, V. & Lahoutte, T. 2012a. Bioluminescence imaging: looking beyond the light. *Trends Mol Med,* 18**,** 164-72.

Keyaerts, M., Heneweer, C., Gainkam, L. O., Caveliers, V., Beattie, B. J., Martens, G. A., Vanhove, C., Bossuyt, A., Blasberg, R. G. & Lahoutte, T. 2011. Plasma protein binding of luciferase substrates influences sensitivity and accuracy of bioluminescence imaging. *Mol Imaging Biol,* 13**,** 59-66.

Keyaerts, M., Remory, I., Caveliers, V., Breckpot, K., Bos, T. J., Poelaert, J., Bossuyt, A. & Lahoutte, T. 2012b. Inhibition of firefly luciferase by general anesthetics: effect on in vitro and in vivo bioluminescence imaging. *PLoS One,* 7**,** e30061.

Keyaerts, M., Verschueren, J., Bos, T. J., Tchouate-Gainkam, L. O., Peleman, C., Breckpot, K., Vanhove, C., Caveliers, V., Bossuyt, A. & Lahoutte, T. 2008. Dynamic bioluminescence imaging for quantitative tumour burden assessment using IV or IP administration of D: -luciferin: effect on intensity, time kinetics and repeatability of photon emission. *Eur J Nucl Med Mol Imaging,* 35**,** 999-1007.

Koehler, R. C., Roman, R. J. & Harder, D. R. 2009. Astrocytes and the regulation of cerebral blood flow. *Trends Neurosci,* 32**,** 160-9.

Koizumi, J., Yoshida, Y., Nakazawa, T. & Ooneda, G. 1986. Experimental studies of ischemic brain edema. 1. A new experimental model of cerebral embolism in rats in which circulation can be introduced in the ischemic area. *Jpn J Stroke***,** 1-8.

Kojima, T., Hirota, Y., Ema, M., Takahashi, S., Miyoshi, I., Okano, H. & Sawamoto, K. 2010. Subventricular zone-derived neural progenitor cells migrate along a blood vessel scaffold toward the post-stroke striatum. *Stem Cells,* 28**,** 545-54.

Kondziolka, D., Steinberg, G. K., Wechsler, L., Meltzer, C. C., Elder, E., Gebel, J., Decesare, S., Jovin, T., Zafonte, R., Lebowitz, J., Flickinger, J. C., Tong, D., Marks, M. P., Jamieson, C., Luu, D., Bell-Stephens, T. & Teraoka, J. 2005. Neurotransplantation for patients with subcortical motor stroke: a phase 2 randomized trial. *J Neurosurg,* 103**,** 38-45.

Krupinski, J., Kaluza, J., Kumar, P., Kumar, S. & Wang, J. M. 1994. Role of angiogenesis in patients with cerebral ischemic stroke. *Stroke,* 25**,** 1794-8.

Kulcsar, Z., Bonvin, C., Pereira, V. M., Altrichter, S., Yilmaz, H., Lovblad, K. O., Sztajzel, R. & Rufenacht, D. A. 2010. Penumbra system: a novel mechanical thrombectomy device for large-vessel occlusions in acute stroke. *AJNR Am J Neuroradiol,* 31**,** 628-33.

Lampl, Y., Boaz, M., Gilad, R., Lorberboym, M., Dabby, R., Rapoport, A., Anca-Hershkowitz, M. & Sadeh, M. 2007. Minocycline treatment in acute stroke: an open-label, evaluator-blinded study. *Neurology,* 69**,** 1404-10.

Lauterbur, P. C. 1989. Image formation by induced local interactions. Examples employing nuclear magnetic resonance. 1973. *Clin Orthop Relat Res***,** 3-6.

Lee, S., Chen, T. T., Barber, C. L., Jordan, M. C., Murdock, J., Desai, S., Ferrara, N., Nagy, A., Roos, K. P. & Iruela-Arispe, M. L. 2007. Autocrine VEGF signaling is required for vascular homeostasis. *Cell,* 130**,** 691-703.

Lee, S. T., Chu, K., Jung, K. H., Kim, S. J., Kim, D. H., Kang, K. M., Hong, N. H., Kim, J. H., Ban, J. J., Park, H. K., Kim, S. U., Park, C. G., Lee, S. K., Kim, M. & Roh, J. K. 2008. Anti-inflammatory mechanism of intravascular neural stem cell transplantation in haemorrhagic stroke. *Brain,* 131**,** 616-29.

Lees, K. R., Zivin, J. A., Ashwood, T., Davalos, A., Davis, S. M., Diener, H. C., Grotta, J., Lyden, P., Shuaib, A., Hardemark, H. G. & Wasiewski, W. W. 2006. NXY-059 for acute ischemic stroke. *N Engl J Med,* 354**,** 588-600.

Lennmyr, F., Ata, K. A., Funa, K., Olsson, Y. & Terent, A. 1998. Expression of vascular endothelial growth factor (VEGF) and its receptors (Flt-1 and Flk-1) following permanent and transient occlusion of the middle cerebral artery in the rat. *J Neuropathol Exp Neurol,* 57**,** 874-82.

Li, L., Jiang, Q., Zhang, L., Ding, G., Gang Zhang, Z., Li, Q., Ewing, J. R., Lu, M., Panda, S., Ledbetter, K. A., Whitton, P. A. & Chopp, M. 2007. Angiogenesis and improved cerebral blood flow in the ischemic boundary area detected by MRI after administration of sildenafil to rats with embolic stroke. *Brain Res,* 1132**,** 185-92.

Li, W. L., Fraser, J. L., Yu, S. P., Zhu, J., Jiang, Y. J. & Wei, L. 2011. The role of VEGF/VEGFR2 signaling in peripheral stimulation-induced cerebral neurovascular regeneration after ischemic stroke in mice. *Exp Brain Res,* 214**,** 503-13.

Lin, C. Y., Chang, C., Cheung, W. M., Lin, M. H., Chen, J. J., Hsu, C. Y., Chen, J. H. & Lin, T. N. 2008a. Dynamic changes in vascular permeability, cerebral blood volume, vascular density, and size after transient focal cerebral ischemia in rats: evaluation with contrast-enhanced magnetic resonance imaging. *J Cereb Blood Flow Metab,* 28**,** 1491-501.

Lin, H., De Vos, D., Decuypere, E. & Buyse, J. 2008b. Dynamic changes in parameters of redox balance after mild heat stress in aged laying hens (Gallus gallus domesticus). *Comp Biochem Physiol C Toxicol Pharmacol,* 147**,** 30-5.

Lin, T. N., Sun, S. W., Cheung, W. M., Li, F. & Chang, C. 2002. Dynamic changes in cerebral blood flow and angiogenesis after transient focal cerebral ischemia in rats. Evaluation with serial magnetic resonance imaging. *Stroke,* 33**,** 2985-91.

Lin, T. N., Wang, C. K., Cheung, W. M. & Hsu, C. Y. 2000. Induction of angiopoietin and Tie receptor mRNA expression after cerebral ischemia-reperfusion. *J Cereb Blood Flow Metab,* 20**,** 387-95.

Longa, E. Z., Weinstein, P. R., Carlson, S. & Cummins, R. 1989. Reversible middle cerebral artery occlusion without craniectomy in rats. *Stroke,* 20**,** 84-91.

Lyons, S. K., Clermont, A. O., Neben, T. Y., Campbell, K., Coffee, R., Hunter, J., Purchio, T. F. & Jenkins, D. E. 2005. Non-invasive in vivo bioluminescent imaging of tumor angiogenesis in mice. *AACR Meeting Abstracts,* 2005**,** 903-b-.

Macleod, M. R., Van Der Worp, H. B., Sena, E. S., Howells, D. W., Dirnagl, U. & Donnan, G. A. 2008. Evidence for the efficacy of NXY-059 in experimental focal cerebral ischaemia is confounded by study quality. *Stroke,* 39**,** 2824-9.

Marti, H. J., Bernaudin, M., Bellail, A., Schoch, H., Euler, M., Petit, E. & Risau, W. 2000. Hypoxia-induced vascular endothelial growth factor expression precedes neovascularization after cerebral ischemia. *Am J Pathol,* 156**,** 965-76.

Meairs, S., Wahlgren, N., Dirnagl, U., Lindvall, O., Rothwell, P., Baron, J. C., Hossmann, K., Engelhardt, B., Ferro, J., Mcculloch, J., Kaste, M., Endres, M., Koistinaho, J., Planas, A., Vivien, D., Dijkhuizen, R., Czlonkowska, A., Hagen, A., Evans, A., De Libero, G., Nagy, Z., Rastenyte, D., Reess, J., Davalos, A., Lenzi, G. L., Amarenco, P. & Hennerici, M. 2006. Stroke research priorities for the next decade--A representative view of the European scientific community. *Cerebrovasc Dis,* 22**,** 75-82.

Minnerup, J., Heidrich, J., Rogalewski, A., Schabitz, W. R. & Wellmann, J. 2009. The efficacy of erythropoietin and its analogues in animal stroke models: a meta-analysis. *Stroke,* 40**,** 3113-20.

Minnerup, J., Sutherland, B. A., Buchan, A. M. & Kleinschnitz, C. 2012. Neuroprotection for stroke: current status and future perspectives. *Int J Mol Sci,* 13**,** 11753-72.

Minnerup, J., Wersching, H., Ringelstein, E. B., Schilling, M., Schabitz, W. R., Wellmann, J. & Berger, K. 2011. Impact of the extended thrombolysis time window on the proportion of recombinant tissue-type plasminogen activator-treated stroke patients and on door-to-needle time. *Stroke,* 42**,** 2838-43.

Mitsios, N., Gaffney, J., Kumar, P., Krupinski, J., Kumar, S. & Slevin, M. 2006. Pathophysiology of acute ischaemic stroke: an analysis of common signalling mechanisms and identification of new molecular targets. *Pathobiology,* 73**,** 159-75.

Moskowitz, M. A., Lo, E. H. & Iadecola, C. 2010. The science of stroke: mechanisms in search of treatments. *Neuron,* 67**,** 181-98.

Mueggler, T., Baumann, D., Rausch, M. & Rudin, M. 2001. Bicuculline-induced brain activation in mice detected by functional magnetic resonance imaging. *Magn Reson Med,* 46**,** 292-8.

Mueggler, T., Baumann, D., Rausch, M., Staufenbiel, M. & Rudin, M. 2003. Age-dependent impairment of somatosensory response in the amyloid precursor protein 23 transgenic mouse model of Alzheimer's disease. *J Neurosci,* 23**,** 8231-6.

Nair, G. & Duong, T. Q. 2004. Echo-planar BOLD fMRI of mice on a narrow-bore 9.4 T magnet. *Magn Reson Med,* 52**,** 430-4.

Naritomi, H., Moriwaki, H., Metoki, N., Nishimura, H., Higashi, Y., Yamamoto, Y., Yuasa, H., Oe, H., Tanaka, K., Saito, K., Terayama, Y., Oda, T., Tanahashi, N. & Kondo, H. 2010. Effects of edaravone on muscle atrophy and locomotor function in patients with ischemic stroke: a randomized controlled pilot study. *Drugs R D,* 10**,** 155-63.

Nelson, P. T., Kondziolka, D., Wechsler, L., Goldstein, S., Gebel, J., Decesare, S., Elder, E. M., Zhang, P. J., Jacobs, A., Mcgrogan, M., Lee, V. M. & Trojanowski, J. Q. 2002. Clonal human (hNT) neuron grafts for stroke therapy: neuropathology in a patient 27 months after implantation. *Am J Pathol,* 160**,** 1201-6.

O'collins, V. E., Macleod, M. R., Donnan, G. A., Horky, L. L., Van Der Worp, B. H. & Howells, D. W. 2006. 1,026 experimental treatments in acute stroke. *Ann Neurol,* 59**,** 467-77.

Ogawa, A., Yoshimoto, T., Kikuchi, H., Sano, K., Saito, I., Yamaguchi, T. & Yasuhara, H. 1999. Ebselen in acute middle cerebral artery occlusion: a placebo-controlled, double-blind clinical trial. *Cerebrovasc Dis,* 9**,** 112-8.

Ogawa, S., Lee, T. M., Kay, A. R. & Tank, D. W. 1990. Brain magnetic resonance imaging with contrast dependent on blood oxygenation. *Proc Natl Acad Sci U S A,* 87**,** 9868-72.

Ohab, J. J., Fleming, S., Blesch, A. & Carmichael, S. T. 2006. A neurovascular niche for neurogenesis after stroke. *J Neurosci,* 26**,** 13007-16.

Oki, K., Tatarishvili, J., Wood, J., Koch, P., Wattananit, S., Mine, Y., Monni, E., Tornero, D., Ahlenius, H., Ladewig, J., Brustle, O., Lindvall, O. & Kokaia, Z. 2012. Human-induced pluripotent stem cells form functional neurons and improve recovery after grafting in stroke-damaged brain. *Stem Cells,* 30**,** 1120-33.

Palmer, T. D., Willhoite, A. R. & Gage, F. H. 2000. Vascular niche for adult hippocampal neurogenesis. *J Comp Neurol,* 425**,** 479-94.

Parent, J. M., Vexler, Z. S., Gong, C., Derugin, N. & Ferriero, D. M. 2002. Rat forebrain neurogenesis and striatal neuron replacement after focal stroke. *Ann Neurol,* 52**,** 802-13.

Paxinos, G. & Franklin, K. B. 2001. *The Mouse Brain in Stereotaxic Coordinates*, Academic Press.

Ramos-Cabrer, P., Justicia, C., Wiedermann, D. & Hoehn, M. 2010. Stem cell mediation of functional recovery after stroke in the rat. *PLoS One,* 5**,** e12779.

Ramos-Cabrer, P., Weber, R., Wiedermann, D. & Hoehn, M. 2005. Continuous noninvasive monitoring of transcutaneous blood gases for a stable and persistent BOLD contrast in fMRI studies in the rat. *NMR Biomed,* 18**,** 440-6.

Reumers, V., Deroose, C. M., Krylyshkina, O., Nuyts, J., Geraerts, M., Mortelmans, L., Gijsbers, R., Van Den Haute, C., Debyser, Z. & Baekelandt, V. 2008. Noninvasive and quantitative monitoring of adult neuronal stem cell migration in mouse brain using bioluminescence imaging. *Stem Cells,* 26**,** 2382-90.

Rueger, M. A., Backes, H., Walberer, M., Neumaier, B., Ullrich, R., Simard, M. L., Emig, B., Fink, G. R., Hoehn, M., Graf, R. & Schroeter, M. 2010. Noninvasive imaging of endogenous neural stem cell mobilization in vivo using positron emission tomography. *J Neurosci,* 30**,** 6454-60.

Sadikot, R. T. & Blackwell, T. S. 2005. Bioluminescence imaging. *Proc Am Thorac Soc,* 2**,** 537-40, 511-2.

Saver, J. L., Kidwell, C., Eckstein, M. & Starkman, S. 2004. Prehospital neuroprotective therapy for acute stroke: results of the Field Administration of Stroke Therapy-Magnesium (FAST-MAG) pilot trial. *Stroke,* 35**,** e106-8.

Schabitz, W. R., Laage, R., Vogt, G., Koch, W., Kollmar, R., Schwab, S., Schneider, D., Hamann, G. F., Rosenkranz, M., Veltkamp, R., Fiebach, J. B., Hacke, W., Grotta, J. C., Fisher, M. & Schneider, A. 2010. AXIS: a trial of intravenous granulocyte colony-stimulating factor in acute ischemic stroke. *Stroke,* 41**,** 2545-51.

Shapiro, E. M., Gonzalez-Perez, O., Manuel Garcia-Verdugo, J., Alvarez-Buylla, A. & Koretsky, A. P. 2006. Magnetic resonance imaging of the migration of neuronal precursors generated in the adult rodent brain. *Neuroimage,* 32**,** 1150-7.

Shuaib, A., Lees, K. R., Lyden, P., Grotta, J., Davalos, A., Davis, S. M., Diener, H. C., Ashwood, T., Wasiewski, W. W. & Emeribe, U. 2007. NXY-059 for the treatment of acute ischemic stroke. *N Engl J Med,* 357**,** 562-71.

Silva, A. C., Lee, S. P., Iadecola, C. & Kim, S. G. 2000. Early temporal characteristics of cerebral blood flow and deoxyhemoglobin changes during somatosensory stimulation. *J Cereb Blood Flow Metab,* 20**,** 201-6.

Smith, W. S., Sung, G., Saver, J., Budzik, R., Duckwiler, G., Liebeskind, D. S., Lutsep, H. L., Rymer, M. M., Higashida, R. T., Starkman, S., Gobin, Y. P., Frei, D., Grobelny, T., Hellinger, F., Huddle, D., Kidwell, C., Koroshetz, W., Marks, M., Nesbit, G. & Silverman, I. E. 2008. Mechanical thrombectomy for acute ischemic stroke: final results of the Multi MERCI trial. *Stroke,* 39**,** 1205-12.

Smith, W. S., Sung, G., Starkman, S., Saver, J. L., Kidwell, C. S., Gobin, Y. P., Lutsep, H. L., Nesbit, G. M., Grobelny, T., Rymer, M. M., Silverman, I. E., Higashida, R. T., Budzik, R. F. & Marks, M. P. 2005. Safety and efficacy of mechanical embolectomy in acute ischemic stroke: results of the MERCI trial. *Stroke,* 36**,** 1432-8.

Strbian, D., Durukan, A., Pitkonen, M., Marinkovic, I., Tatlisumak, E., Pedrono, E., Abo-Ramadan, U. & Tatlisumak, T. 2008. The blood-brain barrier is continuously open for several weeks following transient focal cerebral ischemia. *Neuroscience,* 153**,** 175-81.

Sumner, J. P., Shapiro, E. M., Maric, D., Conroy, R. & Koretsky, A. P. 2009. In vivo labeling of adult neural progenitors for MRI with micron sized particles of iron oxide: quantification of labeled cell phenotype. *Neuroimage,* 44**,** 671-8.

Sun, Y., Jin, K., Xie, L., Childs, J., Mao, X. O., Logvinova, A. & Greenberg, D. A. 2003. VEGF-induced neuroprotection, neurogenesis, and angiogenesis after focal cerebral ischemia. *J Clin Invest,* 111**,** 1843-51.

Sutton, E. J., Henning, T. D., Pichler, B. J., Bremer, C. & Daldrup-Link, H. E. 2008. Cell tracking with optical imaging. *Eur Radiol,* 18**,** 2021-32.

Szpak, G. M., Lechowicz, W., Lewandowska, E., Bertrand, E., Wierzba-Bobrowicz, T. & Dymecki, J. 1999. Border zone neovascularization in cerebral ischemic infarct. *Folia Neuropathol,* 37**,** 264-8.

Thored, P., Arvidsson, A., Cacci, E., Ahlenius, H., Kallur, T., Darsalia, V., Ekdahl, C. T., Kokaia, Z. & Lindvall, O. 2006. Persistent production of neurons from adult brain stem cells during recovery after stroke. *Stem Cells,* 24**,** 739-47.

Thored, P., Wood, J., Arvidsson, A., Cammenga, J., Kokaia, Z. & Lindvall, O. 2007. Long-term neuroblast migration along blood vessels in an area with transient angiogenesis and increased vascularization after stroke. *Stroke,* 38**,** 3032-9.

Tohgi, H., Kogure, K., Hirai, S., Takakura, K., Terashi, A., Gotoh, F., Maruyama, S., Taza- Ki, Y., Shinohara, Y., Ito, E., Sawada, T., Yamaguchi, T., Kikuchi, H., Kobayashi, S., Fujishima, M. & Nakashima, M. 2003. Effect of a novel free radical scavenger, edaravone (MCI-186), on acute brain infarction. Randomized, placebo-controlled, double-blind study at multicenters. *Cerebrovasc Dis,* 15**,** 222-9.

Vande Velde, G., Rangarajan, J. R., Toelen, J., Dresselaers, T., Ibrahimi, A., Krylychkina, O., Vreys, R., Van Der Linden, A., Maes, F., Debyser, Z., Himmelreich, U. & Baekelandt, V. 2011. Evaluation of the specificity and sensitivity of ferritin as an MRI reporter gene in the mouse brain using lentiviral and adeno-associated viral vectors. *Gene Ther,* 18**,** 594-605.

Virostko, J., Chen, Z., Fowler, M., Poffenberger, G., Powers, A. C. & Jansen, E. D. 2004. Factors influencing quantification of in vivo bioluminescence imaging: application to assessment of pancreatic islet transplants. *Mol Imaging,* 3**,** 333-42.

Virostko, J. & Jansen, E. D. 2009. Validation of bioluminescent imaging techniques. *Methods Mol Biol,* 574**,** 15-23.

Wahlgren, N., Ahmed, N., Davalos, A., Hacke, W., Millan, M., Muir, K., Roine, R. O., Toni, D. & Lees, K. R. 2008. Thrombolysis with alteplase 3-4.5 h after acute ischaemic stroke (SITS-ISTR): an observational study. *Lancet,* 372**,** 1303-9.

Wang, L., Zhang, Z., Wang, Y., Zhang, R. & Chopp, M. 2004. Treatment of stroke with erythropoietin enhances neurogenesis and angiogenesis and improves neurological function in rats. *Stroke,* 35**,** 1732-7.

Weber, R., Ramos-Cabrer, P., Justicia, C., Wiedermann, D., Strecker, C., Sprenger, C. & Hoehn, M. 2008. Early prediction of functional recovery after experimental stroke: functional magnetic resonance imaging, electrophysiology, and behavioral testing in rats. *J Neurosci,* 28**,** 1022-9.

Weber, R., Ramos-Cabrer, P., Wiedermann, D., Van Camp, N. & Hoehn, M. 2006. A fully noninvasive and robust experimental protocol for longitudinal fMRI studies in the rat. *Neuroimage,* 29**,** 1303-10.

Wilson, T. & Hastings, J. W. 1998. Bioluminescence. *Annu Rev Cell Dev Biol,* 14**,** 197-230.

Xiong, Y., Mahmood, A., Meng, Y., Zhang, Y., Qu, C., Schallert, T. & Chopp, M. 2010. Delayed administration of erythropoietin reducing hippocampal cell loss, enhancing angiogenesis and neurogenesis, and improving functional outcome following traumatic brain injury in rats: comparison of treatment with single and triple dose. *J Neurosurg,* 113**,** 598-608.

Yamashita, T., Ninomiya, M., Hernandez Acosta, P., Garcia-Verdugo, J. M., Sunabori, T., Sakaguchi, M., Adachi, K., Kojima, T., Hirota, Y., Kawase, T., Araki, N., Abe, K., Okano, H. & Sawamoto, K. 2006. Subventricular zone-derived neuroblasts migrate and differentiate into mature neurons in the post-stroke adult striatum. *J Neurosci,* 26**,** 6627-36.

Yang, Q. X., Smith, M. B., Briggs, R. W. & Rycyna, R. E. 1999. Microimaging at 14 tesla using GESEPI for removal of magnetic susceptibility artifacts in T(2)(*)-weighted image contrast. *J Magn Reson,* 141**,** 1-6.

Yu, S. W., Friedman, B., Cheng, Q. & Lyden, P. D. 2007. Stroke-evoked angiogenesis results in a transient population of microvessels. *J Cereb Blood Flow Metab,* 27**,** 755-63.

Zachary, I. 2005. Neuroprotective role of vascular endothelial growth factor: signalling mechanisms, biological function, and therapeutic potential. *Neurosignals,* 14**,** 207-21.

Zhang, R., Zhang, Z., Wang, L., Wang, Y., Gousev, A., Zhang, L., Ho, K. L., Morshead, C. & Chopp, M. 2004. Activated neural stem cells contribute to stroke-induced neurogenesis and neuroblast migration toward the infarct boundary in adult rats. *J Cereb Blood Flow Metab,* 24**,** 441-8.

Zhang, R. L., Zhang, Z. G., Zhang, L. & Chopp, M. 2001. Proliferation and differentiation of progenitor cells in the cortex and the subventricular zone in the adult rat after focal cerebral ischemia. *Neuroscience,* 105**,** 33-41.

Appendix

List of abbreviations

AMP	adenosine-mono-phosphate
Ang1	angiopoietin 1
Ang2	angiopoietin 2
ATP	adenosine-tri-phosphate
BBB	blood brain barrier
BLI	bioluminescence imaging
BOLD	blood oxygenation level dependent
BrdU	5-bromo-2'-deoxyuridine
CBF	cerebral blood flow
CBV	cerebral blood volume
CCD	charged coupled device
CD31	platelet endothelial cell adhesion molecule (PECAM)
CO_2	carbon dioxide
DCX	doublecortin
deoxyHB	deoxygenated hemoglobin
DNA	deoxyribonucleic acid
EGF	epidermal growth factor
FGF	fibroblast growth factor
FID	free induction decay
G-CSF	granulocyte colony-stimulating factor
Gd-DTPA	gadolinium (Gd) with diethylenetriaminepenta acetic acid (DTPA)
Glut-1	glucose transporter 1
HIF1α	hypoxia inducible factor 1α
HRE	hypoxia-response element
ip	intra-peritoneal
iv	intra-venous
MCA	middle cerebral artery
MCAO	middle cerebral artery occlusion
MRI	magnetic resonance imaging
NMDA	*N*-Methyl-D-aspartate
NMR	nuclear magnetic resonance
oxyHb	oxygenated hemoglobin
pCO_2	partial pressure of carbon dioxide
PDGF	platelet-derived growth factor

PET	positron emission tomography
pO_2	partial pressure of oxygen
PPi	pyrophosphate
RECA-1	rat endothelial cell antigen 1
rt-PA	recombinant tissue plasminogen activator
S1	primary somatosensory cortex
S2	secondary somatosensory cortex
sc	sub-cutaneous
SGZ	subgranular zone
SSCE-MRI	steady-state contrast-enhanced magnetic resonance imaging
SVZ	subventricular zone
TE	echo time
TR	repetition time
VEGF	vascular endothelial growth factor
VEGFR2	vascular endothelial growth factor receptor 2
vWF	von Willebrand factor

Personal contribution to the publications

I.: Monitoring Angiogenesis after stroke using a VEGFR2-luc mouse model

I designed the study, performed the experiments, analyzed the data, and wrote the manuscript.

II.: Vascular changes after stroke in the rat – a longitudinal study using optimized magnetic resonance imaging

I designed the study together with P. Böhm-Sturm and T. Farr. We realized all experiments together and I performed a part of the immunhistological analysis of brain section. I was involved in preparation of the manuscript.

III.: Optimizing bioluminescence sensitivity for noninvasive imaging of neural stem cell grafts in the mouse brain

I designed the study together with M. Aswendt. We performed all experiments together, shared the analysis, and wrote the manuscript together.

IV.: High field BOLD response to forepaw stimulation in the mouse

I designed the study under supervision of M. Hoehn and T.Farr. I performed all experiments, analyzed the data, and wrote the manuscript.

List of publications

Original articles

I. **Monitoring Angiogenesis after stroke using a VEGFR2-luc mouse model.**
Joanna M. Adamczak, Gabi Schneider, Melanie Nelles, Ivo Que, Ernst Suidgeest, Louise v.d. Weerd, Clemens Löwik, Mathias Hoehn
Angiogenesis (2012), (under review)

II. **Vascular changes after stroke in the rat – a longitudinal study using optimized magnetic resonance imaging.**
Philipp Boehm-Sturm*, Tracy D. Farr*, Joanna M. Adamczak, Jan Jikeli, Luam Mengler, Dirk Wiedermann, Therése Kallur, Valerij Kiselev, and Mathias Hoehn
Contrast Media and Molecular Imaging (2013) (in press)
(*: authors contributed equally)

III. **Optimizing bioluminescence sensitivity for noninvasive imaging of neural stem cell grafts in the mouse brain.**
Markus Aswendt*, Joanna M. Adamczak*, Sebastian Couillard-Depres, Mathias Hoehn
PLoS ONE (2013) 8(2): e55662
(*: authors contributed equally)

IV. **High field BOLD response to forepaw stimulation in the mouse.**
Joanna M. Adamczak, Tracy D. Farr, Jörg Seehafer, Daniel Kalthoff and Mathias Hoehn
NeuroImage (2010). 51(2): 704-712

Book chapter

V. **In vivo imaging of cell transplants in experimental ischemia.**
Joanna M. Adamczak, Mathias Hoehn
in: Progress in Brain Research (2012). 201:55-78

VI. **Non-invasive multimodal imaging of stem cell transplants in the brain using BLI and MRI**
Annette Tennstaedt, Markus Aswendt, Joanna M. Adamczak, Mathias Hoehn
in: Imaging and tracking stem cells: Methods (in press)

Danksagung

Zunächst möchte ich mich bei Prof. Dr. Mathias Hoehn bedanken, dass er mich damals als Lehramts-Studentin in seine Arbeitsgruppe aufgenommen und mir damit einen Weg in die Welt der Wissenschaft eröffnet hat. Vielen Dank, dass Du an meine Fähigkeiten geglaubt hast und mir die Möglichkeit gegeben hast, in diesem spannenden Themenbereich zu promovieren. Ich habe immer vollste Unterstützung von Dir. Besonders danken möchte ich Dir für die Ermöglichung eines Auslandsaufenthaltes, welcher mir nicht nur erlaubte ein Projekt eigenverantwortlich aufzubauen und durchzuführen, sondern mich auch persönlich weiter gebracht hat.

Bedanken möchte ich mich auch bei Dr. Heike Endepols für die Betreuung meiner Doktorarbeit. Ich konnte immer mit meinen Anliegen zu Dir kommen. Vielen herzlichen Dank, liebe Heike, für deine Unterstützung in allen Bereichen, den wissenschaftlichen, den organisatorischen und auch den persönlichen.

Bei Prof. Dr. Wolfgang Walkowiak möchte ich mich bedanken für seine Bereitschaft mich seitens der Universität zu betreuen. Ich danke Ihnen für ihr Interesse an meinem Thema und für das unkomplizierte Zustandekommen unserer Treffen.

I would also like to thank Prof. Dr. Clemens Löwik for the possibility to work in his group at the LUMC in beautiful Leiden. I have enjoyed working in such a great scientific environment and with such lovely people. Dear Ivo Que, thank you for letting me into your kingdom of bioluminescence. Special thanks to Dr. Louise van der Weerd for making the MR available to me. Thank you, dear Ernst Suidgeest, for your help and for your company. Thanks also to Robert van Leeuwen, the best animal care taker ever. Dear Clemens, thank you as well for introducing me to the special beauty of the Netherlands by an exciting boat trip around the grachten of Leiden.

Ich möchte mich bei allen derzeitigen und früheren Mitgliedern der In-vivo-NMR Gruppe bedanken, die auf vielfältige Art und Weise mein Werken begleitet und unterstützt haben. Special thanks belong to Tracy Farr, who has been more than my mentor since we met. Danke auch an Therese Kallur und Annette Tennstädt für Tips und Tricks und seelische Unterstützung auf dem Weg zu den zwei Buchstaben. An dieser Stelle möchte ich auch meinen Doktoranden-Weggefährten Luam Mengler, Philipp Boehm-Sturm und Markus Aswendt bedanken. Gemeinsam haben wir Höhen und Tiefen durchgestanden und ohne euch wären die Laborabende doppelt so lang und die Konferenzen nur halb so spannend gewesen. Danke an die neue Generation, Marion Selt und Claudia Hafeneger, für eure tatkräftige Unterstützung auf der Zielgeraden!

Zu guter Letzt möchte ich meiner Familie danken. Ich danke Euch für all die Unterstützung, die ich erfahren durfte, für Euer Verständnis und Euren Rückhalt. Ich danke Euch für all das und noch viel mehr! Danke auch an meine Freundinnen, die einfach immer da waren!

Erklärung

Ich versichere, dass ich die von mir vorgelegte Dissertation selbständig angefertigt, die benutzten Quellen und Hilfsmittel vollständig angegeben und die Stellen der Arbeit − einschließlich Tabellen, Karten und Abbildungen −, die anderen Werken im Wortlaut oder dem Sinn nach entnommen sind, in jedem Einzelfall als Entlehnung kenntlich gemacht habe; dass diese Dissertation noch keiner anderen Fakultät oder Universität zur Prüfung vorgelegen hat; dass sie − abgesehen von unten angegebenen Teilpublikationen − noch nicht veröffentlicht worden ist, sowie, dass ich eine solche Veröffentlichung vor Abschluss des Promotionsverfahrens nicht vornehmen werde. Die Bestimmungen der Promotionsordnung sind mir bekannt. Die von mir vorgelegte Dissertation ist von Prof. Dr. Mathias Hoehn, Dr. Heike Endepols und Prof. Dr. Wolfgang Walkowiak betreut worden.

Köln, den 18.02.2013 _____